

DISSERTATION

APPLICATIONS AND ADVANCED SINTERING TECHNIQUES OF FUNCTIONALLY GRADED
ZNO-BASED THERMOELECTRIC MATERIAL

Submitted by

Corson Lester Cramer

Department of Mechanical Engineering

In partial fulfillment of the requirements

For the Degree of Doctor of Philosophy

Colorado State University

Fort Collins, Colorado

Fall 2017

Doctoral Committee:

Advisor: Kaka Ma

Co-Advisor: Susan P. James

John D. Williams

Walajabad Sampath

Jamie R. Neilson

Copyright by Corson Lester Cramer 2017

All Rights Reserved

ABSTRACT

APPLICATIONS AND ADVANCED SINTERING TECHNIQUES OF FUNCTIONALLY GRADED ZNO-BASED THERMOELECTRIC MATERIAL

Thermoelectric generator (TEG) materials provide a unique solid-state energy conversion from heat to electricity. Nanostructured TEGs experiencing transient thermal loads at medium to high-temperatures are susceptible to degradation due to thermal stress cracking, which subsequently causes decreased lifetime. Previous efforts to prevent the thermal degradation have led to the following approaches: geometric pinning, compositional gradients, and segmentation of different materials. In the present research, functionally graded zinc oxide (ZnO) materials with graded grain size distribution were fabricated using a water sintering strategy via spark plasma sintering (SPS) with a thermal gradient in combination with modified tooling and strategic mechanical load schedules. Samples with homogeneous grain size distribution were also fabricated as a baseline for comparison. The primary objective of the work is to investigate the correlation between the processing conditions, formation of graded microstructure, and the resultant thermoelectric (TE) output performance and lifetime of the ZnO materials. The fundamental understanding of this correlation will contribute to future design of TEG materials using the approach of graded microstructure. The hypothesis is as follows: in a TEG material with graded grain size distribution, one side that consists of coarse (micron-sized) grains is exposed to the heat source. This coarse-grained side of the material can mitigate thermal stress cracking by spreading the heat more quickly during transient

heating and thus provide improved thermal stability. The other side of the TEG material consists of fine grains (submicron-sized) and still exhibits high efficiency.

In the current study, both continuously graded ZnO materials and a five-layer discretely graded ZnO material were fabricated. Microstructural characterization shows that the grain size gradient of the continuously graded materials across a 10-mm thickness goes from submicron scale (average size ~ 180 nm) to micron scale (~ 1.2 μm). The thermoelectric properties of the baseline ZnO materials with uniform grain sizes were measured. Using the data obtained from those samples with uniform grain sizes, the peak efficiencies of the continuously graded materials and the five-layer graded materials were simulated and compared to the experimentally measured values. The lifetime of the ZnO samples was evaluated from the electrical resistance at the cycling temperature. The results of the final efficiencies suggest that the thermoelectrical performance of the ZnO materials benefit from the grain size gradation.

In addition, the sintering behavior of the continuously graded ZnO system is investigated and compared to that of the isothermally sintered samples to establish a predictive model of the microstructure (density-grain size-time relation). A discrepancy is observed between the prediction of the continuously graded materials and the experimental results. This discrepancy is attributed to a stress shielding that develops during sintering due to differential sintering from the temperature gradient. The stress shielding occurs when denser, and thus stiffer material develops adjacent to less dense and less stiff material causing the stress to vary because the stress is not evenly distributed. The stress shielding effect during sintering is further investigated through theoretical sintering equations. Using the viscoelastic analogy in sintering, the stress to be added to the sample

during sintering in a thermal gradient is quantified to compensate the discrepancy from the samples sintered isothermally based on an average strain rate difference.

ACKNOWLEDGEMENTS

I would like to first and foremost thank my advisors Dr. Kaka Ma, Dr. Susan P. James, and Dr. Troy B. Holland, for providing me the opportunity to grow and develop as a scientist in the realm of materials-based engineering and research for mechanical engineering applications and design. Special thanks to Dr. Holland for providing the opportunity in his lab at CSU. I am grateful to my collaborators. First, Jesus Gonzalez-Julian from Forschungszentrum Jülich Germany, provided great help and knowledge early on in my graduate program; Jin Zhihe from U. Maine helped model the thermoelectric performance of the materials; Wenjie Li from U. Virginia Tech. provided assistance in the thermoelectric measurements. I would also like to thank the members of the Advanced Materials Processing and Testing (AMPT) Lab, especially Paul Colasuonno and David Anderson, who aided in the manufacturing of our functionally graded materials. The Chemistry facilities operators, Pat McCurdy and Roy Geiss, provided a lot of useful information and help with materials characterization.

I have always had a lot of support from my family and friends along the long arduous road to my doctorate, and I would like to thank them. My mother, Joanie Kuhn, and father, Dr. Scott R. Cramer, deserve special thanks for always supporting me financially and mentally. I would like to thank my siblings Hayden and Natalie, Storrie and Ramunas, and Kett and Jon for their continued support. Special thanks go out to my uncle and aunt, Wolfgang and Janet, for a generous donation for research expenses. I would also like to thank my grandparents, Annette and Lester Cramer and Alex and Jane Kvasnak, for their

continued support. I could not have done this without my family's support; they taught me to never be afraid of challenges and to dream big!

TABLE OF CONTENTS

ABSTRACT	ii
ACKNOWLEDGEMENTS.....	v
CHAPTER 1 - INTRODUCTION	1
1.1 HYPOTHESIS AND SPECIFIC AIMS.....	5
REFERENCES	8
CHAPTER 2 - LITERATURE REVIEW	10
2.1 INTRODUCTION.....	10
2.2 THERMOELECTRIC GENERATORS.....	11
2.3 THERMOELECTRIC MATERIAL.....	14
2.4 THERMAL STRESS, THERMAL SHOCK, AND THERMAL FATIGUE CRACKING IN LIFETIME OF TEGS.....	15
2.5 CURRENT METHODS FOR IMPROVING TEG LIFETIME	19
2.6 CURRENT TECHNIQUES FOR EFFICIENCY IMPROVEMENTS.....	21
<i>A. Segmentation.....</i>	<i>22</i>
<i>B. Homogenous Property Manipulation.....</i>	<i>23</i>
2.7 MODELLING OF TEG FGMS	25
2.8 PROCESSING FGMS WITH SINTERING	28
2.9 SINTERING THEORY.....	30
<i>A. Powder Preparation.....</i>	<i>31</i>
<i>B. Sintering – Processing of Powder Compacts.....</i>	<i>32</i>
<i>C. Liquid Phase Sintering.....</i>	<i>37</i>
<i>D. Pressure Assisted Sintering, Constitutive Equations and Advanced Topics.....</i>	<i>38</i>
2.10 IMPORTANCE OF ZNO.....	41
<i>A. ZnO as a Multifunctional Material</i>	<i>41</i>
<i>B.SPS/FAST Processing and Liquid Phase Enhanced Transport with ZnO.....</i>	<i>42</i>
<i>C. Al-doped ZnO for Enhanced Electrical Conductivity</i>	<i>42</i>
2.11 GRAIN SIZE EFFECTS.....	43
<i>A. Effects on Sintering.....</i>	<i>43</i>
<i>B. Effects on Material Properties.....</i>	<i>44</i>
REFERENCES	47
CHAPTER 3 - CONTINUOUS FUNCTIONALLY GRADED MATERIAL TO IMPROVE THE THERMOELECTRIC PROPERTIES USING ZNO.....	55
3.1 INTRODUCTION.....	55
3.2 PROCEDURE	58
3.3 RESULTS AND DISCUSSION	62
<i>A. Isothermal Sintering for Predictions of Microstructure.....</i>	<i>63</i>
<i>B. COMSOL Modeling.....</i>	<i>65</i>
<i>C. Thermal Gradient Sintering.....</i>	<i>66</i>
<i>D. Microstructure of Samples Sintered Isothermally for Predictions vs. a Sample Sintered in a Thermal Gradient.....</i>	<i>70</i>
<i>E. Micro Hardness Data on Fully Dense FGM ZnO.....</i>	<i>74</i>
<i>F.TEG Properties on Fully Dense FGM ZnO</i>	<i>75</i>
3.4 CONCLUSION	78

REFERENCES	80
CHAPTER 4 - A LAYERED FGM, CONTROLLING EFFICIENCY, AND TESTING THERMAL FATIGUE DEGRADATION IN A ZNO THERMOELECTRIC USING GRAIN SIZE GRADIENTS ..	84
4.1 INTRODUCTION.....	85
4.2 PROCEDURE	88
4.3 RESULTS AND DISCUSSION	92
4.4 CONCLUSION	104
REFERENCES	106
CHAPTER 5 - PREDICTING FGM MICROSTRUCTURE WHEN SINTERING WITH A THERMAL GRADIENT.....	109
5.1 INTRODUCTION.....	110
5.2 PROCEDURE	115
5.3 RESULTS AND DISCUSSION	116
A. ZnO DGT and TG comparison.....	116
B. Zirconia DGT and TG comparison.....	118
C. Analyzing the Stress shielding in a TG Using ZnO.....	120
5.4 CONCLUSIONS	125
REFERENCES	127
CHAPTER 6 - CONCLUSIONS AND FUTURE WORK	129
6.1 SUMMARY OF PROCESSING.....	129
6.2 SUMMARY OF FGM MODELING EFFORT	130
6.3 SUMMARY OF EXPERIMENTAL RESULTS	131
6.4 FUTURE WORK.....	131
A. Extended Work on Grain Size Gradation in ZnO.....	132
B. Using an Al-doped ZnO system	132
C. Continued Investigation of Stress Shielding in Thermal Gradient SPS.....	135
D. Final Review and Recommendation	136
REFERENCES	138
APPENDIX A.....	139
ZNO CATALYSIS COMPLEXION DIFFUSION TRANSPORT	139
REFERENCES	145
APPENDIX B	146
SELECTION OF FEEDSTOCK POWDER TO OBTAIN MINIMUM SINTERING CONDITIONS - DIRECT COMPARISON OF US RESEARCH NANOMATERIALS, INC. ZNO VERSUS INFRAMAT ADVANCED MATERIALS, LLC ZNO.....	146

LIST OF FIGURES

Figure 1.1: Schematic of graded microstructural for thermoelectric materials. (a) Continuous gradation; (b) Layered gradation. The grain size gradation is close to an order of magnitude.	4
Figure 2.1: Schematic of an n-type and p-type coupled thermoelectric module showing both the n-type and p-type legs [8].	12
Figure 2.2: zTs of common n-type thermoelectric materials [2].	15
Figure 2.3: Critical thermal shock and thermal shock residual strength of ceramics [17]. ..	17
Figure 2.4: Schematic of Functionally graded cutting tool, where material composition gradient was first proposed, and a continuous thermal conductivity gradient was suggested [18], [19].	18
Figure 2.5: Schematic of a thermoelectric generator and pin configuration [27].	20
Figure 2.6: Schematic of a high performance multi-segmented thermoelectric generator [1].	22
Figure 2.7: Dimensional Z for individual materials, compositional FGMs, and carrier concentration FGMs [39].	23
Figure 2.8: Dimensional Z for carrier concentration FGMs [39].	25
Figure 2.9: Energy conversion efficiency versus electrical current density for a PbTb–SiGe graded nanocomposite of varying gradations, n [56].	28
Figure 2.10: Schematic of off-set die arrangement. The hot side is created from a current choke from less contacting area [60].	30
Figure 2.11: Schematic of property hierarchy and manipulation.	31
Figure 2.12: Morphological identification of starting powder for sintering [70].	32
Figure 2.13: Evolution of the microstructure during sintering. a) Initial stage b) intermediate stage (open porosity), c) intermediate stage (onset of pore closure), d) final stage [72].	34
Figure 2.14: Equilibrium shapes of the pores in polycrystalline solids showing the balance between the surface and interfacial forces at the point where the grain boundary intersects the pore [71].	35
Figure 2.15: Mass transport mechanisms in solid state sintering [71].	36
Figure 3.1: 3-D representation of the whole sintering setup (left) and fully machined sintering setup used in sintering of specimens in a thermal gradient (right).	61
Figure 3.2: ZnO powder from US Research Nanomaterials, Inc. (US Nano). TEM image (top left). SEM image (top right) and XRD pattern (bottom).	63
Figure 3.3: DGT plot for prediction of grain size and porosity in a sample sintered with a TG when load is ramped to 73 MPa after large water outgassing.	64
Figure 3.4: DGT plot for prediction of grain size and porosity in a sample sintered with a TG when the load is decreased to 35 MPa before the large water outgassing.	65
Figure 3.5: COMSOL Model of TG sintering setup for temperature field for ZnO.	66
Figure 3.6: Temperature data collected from a sample sintered in a TG when load is ramped to 73 MPa after the large water outgassing.	67
Figure 3.7: Macroscopic cross section and microscopic images of ZnO that is fully dense with a graded grain size distribution.	69

Figure 3.8: Grain size gradation of fully dense sample sintered in a TG.....	70
Figure 3.9: Microstructural comparisons for a sample sintered in a TG versus a sample sintered isothermally when load is ramped to 73 MPa after the large water outgassing.	72
Figure 3.10: Macro- and microstructural image of the sample sintered in a TG done when the load is decreased to 35 MPa before the large water outgassing.	73
Figure 3.11: Vickers Micro Hardness axial traverse down the fully dense FGM ZnO.....	75
Figure 3.12: Thermoelectric properties of the fully dense material sintered in a TG versus samples sintered isothermally having the size grains as the hot and cold side of the sample sintered in a TG. (a) Seebeck and (b) resistivity, and (c) thermal conductivity are measured, and the zT (d) is calculated.....	78
Figure 4.1: Sample setup for TEG testing on a ZEM-3 from ULVAC.....	89
Figure 4.2: COMSOL simulation of thermoelectric tester rig for large temperature difference across the sample.....	90
Figure 4.3: Thermoelectric tester setup.....	91
Figure 4.4: Macroscopic image of the five-layer FGM sample.....	92
Figure 4.5: SEM images of individual layers where the top left is layer # 1, top right is layer # 2, middle left is layer # 3, middle right is layer # 4, and the bottom is layer # 5.	94
Figure 4.6: SEM images of a diffusion bonded joint in the five-layer ZnO FGM.....	96
Figure 4.7: Thermoelectric property data for individual layers.	97
Figure 4.8: Simulated data of efficiency versus current for the model for small, large, and intermediate grains sizes as well as continuous and five-layer FGM.....	99
Figure 4.9: Experimental results for efficiency versus current for small, large, and intermediate grains sizes as well as continuous and five-layer FGMs before thermal shock tests.....	100
Figure 4.10: Temperature schedule of the hot side of the thermoelectric for thermal shock tests showing five cycles.....	101
Figure 4.11: Lifetime test for small, large, and intermediate grains sizes as well as continuous and five-layer FGM. Resistance is the resistance at 600°C.....	102
Figure 4.12: Experimental results for efficiency versus current for small, large, and intermediate grains sizes as well as continuous and five-layer FGMs 20 cycles of thermal shock tests.....	103
Figure 5.1: Schematic of the sintering effects in a sample sintered in a TG.	114
Figure 5.2: DGT plot for grain size and porosity predictions of a sample sintered in a TG when load is ramped to 73 MPa after large water outgassing.....	117
Figure 5.3: DGT plot for microstructural prediction of continuous zirconia sample done with constant load of 32 MPa.	119
Figure 5.4: Grain size gradation of fully dense thermal gradient sample.....	120
Figure 5.5: ZnO DGT (sans grain size) of for spatial predictions from a DGT with mechanical load of 35 MPa (11 kN) showing the cut off time of 385 seconds.	122
Figure 5.6: ZnO Strain rates for TG spatial predictions from a DGT where the applied load is 35 MPa (11 kN).	123
Figure 5.7: ZnO Strain rate differences versus time for the different heating schedules...	124
Figure 6.1: Schematic of layered powder for sintering of compositional FGM TEG.....	135

LIST OF SYMBOLS

$\bar{\alpha}_{pn}$	Average Seebeck coefficient of a couple
α_S	Seebeck coefficient of a material
α_{COT}	Coefficient of thermal expansion
J	Current density through a TEG material
I	Current through a TEG material
$\sigma_{thermal}$	Thermal stress
σ_S	Strength of a material
σ_{DF}	Driving force for sintering
σ_C	Electrical conductivity of a material
σ_y	Yield stress of a material
σ_0	Starting stress for dislocation motion
$T, \Delta T, \nabla T$	Temperature, Temperature difference, Temperature gradient
E	Modulus of elasticity
T_H	Hot side temperature of TEG module or material
T_C	Cold side temperature of TEG module or material
TSR	Thermal shock resistance
q_H	Heat into a TEG in thermoelectric mode
q_C	Heat rejected from TEG in thermoelectric mode
K	Thermal conductance of TEG module
k	Thermal conductivity of a material
R_g	Internal resistance of a TEG couple
Z	Figure of merit for a TEG couple
z	Figure of merit for a material
ρ_R	Electrical resistivity of a material
ρ_{MD}	Mass density
A	Cross-sectional area of a TEG material
r	Radius of curvature of a pore
G	Grain size
γ_{sv}	Free energy of the solid-vapor interface
γ_{gb}	Free energy of the grain boundary interface
L_L	Lorentz Factor
L	TEG leg length
e	Elementary charge
μ	Mobility of majority carrier
k_B	Boltzmann constant
k_y	Strengthening coefficient
n	Majority carrier density
h	Planck's constant
k_e	Thermal conductivity from electron transport
k_l	Thermal conductivity from lattice transport

ε	Strain
$\dot{\varepsilon}$	Strain rate
φ	Shape factor based on particle size
m	Exponent that varies with the mode of diffusion
Ω	Atomic volume
D	Diffusion coefficient
M_b	Boundary mobility of triple junction
t	Time
ϕ	Stress intensification factor
p_a	Applied pressure
η	Shear viscosity
τ	Stress exponent
ν	Poisson ratio
ZT	Figure of merit for a thermoelectric coupled module
zT	Figure of merit for a thermoelectric material or leg
ψ	dihedral angle

CHAPTER 1 - INTRODUCTION

Energy in the form of waste heat is expelled from many operating systems that use heat as their thermodynamic driving source, such as cars, boats, and power plants. Thermoelectric generators (TEGs) are solid-state devices that can turn the waste heat into electrical power. Most waste heat recovery systems are TEG modules that are placed at the waste heat source and are often further cooled actively or passively. The efficiency of the current TEG modules with homogenous grain structure is about 9-12% and their service temperatures are limited to a small range of roughly 200°C. Systems with fast thermal cycling and transient operation are examples of situations where the thermal stresses degrade TEGs because of poor heat dissipation when the TEG is initially subjected to a heat source [1]. This makes the thermal stress initially very high and subsequently reach a transient condition until the heat flow becomes steady-state. One critical challenge of the development of TEGs is the degradation of lifetime due to thermal stresses that arise from thermal expansion, thermal shock, and thermal fatigue [2]–[6]. These modes of thermal degradation lead to a reduction of lifetime for thermoelectric devices [7], [8].

Previous optimization of waste heat recovery systems has been limited to a temperature range rather than for the whole lifetime. Improvement has been achieved in a non-dimensional figure of merit for a thermoelectric material, zT , where $zT = \alpha_S^2 T / \rho_R k$; α_S is a material property called the Seebeck coefficient which is a measure of the amount of voltage per degree temperature difference; T is the temperature; ρ_R is the electrical resistivity, and k is the thermal conductivity. TEGs with improved lifetimes are in demand for applications with large temperature differences and for transient heat sources. Functionally graded materials (FGM) could potentially increase TEG lifetime by reducing

the thermal stresses caused by large temperature differences [9]. A few progresses have been achieved on mitigation of thermal cracking and lifetime improvement in thermoelectric materials [8], [10], [11]. One approach to increase the useful temperature range of a TEG is segmentation [12], where several different TEG materials with optimal properties for different temperature ranges are physically joined together in descending order from high temperature material to low temperature material. As an example, a TEG with segmentation consists of SiGe, PbTe, and Bi₂Te₃ with the following spatial arrangement: SiGe is on the hot side and connected to PbTe (middle section), which is connected to Bi₂Te₃ on the cold side.

Zinc oxide (ZnO) is selected as a model material system in the current work because of its consistent thermoelectric properties, ease of manufacturing, potential to be a good candidate for a thermoelectric (TE) material at mid- to high-temperature ranges when doped with Al, and low cost [13]. ZnO has a zT that is not as high as that of the current TE materials used in mid-range temperatures [14]. However, ZnO is a well-known n-type semiconductor with a wide band gap (3.37 eV) and an excitation of binding energy of 60 mV [15]. It is a great candidate for microelectronic and optoelectronic devices.

Investigation into the functionally graded ZnO materials will provide a fundamental guidance to expand the application of graded grain size microstructure in other complex TEG materials such as Al-doped ZnO, degenerately doped semiconductors, and semimetals. The importance of selecting ZnO as the model system in my work will be further discussed in Chapter 2.

The current work aimed to design an advanced manufacturing technique to manipulate grain size distribution for property variation to improve the lifetime of TE

materials by mitigating thermal degradation while retaining high efficiency. To mitigate the thermal stress and to improve the lifetime, we proposed to create a material with graded thermal conductivity to achieve reduced thermal stress on the side of the TE material that is exposed to the heat source. In transient condition, a fast heating rate and initial exposure to high temperatures create high transient thermal stress if the heat is not dissipated well. Once the TE material reaches steady-state, the grain size gradation does not work as much as a protective layer from thermal stresses but still affects the TEG output. A simultaneous effect on the output current range allows for grain size to be an additional design parameter for TEGs. To obtain a thermal conductivity gradient in a material with homogenous chemical composition, our approach is to make a grain size gradation. Materials with large-grained structure conduct heat more effectively than those with fine-grained structure. Thus, large temperature differences do not occur near the side of the TE material that is exposed to the heat source. On the other hand, TE materials with small grains have higher energy conversion efficiency. Therefore, it is imperative to have them on the cold side of the TE material. Ultimately, the goal is to extend the lifetime of TEG materials and to save costs. Figure 1.1 shows schematic diagrams of the continuously graded TE materials and layered TE materials in which one end has micron-sized grains and the other has submicron-sized grains. The continuously graded material is fabricated strategically with a temperature field across the sample during processing. For the layered material, each layer has uniform grain sizes and the magnitude of the grain size is in the same range as that of the continuously graded material. The multiple layers are bonded together by diffusion.

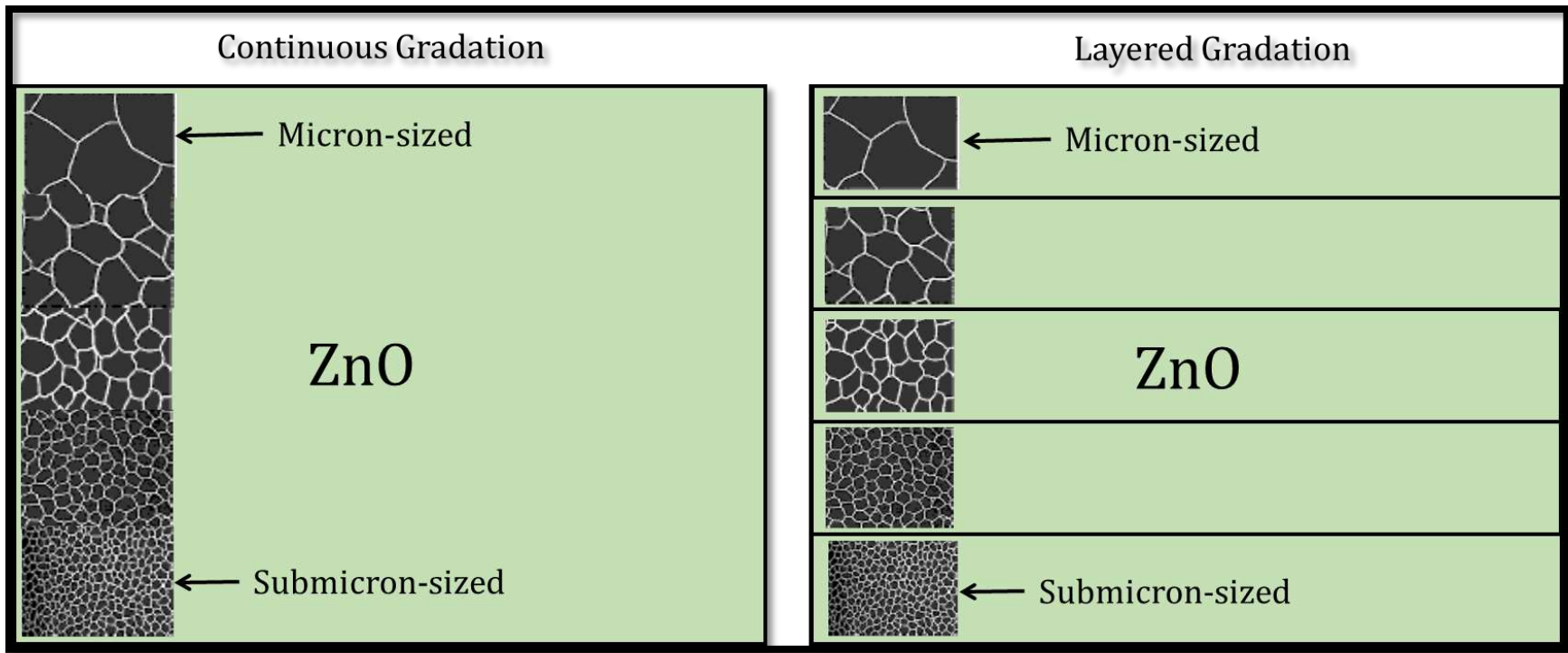


Figure 1.1: Schematic of graded microstructural for thermoelectric materials. (a) Continuous gradation; (b) Layered gradation. The grain size gradation is close to an order of magnitude.

1.1 HYPOTHESIS AND SPECIFIC AIMS

Fundamental Hypothesis: A graded microstructure may positively affect the lifetime and efficiency of a TEG material.

Specific Aim (1): Fabrication and characterization of a material that has a continuous grain size gradation from micron- to submicron-sized grains combined with theoretical prediction of microstructure. This research is discussed in our first paper [16] and is presented in Chapter 3.

Approach for specific aim (1):

- a) Predict microstructure with Density-Grain Size-Time (DGT) plots for a ZnO system using uniform temperature SPS runs.
- b) Control the process to sinter ZnO with a thermal gradient.
- c) Investigate the correlation between the continuously graded microstructure and the TE properties in ZnO with a comparison to the baseline samples with uniform grain size.

Specific Aim (2): Explore an alternative method for grain size gradation in TE materials using a layered structure. Compare the thermoelectric output (efficiency versus current density or current) of layered TE material to those of the TE material with uniform grain sizes in the same range as the individual layers in the FGM. Also, we explore the effects of fast cycling on the lifetime of the samples to test the transient thermal stress reducing potential for improvements in FGM TE material. This research is presented in Chapter 4.

Approach for specific aim (2):

- a) Sinter five layers at different temperatures to obtain discrete layers of uniform grains size within the same grain size range and distribution of the continuous FGM samples.
- b) Bond these layers in the SPS through diffusion.
- c) Model the efficiency versus current for uniform layers to gain insight into the power profile through a range of currents that cannot be reached in practice.
- d) Model the efficiency of the FGM of five layers with TE properties from the 5 individual layers.
- e) Use the property trends from the five individual layers to predict a continuously graded FGM by using 100 layers instead of five.
- f) Experimentally validate the simulations with curves of efficiency versus current.
- g) Thermally cycle the samples with a fast ramp rate to 600°C.
- h) Retest the efficiencies after the cycling is done.

Specific Aim (3): Investigate the effects of thermal gradient sintering where axial differential sintering occurs in one sample, essentially leading to transient sintering where the hot side experiences more shrinkage while the cold side experiences less shrinkage.

This research is presented in Chapter 5.

Approach for specific aim (3):

- a) Analyze the strain at three different spots axially in the system.
- b) Add pressure to the sintering runs with a thermal gradient (TG) and compare the results to the DGT.

b) Use the viscoelastic analogy for an isotropic, linearly viscous, and incompressible material to identify the amount of backpressure that is needed to achieve an improved match with the DGT.

REFERENCES

- [1] S. Quoilin, R. Aumann, A. Grill, A. Schuster, V. Lemort, and H. Spliethoff, "Dynamic modeling and optimal control strategy of waste heat recovery Organic Rankine Cycles," *Applied Energy*, vol. 88, no. 6, pp. 2183–2190, Jun. 2011.
- [2] V. Ravi *et al.*, "Thermal Expansion Studies of Selected High-Temperature Thermoelectric Materials," *Journal of Elec Materi*, vol. 38, no. 7, pp. 1433–1442, Jul. 2009.
- [3] B. L. Wang, Y. B. Guo, and C. W. Zhang, "Cracking and thermal shock resistance of a Bi₂Te₃ based thermoelectric material," *Engineering Fracture Mechanics*, vol. 152, pp. 1–9, Feb. 2016.
- [4] B.-L. Wang and Y.-W. Mai, "On Thermal Shock Behavior of Functionally Graded Materials," *Journal of Thermal Stresses*, vol. 30, no. 6, pp. 523–558, Apr. 2007.
- [5] Y. Isoda, Y. Shinohara, Y. Imai, I. A. Nishida, and O. Ohashi, "Thermal Shock Resistance and Thermoelectric Properties of Boron Doped Iron Disilicides," *Journal of the Japan Institute of Metals*, vol. 63, no. 3, pp. 391–396, 1999.
- [6] H. Takahashi, T. Ishikawa, D. Okugawa, and T. Hashida, "Laser and Plasma-Arc Thermal Shock/Fatigue Fracture Evaluation Procedure for Functionally Gradient Materials," in *Thermal Shock and Thermal Fatigue Behavior of Advanced Ceramics*, D. G. A. Schneider and P. D. D. h c mult G. Petzow, Eds. Springer Netherlands, 1993, pp. 543–554.
- [7] Y. Hori, D. Kusano, T. Ito, and K. Izumi, "Analysis on thermo-mechanical stress of thermoelectric module," in *Eighteenth International Conference on Thermoelectrics, 1999*, 1999, pp. 328–331.
- [8] L. Bakhtiarfard and Y. S. Chen, "Design and Analysis of a Thermoelectric Module to Improve the Operational Life," *Advances in Mechanical Engineering*, vol. 7, no. 1, p. 152419, Jan. 2015.
- [9] M. Koizumi, "FGM activities in Japan," *Composites Part B: Engineering*, vol. 28, no. 1–2, pp. 1–4, 1997.
- [10] E. Hatzikraniotis, K. T. Zorbas, I. Samaras, T. Kyratsi, and K. M. Paraskevopoulos, "Efficiency Study of a Commercial Thermoelectric Power Generator (TEG) Under Thermal Cycling," *Journal of Elec Materi*, vol. 39, no. 9, pp. 2112–2116, Sep. 2010.
- [11] A. S. Al-Merbati, B. S. Yilbas, and A. Z. Sahin, "Thermodynamics and thermal stress analysis of thermoelectric power generator: Influence of pin geometry on device performance," *Applied Thermal Engineering*, vol. 50, no. 1, pp. 683–692, Jan. 2013.
- [12] Y. S. Kang *et al.*, "Evaluation of monolithic and segmented thermoelectric materials by using a large-temperature-span apparatus," in *XVI International Conference on Thermoelectrics, 1997. Proceedings ICT '97*, 1997, pp. 390–393.
- [13] K. P. Ong, D. J. Singh, and P. Wu, "Analysis of the thermoelectric properties of ZnO type ZnO," *Phys. Rev. B*, vol. 83, no. 11, p. 115110, Mar. 2011.
- [14] M. Søndergaard, E. D. Bøjesen, K. A. Borup, S. Christensen, M. Christensen, and B. B. Iversen, "Sintering and annealing effects on ZnO microstructure and thermoelectric properties," *Acta Materialia*, vol. 61, no. 9, pp. 3314–3323, May 2013.
- [15] K. Ellmer and A. Klein, "ZnO and Its Applications," in *Transparent Conductive Zinc Oxide*, Springer, Berlin, Heidelberg, 2008, pp. 1–33.

- [16] C. L. Cramer, J. Gonzalez-Julian, P. S. Colasuonno, and T. B. Holland, "Continuous functionally graded material to improve the thermoelectric properties of ZnO," *Journal of the European Ceramic Society*, vol. 37, no. 15, pp. 4693–4700, Dec. 2017.

CHAPTER 2 - LITERATURE REVIEW

2.1 INTRODUCTION

Energy conversion in thermoelectric generators (TEGs) is a research area of interest. Significant efforts have been put into exploring promising materials and techniques to improve the efficiency and useful temperature range of TEGs [1]. The efficiency of the current TEGs from waste heat reaches a range of 9-13 % with a value of zT approximately one for both n-type and p-type legs. These are used in many applications where waste heat is rejected [2], [3]. They are used within heat exchangers, coupled with solar cells, and on exhaust units in a passive mode. They are known to improve the total efficiency of systems because waste heat is put back into the system in the form of electrical power. New module designs and materials are pushing these limits even further. The most innovative improvement in TEGs is to improve the temperature range and efficiency within a given current output, which has been achieved via segmentation, geometric pinning, and property gradients [4], [5]. One challenge in the development of the TE materials is the formation of cracking due to thermal stresses that arise from transient heat sources; initially the thermal stresses are very high when the TEG is exposed to a heat source and eventually are relieved as the heat flow across the TEG reaches a steady-state condition [6].

This chapter aims to provide the relevant background on the properties, uses, and temperature ranges of TEGs. The chapter also reviews thermal stress issues in TE materials. Subsequently, it discusses the current status of the methods to improve the efficiency and lifetime of thermoelectrics using FGMs. Modelling of efficiency versus current density for a wide range of properties is also discussed. The processing of FGMs

with sintering is discussed. Finally, the sintering theory and specifics of the candidate material, ZnO, are discussed.

2.2 THERMOELECTRIC GENERATORS

Thermoelectric generators encompass the Seebeck, Peltier, and Thomson effects [7]. The Peltier effect is a temperature difference caused at the junction of dissimilar materials when current is passed through the junction. The Thomson effect is the rate of generation of reversible heat in a material with an imposed current flow and a temperature gradient. The Seebeck effect is a voltage caused by a temperature difference imposed between the points where two dissimilar materials are joined at their free ends. Thermoelectric power generation can be explained by performing an energy balance at the hot and cold side junctions of a TEG device like the one shown in Figure 2.1. The net heat that goes into the hot side, q_H , and the net heat rejected from the cold junction, q_C , are shown in Equations (2.1) and (2.2), where $\bar{\alpha}_{pn}$ is the average Seebeck coefficient of the couple, I is the current, T_H is the hot side temperature, K is the total thermal conductance of the couple, and R_g is the total internal resistance of the couple [7].

$$q_H = \bar{\alpha}_{pn} T_H I + K \Delta T - \frac{1}{2} I^2 R_g \quad (2.1)$$

$$q_C = \bar{\alpha}_{pn} T_C I + K \Delta T + \frac{1}{2} I^2 R_g \quad (2.2)$$

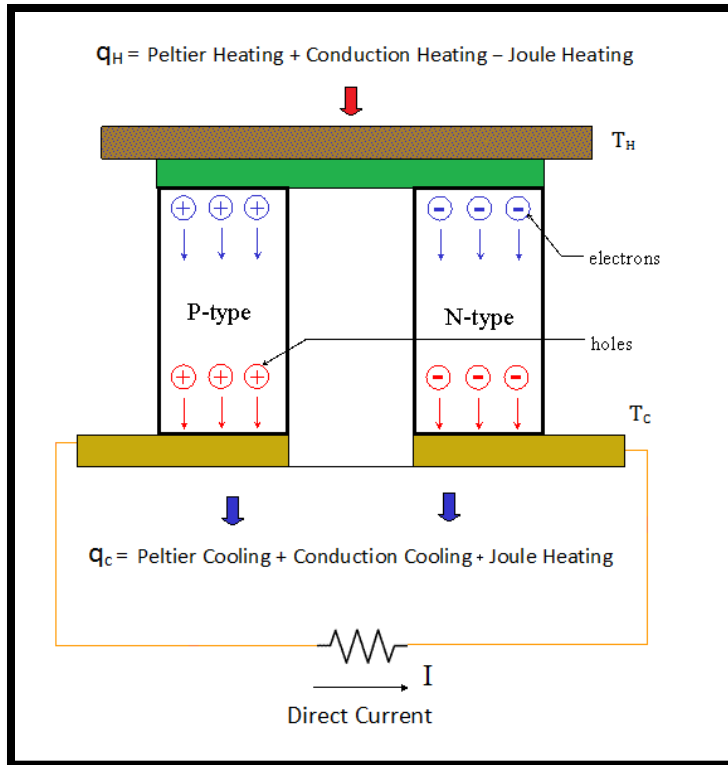


Figure 2.1: Schematic of an n-type and p-type coupled thermoelectric module showing both the n-type and p-type legs [8].

The heat supplied to the hot side is broken down into three components, the Peltier cooling, conduction cooling, and joule heating. The charge carriers are promoted to a level where they can conduct electricity and heat. The energy required to enable the promotion consumes heat and is referred to as the Peltier cooling term. One can think of the Peltier cooling at the hot junction as the act of blooming electrons in the n-type and holes in the p-type that diffuse to the cold junction. The n- and p-type materials conduct heat via both phonon lattice vibrations and electronically by the motion of electrons and holes. The TEG components also heat themselves due to the current flow, I , which is referred to as Joule heating. As mentioned above, the blooming of holes and electrons creates a buildup of carriers on the hot ends of the n- and p-type materials, which creates a concentration gradient. The carriers then diffuse toward the cold side and lead a current to flow.

Simultaneously, some heat is conducted to the cold side. The total Joule heat is I^2R_g ; Half of this term is traditionally assigned to the hot junction. It reduces the amount of heat that needs to be supplied to the hot junction to maintain the hot junction temperature. When an external load completes the circuit, the carriers that were created at the hot side flow to the cold side and are subsequently recombined, which sustains a current when a temperature difference is imposed across the TE device. The heat removed from the cold side is also broken down into three components, the Peltier heating, conduction heating, and joule heating. At the cold side, one-half of the Joule heat is required to be removed. Consequently, it increases the amount of heat that must be removed at the cold junction to maintain the temperature.

The equations (2.3) - (2.5) show how the efficiency is related to the heat and power through the TEG [7]. The heat and the power can be broken down into terms that have the thermoelectric properties. The efficiency can be also expressed solely in terms of temperature and the thermoelectric properties after rearranging the equations. The consolidation of the thermoelectric properties is put into Z , the figure of merit for a module, which is considered the coupled module efficiency.

$$\eta_t = \frac{w}{q_H} = \frac{q_H - q_C}{q_H} = \frac{\bar{\alpha}_{pn}\Delta T I - I^2 R_g}{\bar{\alpha}_{pn} T_H I + K \Delta T - \frac{1}{2} I^2 R_g} = \frac{I^2 R_g}{\bar{\alpha}_{pn} T_H I + K \Delta T - \frac{1}{2} I^2 R_g} \quad (2.3)$$

$$\eta_t = \frac{[\sqrt{1+ZT}-1][(\Delta T/T_H)]}{\sqrt{1+ZT}+1} \quad (2.4)$$

$$\text{where } Z = \frac{\bar{\alpha}_{pn}^2}{K R_g} \quad (2.5)$$

2.3 THERMOELECTRIC MATERIAL

The performance of TE materials, not a coupled module, is evaluated based on a parameter called the non-dimensional figure of merit, zT . The formulation of the zT is derived the same way as the module except the energy balance is done for one of the legs, either n-type or p-type. The zT is defined in (2.6), where α_S is the Seebeck coefficient in V/K, T is the temperature in K, ρ is the electrical resistivity in $\Omega\cdot\text{m}$, and κ is the total thermal conductivity in W/mK due to steady-state phonon and electronic heat transport [1]. These parameters will be discussed throughout this dissertation as we move into characterization of an n-type thermoelectric material, ZnO.

$$zT = \frac{\alpha_S^2 T}{\rho_R \kappa} \quad (2.6)$$

Figure 2.2 displays the typical values of the figures of merit for several n-type thermoelectric materials as a function of operating temperature. Nano-structured PbTe exhibits the highest zT , 80% higher than the bulk PbTe, which has been used since 1960 [1]. Figure 2.2 shows that Bi_2Te_3 is the best candidate for applications below 250°C , and the optimal service temperature range for PbTe is $400\text{-}600^\circ\text{C}$. In contrast, the semi-metals, such as CoSb_3 , La_3Te_4 , and SiGe , are the best candidates to be used in high temperature applications. Researchers have put forth efforts to improve these temperatures range by segmenting these materials or tailoring the properties of a single material [9]–[11].

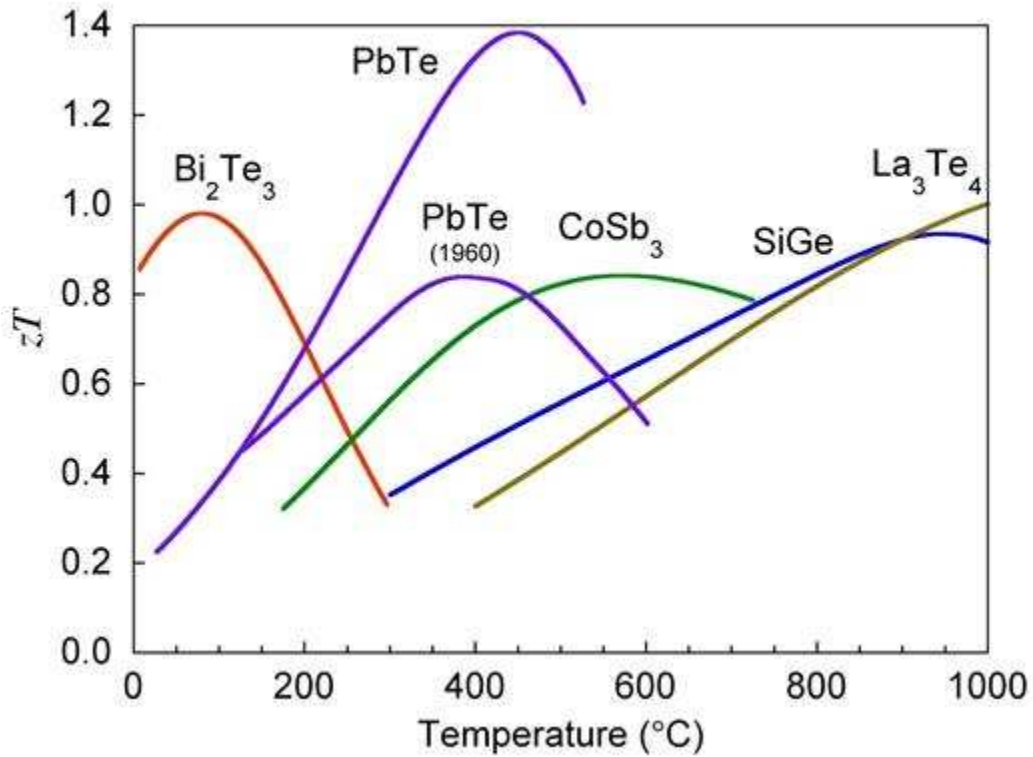


Figure 2.2: zTs of common n-type thermoelectric materials [2].

2.4 THERMAL STRESS, THERMAL SHOCK, AND THERMAL FATIGUE CRACKING IN LIFETIME OF TEGS

Few studies on thermal stress effects on thermoelectric material and TEG lifetime are present in the literature [6], [12]–[16]. The primary goal of the current work is to explore new methods that can mitigate thermal stresses from transient heat flux and high initial temperature exposure in TE materials to enhance the lifetime. Cracking induced by thermal stress degrades the electrical properties and thus the lifetime of the TEGs. Thermal stress cracking leads to the failure of the material by the stress that builds up due to thermal expansion when there are large differences in temperature during transient

heating. The thermal stress is expressed in (2.7); where E is the modulus of elasticity, α_{COT} is the coefficient of thermal expansion, and T is the temperature.

$$\sigma_{thermal} = E\alpha_{COT}\Delta T \quad (2.7)$$

Thermal shock resistance is characterized by the change in strength or other physical properties of the material caused by large temperature differences. When materials are subject to relatively sudden and large temperature differences, the strength of the material will act as a step function leading to higher propensity to crack. In thermal fatigue cracking, the cracks may form upon any thermal treatment. Repeated stress ultimately causes more crack formation.

When a ceramic specimen is subjected to sufficiently severe thermal shocks, micro-cracks will initiate from pre-existing defects and grow to large cracks. Crack propagation in thermally shocked ceramics may be arrested depending on the severity of thermal shock, thermal stress field characteristics and material properties. Thermal shock resistance (TSR) is characterized by (2.8), where σ_S is the strength of the material, and k is the thermal conductivity.

$$TSR = \frac{k\sigma_S}{E\alpha_{COT}} \quad (2.8)$$

If one measures the strength of a thermally shocked ceramic specimen, the material generally exhibits the behavior as shown in Figure 2.3; the strength remains unchanged when the thermal shock ΔT (difference between the initial temperature of the material and applied temperature at the surface) is less than a critical value, ΔT_c , called the critical thermal shock. At $\Delta T = \Delta T_c$, the strength σ_R suffers a precipitous drop and then decreases

gradually with increasing severity of thermal shock. Both material properties and specimen size influence the residual strength of the ceramics exposed to a thermal shock.

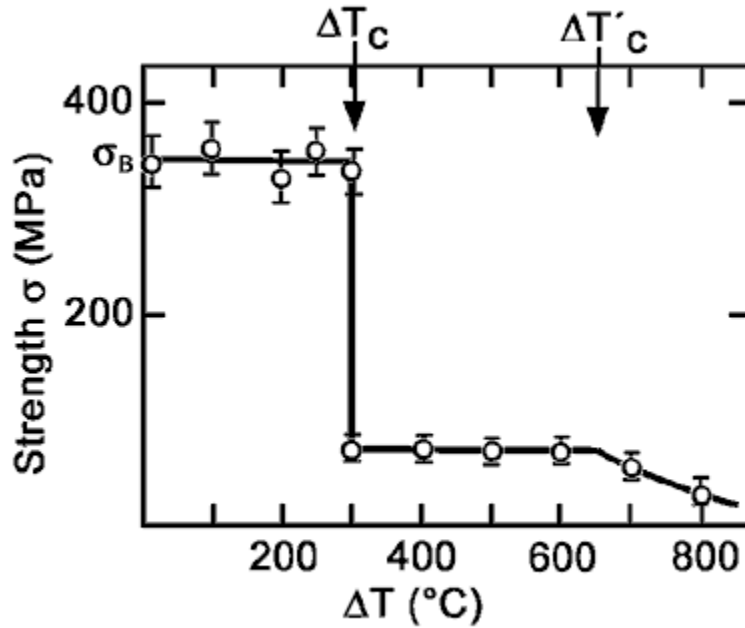


Figure 2.3: Critical thermal shock and thermal shock residual strength of ceramics [17].

A functionally graded microstructural cutting tool was proposed in [18], [19]. It is hypothesized that the thermal conductivity gradient and mechanical property gradient would effectively mitigate heat and reduce the wear of the material. A schematic diagram of a graded microstructure is shown in Figure 2.4, which was the first published study that proposed grain size gradation [17]. The graded microstructure in FGM lead to a gradual change of the material properties with respect to position.

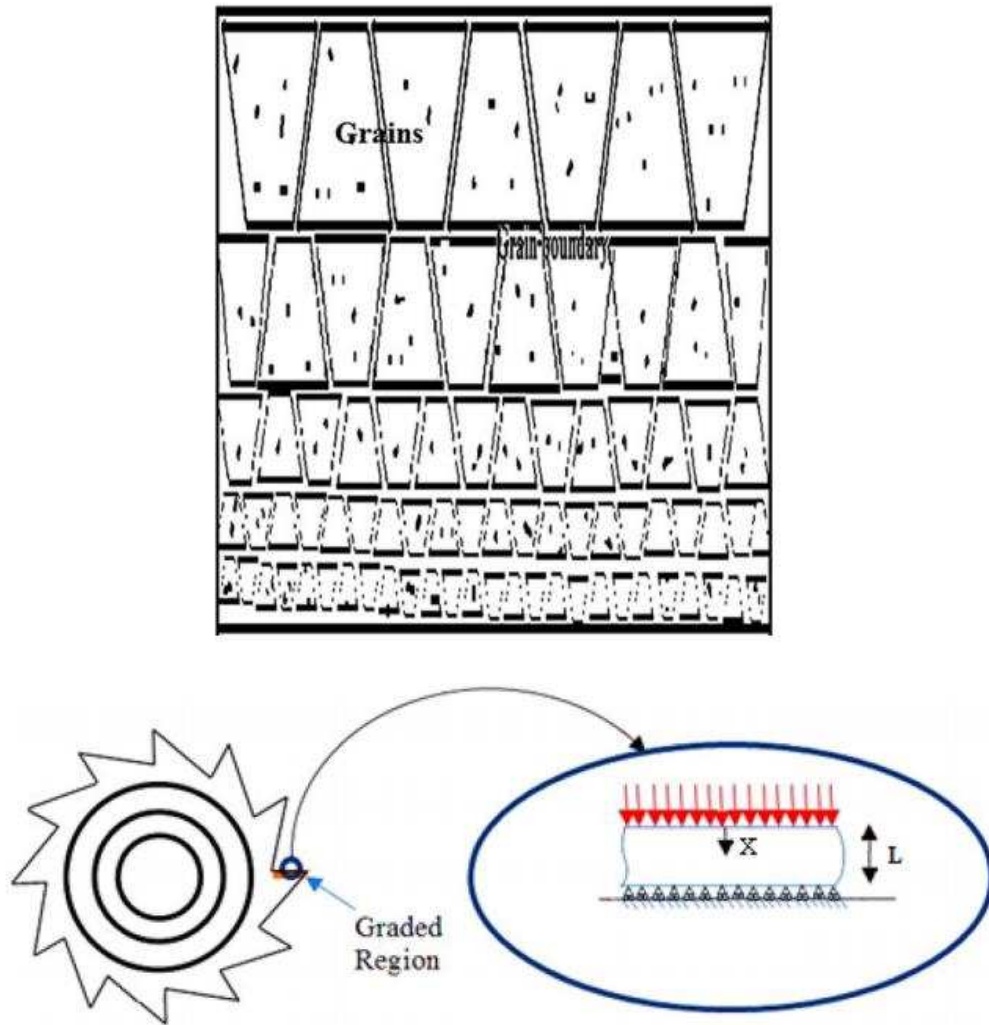


Figure 2.4: Schematic of Functionally graded cutting tool, where material composition gradient was first proposed, and a continuous thermal conductivity gradient was suggested [18], [19].

Most thermal shock resistant material research started with cutting tools. Zhao et al. [20] synthesized symmetrically graded $\text{Al}_2\text{O}_3/\text{TiC}$ and $\text{Al}_2\text{O}_3/(\text{W}, \text{Ti})\text{C}$ FGMs using the hot pressing method and measured the thermal shock residual strengths of the materials. Zheng et al. [21] developed sialon/ Si_3N_4 FGC and measured the thermal shock and thermal fatigue resistance of the material. An example of a composite and FGM with a thermal conductivity and hardness gradient was seen in Xue et al. [22]. Although progress has been

made in FGM cutting tool materials, nanostructured FGMs for thermal shock applications needs to be further investigated.

2.5 CURRENT METHODS FOR IMPROVING TEG LIFETIME

Thermal stress induced cracks and other forms of defects from repeated heat cycling subject TEGs to thermal shock and rapid thermal fatigue leading to poor lifetime of thermoelectric devices [16], [23]. Studies on thermal stress mitigation and extended lifetime in thermoelectric material was previously investigated [24]. A method to study the thermal shock phenomena in FGMs was first tested by Wang and Mai [14]. One group tested the efficiency and TE properties as a function of the thermal cycles to obtain lifetime degradation results [25]. Another study monitored the thermal cracking and lifetime of the Bi-Te system [13]. Failure from thermal expansion and thermal shock were tested in some high temperature thermoelectrics [12], [15]. Geometric pinning is an approach to spread heat more effectively in TEGs and cutting tools. Using a tapered TEG leg geometry, the area decreases continuously along the TEG. Compared to a TEG of the same material with constant area and the same heat flux, the TEG with geometric pinning has smaller temperature differences which lessen thermal stresses as shown in (2.9).

$$q = -kA(T_2 - T_1) \quad (2.9)$$

Pinning of the geometry was also explored to mitigate the thermal stress in thermoelectrics, as shown in Figure 2.5 [26]. Al-Merbati et al. [26] and Erturun et al. [27] also applied the approach of geometric pinning to alleviate high stresses in TEGs. Other groups have successfully mitigated thermal stress by layering, segmentation, and

composite fabrication [13], [28], [29]. Hatzikraniotis et al. characterized the efficiency and lifetime of a thermoelectric in terms of the crack degradation [25].

In addition, multilayered composites exhibited improved resistance to thermal stress cracking, compared to individual layers of material [28]. Microstructure greatly affects the thermal shock behavior primarily due to the thermal conductivity differences [30].

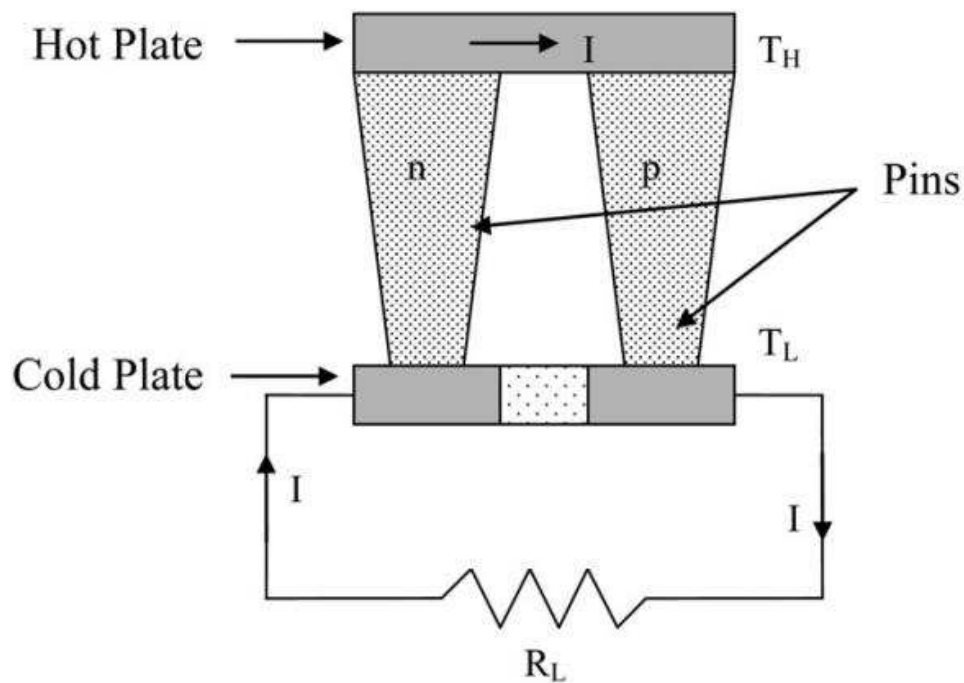


Figure 2.5: Schematic of a thermoelectric generator and pin configuration [27].

Our current work is aimed to develop FGMs that can mitigate heat effectively and thus experience less thermal stress and less cracking than the TE materials with uniform microstructure. The following structural design is proposed: one side of the FGM consists of coarse grains and will be exposed to the heat source; the high thermal conductivity of the coarse-grained structure protect the whole FGM against thermal expansion, shock and

fatigue. The coarse-grain structured end of the FGM will exhibit a higher ductility than a fine-grain structured end.

2.6 CURRENT TECHNIQUES FOR EFFICIENCY IMPROVEMENTS

In applications that require high power and high efficiency, large temperature differences are needed across the TEG. A critical limitation of using a material with homogenous microstructure in a large temperature difference is that a significant portion of the material, no matter if it is the hot side or cold side, do not operate in the maximum temperature range. As seen in Figure 2.6, the efficiency is improved by adding a material suitable for low service temperature in the lower temperature zone of the TEG. It allows the whole length of the TEG to operate with higher efficiency compared to the one using solely one material. Segmentation is one way to combine materials with different optimal temperature ranges [31]. This successfully allows for the temperature range that was not running efficiently to contribute to the overall power generation of the material. This also provides a material that could, in theory, operate in a wider temperature range because there is always a part for the material that is working optimally for different temperatures, thus, providing more motivation for grain size FGM TEGs.

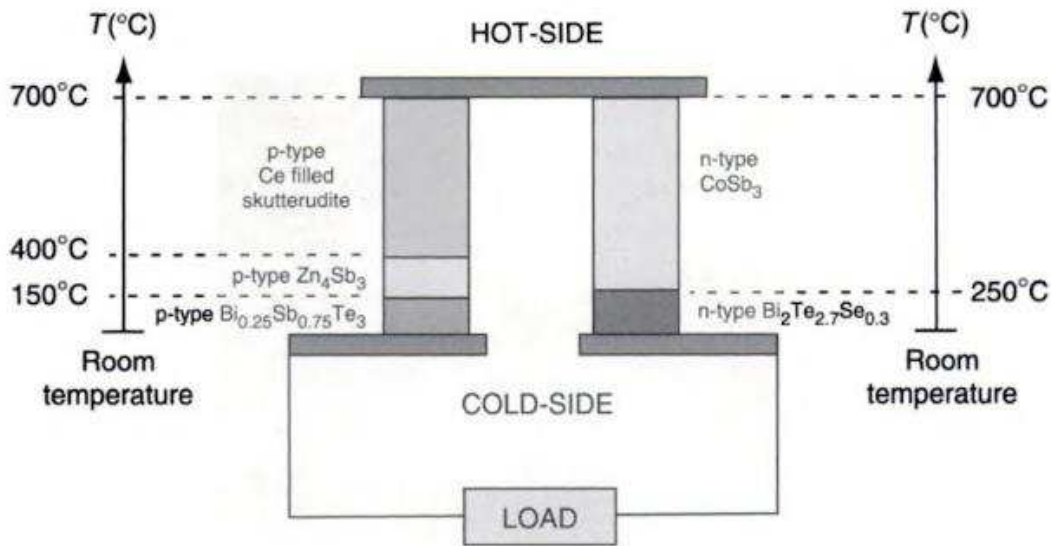


Figure 2.6: Schematic of a high performance multi-segmented thermoelectric generator [1].

A. SEGMENTATION

Thermoelectric efficiency and useful temperature range can be improved from manufacturing a segmented thermoelectric module utilizing different materials stacked together [32], [33]. One popular design is the Bi-Te, PbTe, and Si-Ge stacked in order of rising temperature in order to have highly efficient TE material at low, medium, and high temperature ranges [34]. Another segmented thermoelectric material showing promise includes Bi-Te and FeSi₂ where the manufacturing is the emphasis rather than efficiency optimization [9]. A uni-couple of Bi-Te and Co-Sb showed that the thermoelectric efficiency is doubled compared to a simple Si-Ge TE material [35]. Work done on a Bi-Te and PbTe segmented couple shows that the useful temperature range increased compared to the individual material [11]. Gradation improves the useful temperature range, but there are efficiency losses from the metal contacts joining the segments [35]–[38]. A plot of

individual material is shown in Figure 2.7 along with FGMs, and it shows how combining material as well as using FGM techniques can broaden the temperature bandwidth of TEGs.

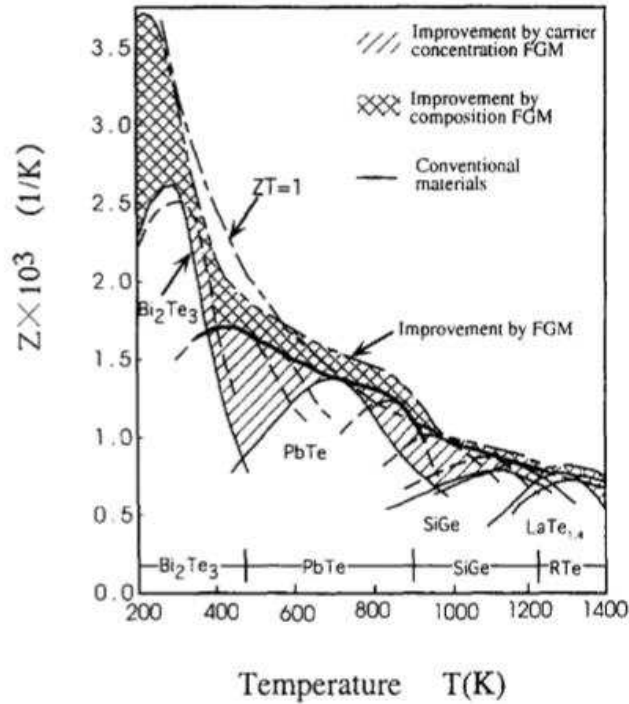


Figure 2.7: Dimensional Z for individual materials, compositional FGMs, and carrier concentration FGMs [39].

B. HOMOGENOUS PROPERTY MANIPULATION

Doping increases the electrical conductivity of a material and increases the thermoelectric power output [40], [41]. Also, Thermal conductivity is significant in thermoelectric material. For bulk material, the thermal conductivity is high compared to lower dimensional samples due to scattering [42]. Nano-structuring of thermoelectric material enhances the overall efficiency by significantly lowering the thermal conductivity [43]. Other strategies to increase disorder in the lattice to decrease lattice thermal conductivity in bulk material includes the use of skutterudites and mixed-lattice atoms such as half-Heusler alloys [44], clathrates that scatter phonons but not electrons [45], and

complex intermetallic phases [46]. For these approaches, manipulating the crystal structure and band gap is very important for increasing the thermoelectric efficiency, and researchers continue to combine techniques to lower the thermal conductivity and enhance the thermoelectric output.

C. FUNCTIONALLY GRADED TEGS

Many thermoelectric designs are based on controlling the electrical resistivity. Researchers have used dopants to change the carrier concentration of the material increasing the electrical conductivity [40], [41]. An approach for enhanced thermoelectric efficiency in FGMs is tuning the peak zT by manipulating the amount of dopant at different spots in the material making it nonhomogeneous. Initially, models were made to verify the benefits of property gradations in thermoelectrics. One study shows that if all three TE properties improve spatially then the overall peak efficiency increases by 30% [47], but it is usually very difficult to improve all properties in one direction in FGMs. Other models and simulations show that a carrier concentration, or compositional gradients will widen the useful temperature range of a thermoelectric material because the zT will peak at different temperatures [39], [48]–[50]. Carrier concentration gradients increased the zT in a study using the Bridgman method of melt material with Bi-Te [51]. A carrier concentration gradient was achieved in a p-type PbTe crystal by unidirectional solidification, but it was doubtful that the process could be controlled for applications [52]. A carrier concentration gradient of indium dopant in PbTe crystals were grown by the Czochralski technique showing that the optimal zT is shifted with temperature [53]. Functionally graded $\text{Ge}_{1-x}\text{Si}_x$ was developed with the Czochralski method in order to achieve a concentration gradient and band gap gradient simultaneously to help optimize the zT for a wide temperature

range [54]. One group even shows a shifted zT with varying doping of PbI_2 in n-type $PbTe$ [55]. Figure 2.8 shows how a carrier concentration can cause the peak zT to shift. FGM based on graded dopant will potentially produce a TEG with wider temperature bandwidth.

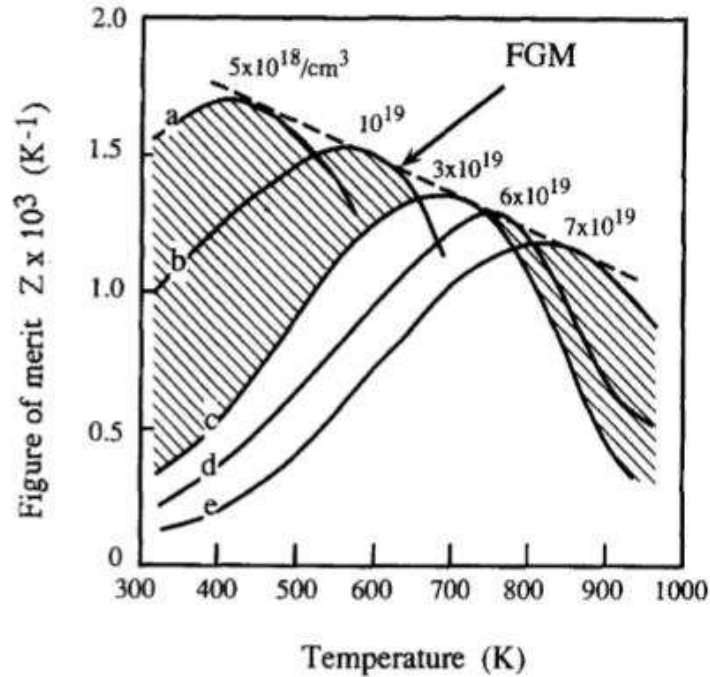


Figure 2.8: Dimensional Z for carrier concentration FGMs [39].

2.7 MODELLING OF TEG FGMS

Modelling of the efficiency versus current or current density is important for the thermoelectric output. It is a popular and well understood model for power output systems. Modelling of a composite thermoelectric material graded from 100% Bi_2Te_3 to 100% $SiGe$ shows that the efficiency is higher for large range of current density compared to the uniform $SiGe$ sample [56]. In this model, the output is shown in Figure 2.9. The gradation is partitioned into discrete layers of material. The enhancement is from the properties at different temperatures based on Bi_2Te_3 having higher efficiency at lower temperature. $SiGe$ has higher efficiency at higher temperature. In this study, the data for

the enhancement of the efficiency versus current density is presented without zT values. They assume a composite of SiGe and PbTe can be made, but no one has done it to date. Their model shows that the FGM has higher efficiency for a large span of current density compared to the homogenous material.

The governing steady-state equation of the temperature of an FGM TEG material is:

$$k\nabla^2 T + \nabla k \nabla T - J \nabla \alpha_S T = -\rho_R J^2 \quad (2.10)$$

where T is the temperature, J is the electric current density, α_S is the Seebeck coefficient, k is the thermal conductivity, and ρ_R is the electrical resistivity. The temperature distribution can be calculated based on the properties as shown below.

$$\begin{aligned} & T \\ = & T_n + \frac{T_{n+1} - T_n}{h_n} (x - x_n) - \frac{\rho_{Rn} J^2}{2k_n} \times [x^2 - (h_n + 2x_n)x \\ & + h_n x_n + x_n^2] \end{aligned} \quad (2.11)$$

If the energy conversion efficiency of the thermoelectric material is given by the following equation,

$$\eta = \frac{P_{out}}{Aq_h} \quad (2.12)$$

where q_h is the heat flux at the hot end of the thermoelectric leg ($x = L$), and P_{out} is the electrical power output from the Seebeck effect and joule heating as such below.

$$\frac{P_{out}}{A} = J \int_0^L \alpha_S \nabla T dx + J^2 \int_0^L \rho_R dx \quad (2.13)$$

Combining the equation of the temperature distribution and the power output into the efficiency equation yields a relationship of the energy efficiency in terms of the TE properties at given temperatures. This relation can be plotted versus the current density showing the efficiency range. In the work of Jin et al. [56], a model of a composite material exhibited a higher efficiency and in a larger current range than the homogenous SiGe thermoelectric. The equation for the efficiency in terms of the thermoelectric properties is given below in (2.14), and the plot from Jin's work is shown below in Figure 2.9. 3-4% higher efficiency is predicted in a large current density range with property gradients that are very small from the hot side to the cold side. Namely, the thermal conductivity transitions from 1.2 W/mK on the cold side to 2.5 W/mK on the hot side, the Seebeck coefficient transitions from 230 $\mu\text{V/K}$ on the cold side to 200 $\mu\text{V/K}$ on the hot side, and the resistivity transitions from $3.1 \times 10^{-5} \Omega\text{-m}$ on the cold side to $2 \times 10^{-5} \Omega\text{-m}$ on the hot side. The equation used to model the efficiency is shown below in (2.14). This approach for modelling TE material is important for the current work because the efficiency outputs are modelled and then experimentally validated in the current study. My study, present in Chapter 4, is the first time that the model developed by Jin et al. has been validated.

$$\eta = \frac{J \sum_{n=0}^N \alpha_{S_N} (T_{n+1} - T_n) + J^2 \sum_{n=0}^N \rho_{R_n} h_n}{-k_N \frac{T_h - T_N}{h_N} + \frac{1}{2} \rho_{R_N} J^2 h_N + J \alpha_{S_N} T_h} \quad (2.14)$$

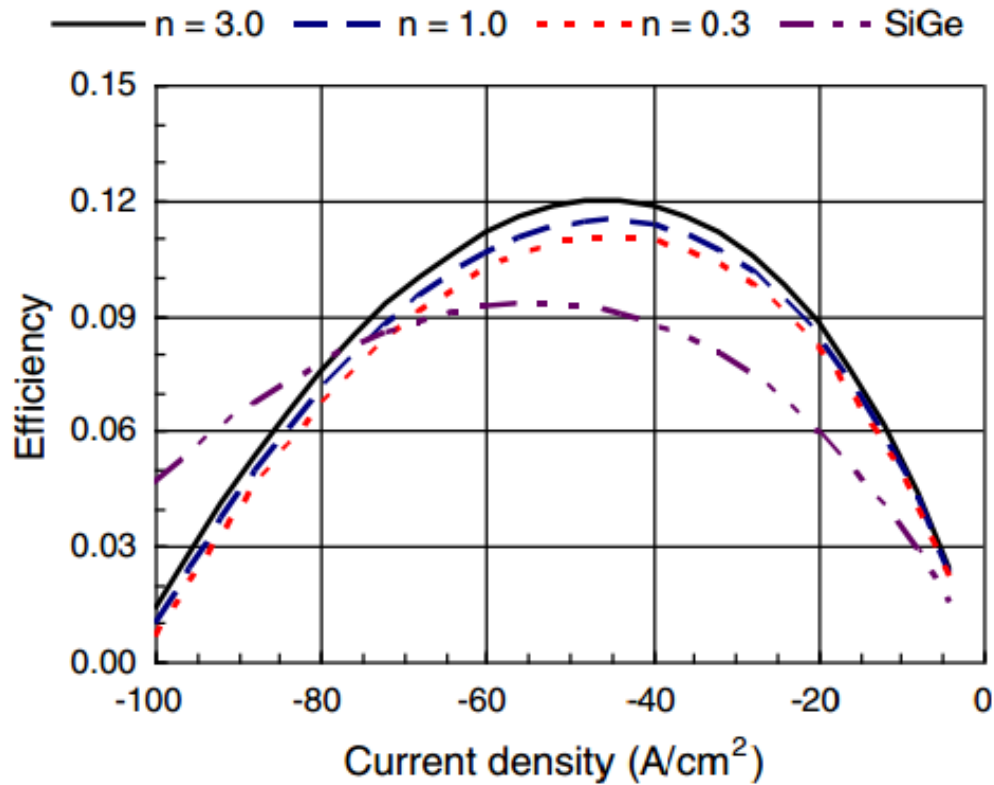


Figure 2.9: Energy conversion efficiency versus electrical current density for a PbTb-SiGe graded nanocomposite of varying gradations, n [56].

2.8 PROCESSING FGMS WITH SINTERING

Sintering is the consolidation of powder to a bulk, solid material. Sintering is a manufacturing technique that allows for the retention of submicron-sized grains in bulk material starting from nano-sized particle or agglomerate powders. Specifically, Spark Plasma Sintering (SPS) uses graphite tooling in soft vacuum to joule heat powders as well as subject the powders to mechanical load to densify the powder into a bulk sample. Some studies show that SPS is a very viable method for manufacturing TEGs because of fast processing, high relative densities, and improved directional properties [57]. Modification in SPS tooling has helped to manufacture parts that were not achievable [58]. Some FGM concepts expressed the need for modified tooling, so improvements in this area have been very necessary. A conical die arrangement is used to induce an in-situ thermal gradient

during the sintering to densify different phases of material at different spots in the die axially [59].

One group created an axial microstructural gradient from fully dense to open porosity in a single step by using an offset die arrangement, which is a die arrangement that creates a thermal gradient across the sintering specimen from increased current density through the offset plunger where there is less contact surface area compared to the other plunger as shown in Figure 2.10 [60]. The concept of an offset die is used in another study to stabilize phases creating the first grain size gradient in an axial sample even though the grain size gradation was not the goal [61]. The first SPS processing of FGM TEGs was designed with modified tooling using a conical die approach intended for microstructural variation control [62]. A layered powder system of $Pb_{1-x}Sn_xTe$ was fabricated with different dopant concentrations using a free sintering method. However, there was no comparison to a sample with homogeneous microstructure[63].

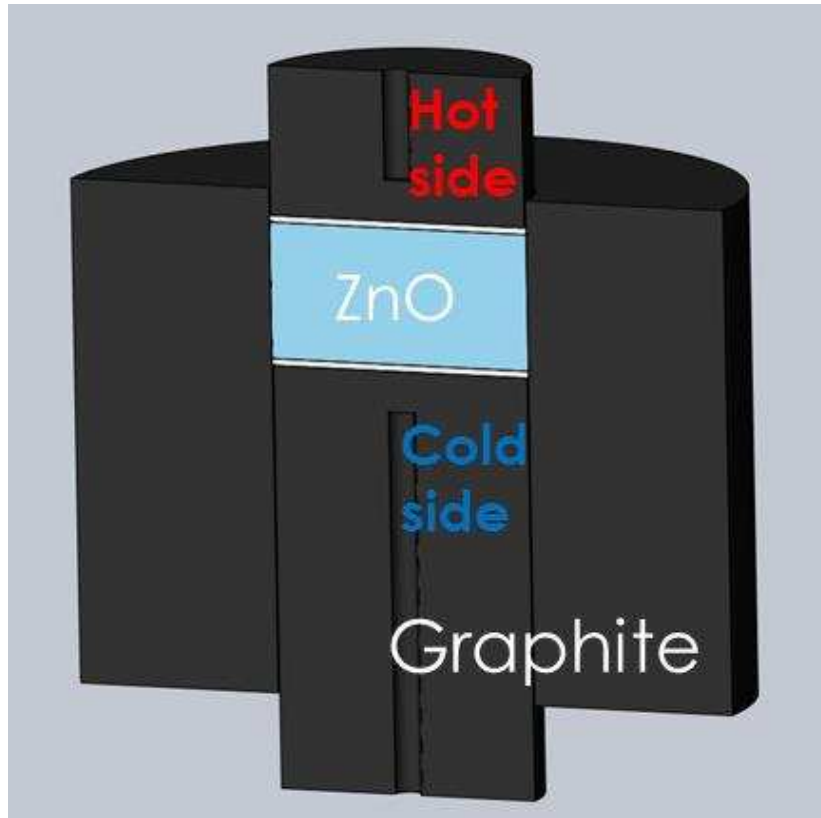


Figure 2.10: Schematic of off-set die arrangement. The hot side is created from a current choke from less contacting area [60].

2.9 SINTERING THEORY

The motivation for processing with sintering and nanopowder is to retain submicron-sized grains to manipulate the properties through microstructure, whether it is porosity, grain size, or phase composition. The intensive, or bulk properties, of a material will not change with the processing methods such as melting point and coefficient of thermal expansion, but some of the extensive properties can be entirely manipulated with microstructure. Sintering is a great method to control microstructure and thus properties. Like the flow chart below in Figure 2.11, the properties will be controlled by the microstructure, and the intrinsic properties will not change. Many of the mechanical

properties depend on grain size [64], [64]–[66], and the thermoelectric properties vary with grain size as well [67]–[69].

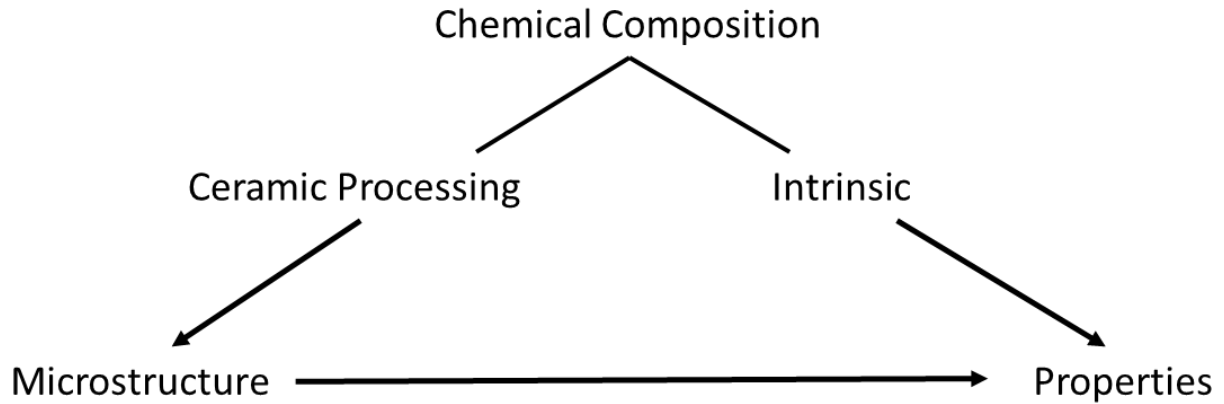


Figure 2.11: Schematic of property hierarchy and manipulation.

A. POWDER PREPARATION

In ceramic processing, the powder plays a significant role on the outcome of the final product in terms of density, consolidation, grain size, grain orientation, pore size, and phases present. For enhanced sintering of advanced ceramics using low dimensional scale, the particle size (nm), particle size distribution, particle shape, state of agglomeration, purity, and phase composition are integrally important for the processing outcome. They all play a role in the thermodynamic driving forces and kinetics of the sintering process which are discussed in Chapters 3, 4, and 5. Figure 2.12 shows a schematic of a powder agglomerate, which is composed of a bunch of particles that have many grains attached to each other. Ideally, the more dispersed the powder is, the better it will be for sintering and retention of submicron grain sizes. In some cases, the powder is not agglomerated much and the particle size can be the grain size, and that is very hard to achieve in synthesis.

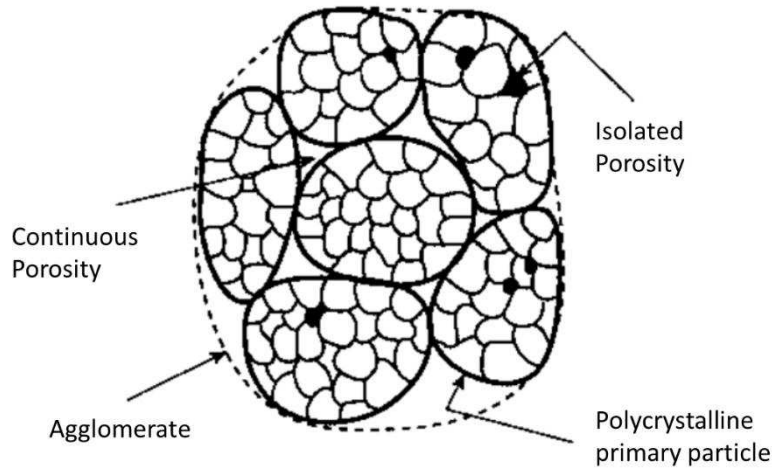


Figure 2.12: Morphological identification of starting powder for sintering [70].

B. SINTERING – PROCESSING OF POWDER COMPACTS

Sintering is the consolidation of a porous body that is accompanied by densification and grain growth resulting in macroscopic shrinkage. The thermodynamic driving force for sintering is energy minimization of interfacial surface free energy of contacting particles where sharp curvature is alleviated. Reduction of interfacial area in powder compacts as well as pore elimination is achieved through atomistic transport or diffusion. Depending on the material system, viscous flow, evaporation-condensation, transport through a liquid phase or solid state diffusion can occur [71]. Accordingly, we differentiate between viscous sintering, liquid phase sintering and solid-state sintering. Solid-state sintering is mostly done in this work with the addition of a transient liquid phase for enhanced solid-state sintering by addition of adsorbed water. Sintering is usually activated by heating the material to temperatures one-half of the melting point. Also, additional mechanical load aids in the sintering process by providing a driving force higher than that from curvature. During the solid-state sintering process, different material transport paths are possible

such as evaporation-condensation, viscous flow, surface diffusion, diffusion through grain boundaries, and diffusion through the lattice. However, only the first two diffusion paths can result in densification because they move the particle centers closer together. In liquid phase sintering, an additional diffusion path is provided by the liquid phase.

The sintering process is divided into the initial, intermediate, and final stages. In solid-state sintering, these stages are defined with respect to density and pore configuration. During the first stage, there is neck formation at the contact points of the particles which brings about cohesion and about 3% density increase as shown in Figure 2.13a. This neck formation occurs via diffusion of atoms from the center of the grain boundary to the neck as a consequence of the gradient in chemical potential. The three sintering stages are preceded by a phase of adhesion, rearrangement and repacking due to the orientation dependent grain boundary energy [70]. During the intermediate stage of sintering, there is a large increase in density, and the pore structure of the sintering body goes from open porosity as on Figure 2.13b to closed porosity as in Figure 2.13c. At densities around 92-95% the final stage begins which is characterized by pore closure, shrinkage and grain growth that result in an incremental increase in density as shown in Figure 2.13d [72].

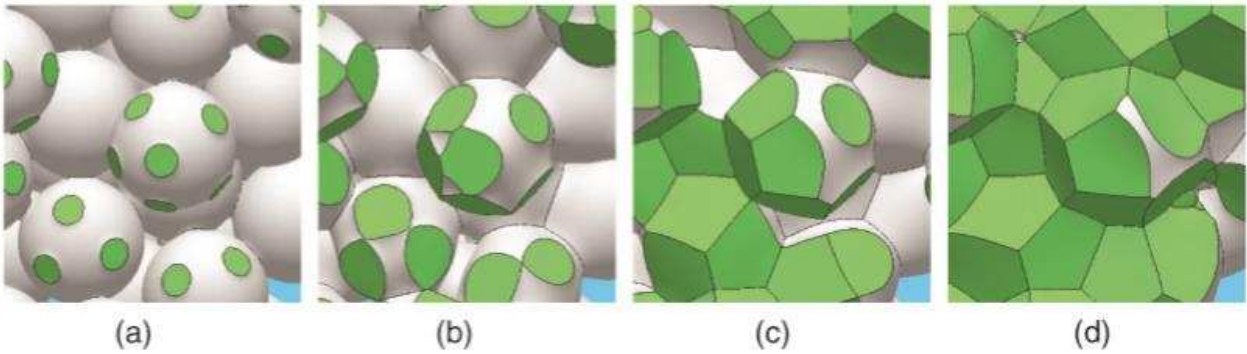


Figure 2.13: Evolution of the microstructure during sintering. a) Initial stage b) intermediate stage (open porosity), c) intermediate stage (onset of pore closure), d) final stage [72].

The sintering potential or sintering stress is a quantity that determines the sintering process. The driving force for sintering is minimizing the free energy of the system caused by surface tension of particles with large surface area. The initial stage of sintering works to reduce the sharp curvature of particle interfaces. The sintering stress is defined as an equivalent externally applied stress that would cause a densification rate equal to that resulting from free sintering [70]. The sintering stress is related to pore surface curvature and interfacial energy as shown below Figure 2.14 and in (2.15). Here, γ_{gb} and γ_{sv} are the free energies of the grain boundary and the solid-vapor interface, respectively. r is the radius of curvature of the pore, G is the grain size, and ψ is the dihedral angle.

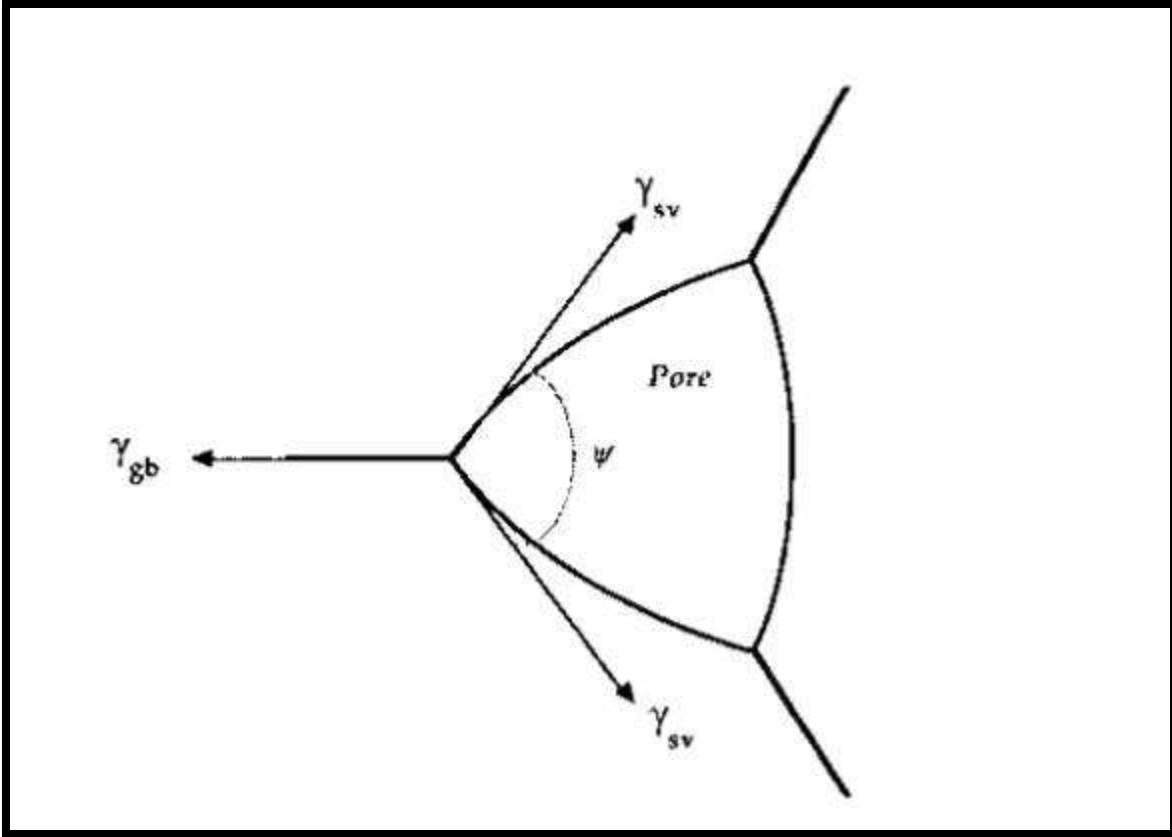


Figure 2.14: Equilibrium shapes of the pores in polycrystalline solids showing the balance between the surface and interfacial forces at the point where the grain boundary intersects the pore [71].

$$\sigma_{DF} = \frac{\gamma_{sv}}{r} + \frac{\gamma_{gb}}{G} \quad (2.15)$$

Once the driving force for sintering is established, it is important to know the diffusion paths that can occur to aid in the sintering process. Diffusion during solid state sintering can occur by surface and bulk transport mechanisms as shown in Figure 2.15. Mass transport can occur along the surface which is called surface diffusion, through the pore space which is called vapor transport, along the grain boundaries which is called grain boundary diffusion, through the lattice which is called volume diffusion bulk diffusion or plastic flow. The first two diffusion paths do not cause the particle centers to approach, so

there is no densification. Whenever mass from the particle interior is deposited at the neck, densification occurs as in bulk and grain boundary diffusion because the two particle centers move closer to each other.

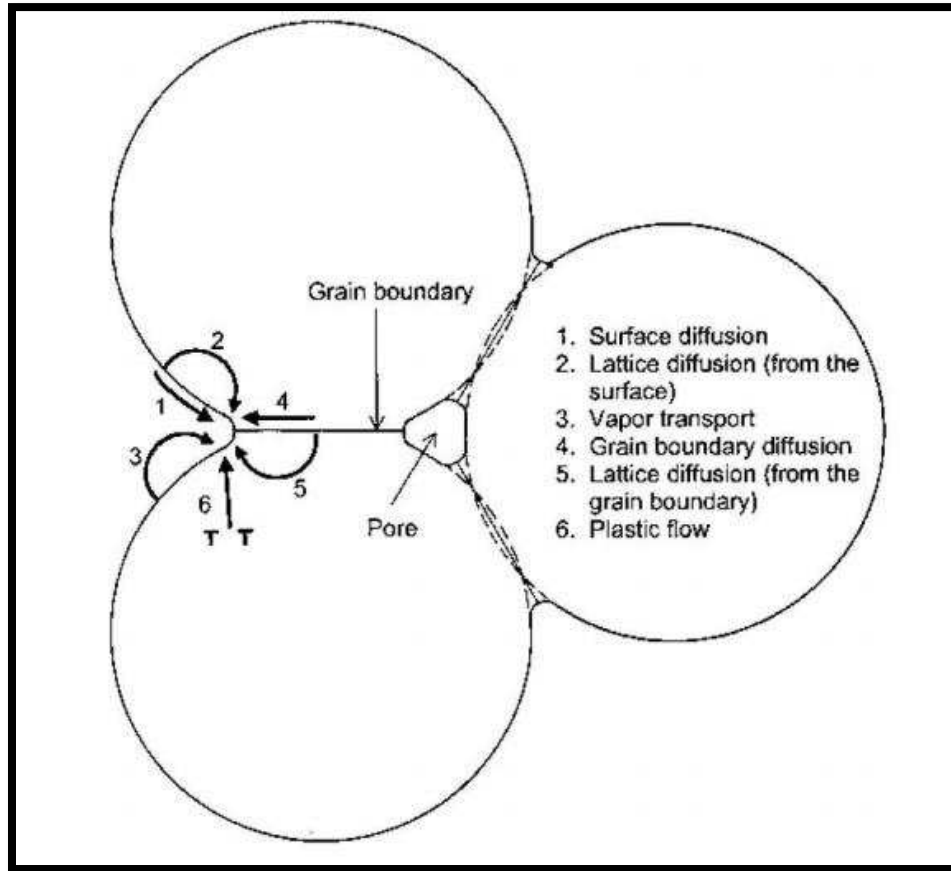


Figure 2.15: Mass transport mechanisms in solid state sintering [71].

When the intermediate stage begins, the driving force shifts from sharp curvature elimination to minimizing the surface area of the particles. Vast densification happens, and the open pore channels begin to close to form isolated pores. The fractional densification rate can be determined from the microscopic properties of the system as shown below where ρ_M is the density, D is the diffusion coefficient, Ω is the atomic volume, k_B is the Boltzmann constant, T is the temperature, G is the grain size, t is time, and m is the

exponent that varies with the mode of diffusion. m is three for lattice diffusion and four for grain boundary diffusion. The densification rate can be determined from shrinkage of the sintering specimens and the microscopic properties can be calculated in a multi-scale problem fashion.

$$\frac{1}{\rho_{MD}} \frac{d\rho_{MD}}{dt} = \frac{D\gamma_{sv}\Omega}{\rho_{MD}k_B T G^m} \quad (2.16)$$

As the later part of the intermediate stage occurs, the densification is paralleled with grain growth, and then the final stage is comprised of mostly small isolated pore closure and significant grain growth. Pores become isolated and no longer have large pinning effects, causing grain growth to dominate the thermodynamics. The grain growth follows the equation below where φ is a shape factor and M_b is the boundary mobility.

$$G^m = G_0^m + 2\varphi\gamma_{gb}M_b t \quad (2.17)$$

C. LIQUID PHASE SINTERING

The liquid phase sintering process is important for water sintering of ZnO because one of the purposed mechanisms for enhanced sintering is a transient liquid phase. The three stages that comprise liquid phase sintering are somewhat different compared to the solid-state sintering. The initial stage includes the rearrangement of solid particles in the liquid phase and is accompanied by a steep increase in density. In the intermediate stage, a solution-precipitation process usually follows. The solid, main component dissolves in the liquid phase to be subsequently precipitated at locations with a lower chemical potential. The final stage is referred to as final pore removal by pore filling and solid-state sintering. It may involve transport of matter along solid-solid contact points. As in solid state

sintering, only a small increase in density is observed during the final stages of sintering [73].

D. PRESSURE ASSISTED SINTERING, CONSTITUTIVE EQUATIONS AND ADVANCED TOPICS

One common difficulty of sintering ceramics is insufficient densification. One solution to this problem that is a common practice for enhanced densification is pressure assisted sintering giving rise to sintering methods such as hot pressing, hot isostatic pressing, hot forging, and spark plasma sintering. Single crystal material deforms under applied compressive stress due to creep by diffusing material from high compressive areas to areas of tension where chemical potential is low. The strain equations for sintering of polycrystalline materials behave similarly. Creep by lattice diffusion is called Nabarro-Herring creep, and creep by grain boundary diffusion is called Coble creep [74]. The equation for the strain rate in Nabarro-Herring creep is shown in (2.18) and resembles the differential densification equation where $\dot{\epsilon}_c$ is the strain rate associated with creep.

$$\dot{\epsilon}_c = \frac{40D_l\Omega p_a}{3kTG^2} \quad (2.18)$$

Because particle rearrangement contributes to the densification through grain boundary sliding, the driving force for sintering is weighted toward the applied pressure rather than the curvature as in free sintering. The densification rate is in equation (2.19), where m is the grain size exponent, ϕ is the stress intensification factor, and τ is the stress exponent:

$$\frac{1}{\rho} \frac{d\rho}{dt} = \frac{D\phi^\tau}{kTG^m} p_a^\tau \quad (2.19)$$

The continuum mechanical description of sintering is commonly applied since it involves macroscopic factors and their influence on densification [75]. The sintering body is viewed as a viscoelastic material whose response to an applied stress is described using a Maxwell element (combination of a spring and a dashpot in series). The viscoelastic response to an applied strain is the superposition of an instantaneous elastic strain and a time dependent deformation by viscous flow or creep [76]. We start with the constitutive equation for an isotropic linear elastic solid where ε_x is the strain on the sintering specimen, ε_f is the free sintering strain rate of the powder used, E is the elastic modulus, and σ is the stress:

$$\varepsilon_x = \varepsilon_f + \frac{1}{E} [\sigma_x - \nu(\sigma_y + \sigma_z)] \quad (2.20)$$

For an isotropic, linearly viscous, incompressible material, the constitutive equation is easily obtained by invoking the elastic-viscous analogy as the strain is replaced with the strain rate and E is replaced with the shear viscosity, η , and ν becomes $\frac{1}{2}$ [77], where $\dot{\varepsilon}_x$ is the strain rate from the dilatometer of a sintering specimen, $\dot{\varepsilon}_f$ is the free sintering strain rate of the powder used, η is the property called shear viscosity, and σ is the stress:

$$\dot{\varepsilon}_x = \dot{\varepsilon}_f + \frac{1}{3\eta} \left[\sigma_x - \frac{1}{2}(\sigma_y + \sigma_z) \right] \quad (2.21)$$

These equations relate the strain and strain rates to the stress during sintering. This is important when analyzing stress shielding effects that arise from varying stress states, or situations where external stresses affect the sintering stress. Since the strains are known, the expected corresponding stress on a sintering system can be estimated from advanced

sintering equations in (2.21). For the above equations, the shear viscosity and the free sintering strain rate can be found [78]–[82].

Constrained sintering is a phenomenon reported in literature that happens when one sintering body experiences differential sintering at different locations. In the current work, the term constrained should not be used for any sintering effects including free sintering because all sintering is essentially constrained. Instead, the term stress shielding is used to explain why inclusions, bimodal powder distributions, and differential strains would hinder sintering. Several factors may lead to stress shielding in sintering, such as sintering with large inclusions, composite sintering, thin-film sintering, and bimodal powder sintering [83]. Stress shielded sintering occurs when external forces act against the sintering stress of a uniform condition [84]–[86]. For thermal gradient sintering, a temperature field creates a varying strain rate field axially where the stress states will most likely be different axially as well. In thin-film sintering where layers of material are sintered directly on the substrate, the stress of adhering the sintering material to the substrate interfere with the sintering stresses. This type of stress interference reduced densification kinetics, cracking, localized porosity, and shape distortion [87]. The issues with stress distribution are explained in sintering with thin films [88], [89]. Also, size inclusions seemed to cause a local pressure change as well [90]. Finally, the sintering of bimodal grain size distribution is explained and analyzed as a pressure shielded sintering problem [91].

The TG sintering phenomenon we will be discussing in this work arises from stage 2 differential sintering under an axial thermal gradient. An axial temperature field causes different strain rates or densification rates along the axial direction of the sintering

specimen. The varying strain rates correlate to varying stress states along the sample. The samples will experience more shrinkage on the hot end while the cold end will have less shrinkage simultaneously. Also, the higher temperature sinters more quickly and will have closed porosity sooner than the underlying material at less temperature. This can cause a stress shielding with different stress states in material that is denser and experiencing higher strain. The varying stress states and possible shielding of stress impedes the colder side densification because it is not exposed to the same stress as the hotter side with less porosity. This transient effect on the sintering specimen hinders the overall densification.

2.10 IMPORTANCE OF ZNO

A. ZNO AS A MULTIFUNCTIONAL MATERIAL

Zinc oxide (ZnO) is a well-known wide band gap n-type semiconductor with energy gap of 3.37 eV and excitation of binding energy of 60 mV making it a great candidate for microelectronic and optoelectronic devices [92]. The conductivity in pure ZnO may be caused by interstitial Zn and oxygen vacancies. Most of the electrical properties are enhanced in nanocrystalline ZnO raising interest for applications, such as transparent electrodes, ultraviolet LEDs, lasers, solar cells, and transistors [93]. ZnO is a promising thermoelectric material at elevated temperatures namely from the high Seebeck coefficient [94]. The electrical conductivity is relatively low and the thermal conductivity is relatively high, so the need to lower these properties is eminent to increase the efficiency. Sintering of ZnO without pressure began in the late 1950s [95]. Early hot press studies on ZnO used very slow heating rates and higher temperatures around 700-900°C [96], [97]. In addition, zinc oxide is relatively easy to process, low cost, and easy to test for properties.

B.SPS/FAST PROCESSING AND LIQUID PHASE ENHANCED TRANSPORT WITH ZNO

Nano-sized particles are sintered to bulk at a fast rate; thus, the grain size of the bulk can be retained in a submicron regime. [98], [99]. Flash sintering [100], [101] and microwave heating [102] provide a rapid heating rate and effectively lower the sintering temperature. Compaction is improved with the addition of acetate phase, which lowers the sintering temperature as well [103]. Sintering aids improved the temperature at which ZnO sinters to 400°C [104], [105]. The addition of adsorbed water into the green compact is thought to assist the densification in three major ways. First is a purposed hydroxide ion mass transport. The second is a transient liquid phase surface transport of the Zn and O ions. The third is a surface cleaning that consumes the carbonate that inhibits mass transport [106]. In a parallel study, the morphology of the water assisted sintered zinc oxide is anisotropic with a bimodal grain size distribution [107]. It is necessary to use water in the amount correlating to 1.5 monolayers of ZnO particle coverage to assist sintering at low temperature to ensure full density for a fully dense sample with submicron-sized grains at 400°C.

C. AL-DOPED ZNO FOR ENHANCED ELECTRICAL CONDUCTIVITY

ZnO is a promising thermoelectric material at elevated temperatures namely from the high Seebeck coefficient [94]. The electrical conductivity is relatively low and the thermal conductivity is relatively high. To increase the electrical conductivity of ZnO thermoelectrics, researchers have used Al-doped ZnO (AZO) to achieve higher carrier concentration [97], [98], [99], [100]. The AZO material has high variability according to the literature but nonetheless has improved the zT [112]–[115]. Spark plasma sintering of AZO was achieved with excellent properties with varying amount of aluminum doping

[116]. Also, many have achieved good sintering results with AZO nanopowders [117]–[119]. The challenge has been lowering the thermal conductivity of the ZnO. Some groups have improved the thermal conductivity with nanostructuring [2], [54], [99]. One study sintered carbon nanotubes in AZO and improved the electric conductivity by about an order of magnitude [121].

2.11 GRAIN SIZE EFFECTS

Grain size plays a significant role in processing. Properties of bulk polycrystalline material depend on the grain size because grain boundaries influence the diffusion paths of electrons, phonons, and dislocations all affecting the electrical, thermal, and mechanical properties, respectively.

A. EFFECTS ON SINTERING

In terms of sintering, the starting particle size plays a large role because the size determines the amount of free surface energy available. Since sintering is the minimization of the total free energy of a powder system through diffusion mechanisms, then more surface area has higher total free energy associated with the material. Green compacts with nano-sized starting powder will have higher driving force for sintering initiating sintering mechanisms at lower temperatures compared to green compacts with larger starting powder size. It is relatively easy to evolve nano-powder into a fully dense material and then use elevated temperature to grow grains to obtain a large-grained system. Retaining submicron-sized material without significant grain growth during sintering can be a challenge. High mechanical load, fast sintering rates, and use of a transient liquid phase can help retain submicron-sized grains [106].

B. EFFECTS ON MATERIAL PROPERTIES

The intrinsic physical properties of sintered material do not change much with different grain size. However, mechanical, electrical and thermal properties, such as mechanical strength, electrical resistivity, and thermal conductivity, can be influenced by the grain size. The grain size introduces boundaries that thermal, electrical, and mechanical carriers need to pass. If these carriers are impeded, then the properties will be greatly affected.

For electrical properties, the Seebeck coefficient and the electrical conductivity are influenced by microstructure because of the statistical interaction of charge carriers with scattering sites or potential barriers known as the grain boundaries. The Seebeck coefficient is shown in (2.22) where n is the carrier concentration; m^* is the effective mass; T is the temperature; k_B is the Stefan-Boltzmann constant; h is Planck's constant, and e is the elementary charge. The effective mass is greatly influenced by the force and potential wells that electrons will see when transporting contributing to grain size effects. The more boundaries, the more scattering and potential wells there are, thus, the Seebeck coefficient will increase with decreasing grain size [68], [122].

$$\alpha_S = \frac{8\pi^2 k_B^2}{3eh^2} m^* T \left(\frac{\pi}{3n}\right)^{\frac{2}{3}} \quad (2.22)$$

The electrical conductivity (σ_C) and electric resistivity (ρ_R) are related to the carrier density and the carrier mobility, μ . The mobility gives a measure of how well the electrical carriers flow through the material. The grain size affects the electric conductivity because the scattering sites decrease the mobility of the carriers, so decreasing grain size will decrease the electrical conductivity in most cases [123]–[125].

$$\sigma_C = \frac{1}{\rho_R} = ne\mu \quad (2.23)$$

Thermal conductivity comes from two sources:(1) electrons transporting heat (κ_e) and (2) phonons travelling through the lattice (κ_l).

$$k=k_e + k_l \quad (2.24)$$

$$k_e = L_L\sigma_C T = ne\mu L_L T \quad (2.25)$$

Most of the electronic term (κ_e) of thermal conductivity is directly related to the electrical conductivity through the Wiedemann–Franz law, where L_L is the Lorenz factor, $2.4 \times 10^{-8} \text{ J}^2\text{K}^{-2}\text{C}^{-2}$ for free electrons. Decreasing the grain size enhances phonon dispersion due to increased number of collisions that effectively decrease the thermal conductivity [126].

Grain boundaries affect the mechanical properties by impeding dislocation motion which is essential in determining a material's strength, ductility, and hardness. The relationship between the grain size and the strength of a material is shown below in (2.26) which is the Hall-Petch relationship where σ_y is the yield stress, σ_0 is the starting stress for dislocation motion, k_y is the strengthening coefficient, and G is the grain size. The Hall-Petch relationship [65], [66], [127] directly shows how the grain size affects the strength of a material. Increased strength is from hindered dislocation motion along slip planes. The dislocations pile up at boundaries where they will repel each other. For small grains, there is less dislocation density, so the dislocation pile-up in small-grained samples will be smaller than in large-grain samples. The higher dislocation pile-up with larger grain

samples will require less stress to cause failure in the grain boundary. This gives materials with small grains more strength and hardness. Small grains will not be as resilient to plastic flow and will be less ductile.

$$\sigma_y = \sigma_0 + \frac{k_y}{\sqrt{G}} \quad (2.26)$$

REFERENCES

- [1] D. M. Rowe, *Thermoelectrics Handbook: Macro to Nano*. CRC Press, 2005.
- [2] G. J. Snyder and E. S. Toberer, "Complex thermoelectric materials," *Nat. Mater.*, vol. 7, no. 2, pp. 105–114, Feb. 2008.
- [3] B. Sherman, R. R. Heikes, and R. W. U. Jr, "Calculation of Efficiency of Thermoelectric Devices," *J. Appl. Phys.*, vol. 31, no. 1, pp. 1–16, Jan. 1960.
- [4] "Misfit layered Ca₃Co₄O₉ as a high figure of merit p-type transparent conducting oxide film through solution processing," *Appl. Phys. Lett.*, vol. 104, no. 16, p. 161901, Apr. 2014.
- [5] L. T. Hung *et al.*, "High performance p-type segmented leg of misfit-layered cobaltite and half-Heusler alloy," *Energy Convers. Manag.*, vol. 99, pp. 20–27, Jul. 2015.
- [6] H. Takahashi, T. Ishikawa, D. Okugawa, and T. Hashida, "Laser and Plasma-Arc Thermal Shock/Fatigue Fracture Evaluation Procedure for Functionally Gradient Materials," in *Thermal Shock and Thermal Fatigue Behavior of Advanced Ceramics*, D. G. A. Schneider and P. D. D. h c mult G. Petzow, Eds. Springer Netherlands, 1993, pp. 543–554.
- [7] S. W. Angrist, *Direct energy conversion*. Allyn and Bacon, 1982.
- [8] C. L. Cramer, "Thermoelectric properties of Si/SiC thin-film superlattices grown by ion beam sputtering," M.S. Thesis. Colorado State University, 2015.
- [9] J. Schilz, L. Helmers, Y. S. Kang, Y. Noda, and M. Niino, "Bismuth-telluride/iron-disilicide segmented thermoelectric elements: patterning, preparation and properties," in *XVI International Conference on Thermoelectrics, 1997. Proceedings ICT '97*, 1997, pp. 375–378.
- [10] Y. S. Kang *et al.*, "Evaluation of monolithic and segmented thermoelectric materials by using a large-temperature-span apparatus," in *XVI International Conference on Thermoelectrics, 1997. Proceedings ICT '97*, 1997, pp. 390–393.
- [11] Y. Noda, Y.-S. Kang, and M. Niino, "Preparation and characterization of segmented-type thermoelectric branches of Bi₂Te₃/PbTe," in *XVI International Conference on Thermoelectrics, 1997. Proceedings ICT '97*, 1997, pp. 371–374.
- [12] V. Ravi *et al.*, "Thermal Expansion Studies of Selected High-Temperature Thermoelectric Materials," *J. Electron. Mater.*, vol. 38, no. 7, pp. 1433–1442, Jul. 2009.
- [13] B. L. Wang, Y. B. Guo, and C. W. Zhang, "Cracking and thermal shock resistance of a Bi₂Te₃ based thermoelectric material," *Eng. Fract. Mech.*, vol. 152, pp. 1–9, Feb. 2016.
- [14] B.-L. Wang and Y.-W. Mai, "On Thermal Shock Behavior of Functionally Graded Materials," *J. Therm. Stress.*, vol. 30, no. 6, pp. 523–558, Apr. 2007.
- [15] Y. Isoda, Y. Shinohara, Y. Imai, I. A. Nishida, and O. Ohashi, "Thermal Shock Resistance and Thermoelectric Properties of Boron Doped Iron Disilicides," *J. Jpn. Inst. Met.*, vol. 63, no. 3, pp. 391–396, 1999.
- [16] L. Bakhtaryfard and Y. S. Chen, "Design and Analysis of a Thermoelectric Module to Improve the Operational Life," *Adv. Mech. Eng.*, vol. 7, no. 1, p. 152419, Jan. 2015.
- [17] D. P. H. Hasselman, "Unified Theory of Thermal Shock Fracture Initiation and Crack Propagation in Brittle Ceramics," *J. Am. Ceram. Soc.*, vol. 52, no. 11, pp. 600–604, Nov. 1969.

- [18] R. M. Mahamood and E. T. Akinlabi, "Types of Functionally Graded Materials and Their Areas of Application," in *Functionally Graded Materials*, Springer, Cham, 2017, pp. 9–21.
- [19] M. R. Vaziri, S. M. Nowruzpour Mehrian, M. H. Naei, and J. Y. Sheikh Ahmad, "Modification of Shock Resistance for Cutting Tools Using Functionally Graded Concept in Multilayer Coating," *J. Therm. Sci. Eng. Appl.*, vol. 7, no. 1, pp. 011014-011014-8, Mar. 2015.
- [20] Z. Jun, A. Xing, D. Jianxin, and W. Jinghai, "Thermal shock behaviors of functionally graded ceramic tool materials," *J. Eur. Ceram. Soc.*, vol. 24, no. 5, pp. 847–854, 2004.
- [21] G. Zheng, J. Zhao, Z. Gao, and Q. Cao, "Cutting performance and wear mechanisms of Sialon-Si₃N₄ graded nano-composite ceramic cutting tools," *Int. J. Adv. Manuf. Technol.*, vol. 58, no. 1–4, pp. 19–28, Jan. 2012.
- [22] Q. Xue, X. Ai, J. Zhao, Y. Liu, and Y. Zhou, "Analysis of microstructure and mechanical properties of graded nano-composite Si₃N₄-based ceramic cutting tool material," in *Proceedings of 2011 International Conference on Electronic Mechanical Engineering and Information Technology*, 2011, vol. 7, pp. 3539–3542.
- [23] Y. Hori, D. Kusano, T. Ito, and K. Izumi, "Analysis on thermo-mechanical stress of thermoelectric module," in *Eighteenth International Conference on Thermoelectrics*, 1999, 1999, pp. 328–331.
- [24] Y. Nakatani, R. Takaku, T. Hino, T. Shindo, and Y. Itoh, "Mechanical Aspects of Structural Optimization in a Bi-Te Thermoelectric Module for Power Generation," *MRS Online Proc. Libr. Arch.*, vol. 842, Jan. 2004.
- [25] E. Hatzikraniotis, K. T. Zorbas, I. Samaras, T. Kyratsi, and K. M. Paraskevopoulos, "Efficiency Study of a Commercial Thermoelectric Power Generator (TEG) Under Thermal Cycling," *J. Electron. Mater.*, vol. 39, no. 9, pp. 2112–2116, Sep. 2010.
- [26] A. S. Al-Merbaty, B. S. Yilbas, and A. Z. Sahin, "Thermodynamics and thermal stress analysis of thermoelectric power generator: Influence of pin geometry on device performance," *Appl. Therm. Eng.*, vol. 50, no. 1, pp. 683–692, Jan. 2013.
- [27] U. Erturun, K. Erermis, and K. Mossi, "Effect of various leg geometries on thermo-mechanical and power generation performance of thermoelectric devices," *Appl. Therm. Eng.*, vol. 73, no. 1, pp. 128–141, 2014.
- [28] Z.-H. Jin and G. H. Paulino, "Transient thermal stress analysis of an edge crack in a functionally graded material," *Int. J. Fract.*, vol. 107, no. 1, pp. 73–98, Jan. 2001.
- [29] M. Sribalaji, B. Mukherjee, S. R. Bakshi, P. Arunkumar, K. Suresh Babu, and A. K. Keshri, "In-situ formed graphene nanoribbon induced toughening and thermal shock resistance of spark plasma sintered carbon nanotube reinforced titanium carbide composite," *Compos. Part B Eng.*, vol. 123, pp. 227–240, Aug. 2017.
- [30] Z. Wang, C. Hong, X. Zhang, X. Sun, and J. Han, "Microstructure and thermal shock behavior of ZrB₂-SiC-graphite composite," *Mater. Chem. Phys.*, vol. 113, no. 1, pp. 338–341, Jan. 2009.
- [31] Rowe, D. M. (Ed.). *Materials, preparation, and characterization in thermoelectrics* (Vol. 1). CRC press. 2012.
- [32] J. Schilz, L. Helmers, W. E. Müller, and M. Niino, "A local selection criterion for the composition of graded thermoelectric generators," *J. Appl. Phys.*, vol. 83, no. 2, pp. 1150–1152, Jan. 1998.

- [33] E. Müller, Č. Drašar, J. Schilz, and W. A. Kaysser, "Functionally graded materials for sensor and energy applications," *Mater. Sci. Eng. A*, vol. 362, no. 1–2, pp. 17–39, Dec. 2003.
- [34] Schilz, J., L. Helmers, Y. S. Kang, Y. Noda, and M. Niino. "Bismuth-telluride/iron-disilicide segmented thermoelectric elements: patterning, preparation and properties." In *Thermoelectrics, 1997. Proceedings ICT'97. XVI International Conference on*, pp. 375-378. IEEE, 1997.
- [35] M. S. El-Genk and H. H. Saber, "High efficiency segmented thermoelectric uncouple for operation between 973 and 300 K," *Energy Convers. Manag.*, vol. 44, no. 7, pp. 1069–1088, May 2003.
- [36] M. S. El-Genk, H. H. Saber, and T. Caillat, "A performance comparison of SiGe and skutterudite based segmented thermoelectric devices," in *AIP Conference Proceedings*, 2002, vol. 608, pp. 1007–1015.
- [37] P. H. Ngan *et al.*, "Towards high efficiency segmented thermoelectric uncouples," *Phys. Status Solidi A*, vol. 211, no. 1, pp. 9–17, Jan. 2014.
- [38] T. T. Wallace, Z.-H. Jin, and J. Su, "Efficiency of a Sandwiched Thermoelectric Material with a Graded Interlayer and Temperature-Dependent Properties," *J. Electron. Mater.*, vol. 45, no. 4, pp. 2142–2149, Feb. 2016.
- [39] M. Koizumi, "FGM activities in Japan," *Compos. Part B Eng.*, vol. 28, no. 1–2, pp. 1–4, 1997.
- [40] O. Yamashita, S. Tomiyoshi, and K. Makita, "Bismuth telluride compounds with high thermoelectric figures of merit," *J. Appl. Phys.*, vol. 93, no. 1, pp. 368–374, Jan. 2003.
- [41] S. Ohta, T. Nomura, H. Ohta, and K. Koumoto, "High-temperature carrier transport and thermoelectric properties of heavily La- or Nb-doped SrTiO₃ single crystals," *J. Appl. Phys.*, vol. 97, no. 3, p. 034106, Feb. 2005.
- [42] M. S. Dresselhaus *et al.*, "New Directions for Low-Dimensional Thermoelectric Materials," *Adv. Mater.*, vol. 19, no. 8, pp. 1043–1053, Apr. 2007.
- [43] G. Chen, M. S. Dresselhaus, G. Dresselhaus, J.-P. Fleurial, and T. Caillat, "Recent developments in thermoelectric materials," *Int. Mater. Rev.*, vol. 48, no. 1, pp. 45–66, Feb. 2003.
- [44] G. S. Nolas, J. Poon, and M. Kanatzidis, "Recent Developments in Bulk Thermoelectric Materials," *MRS Bull.*, vol. 31, no. 03, pp. 199–205, Mar. 2006.
- [45] B. B. Iversen *et al.*, "Why are Clathrates Good Candidates for Thermoelectric Materials?," *J. Solid State Chem.*, vol. 149, no. 2, pp. 455–458, Feb. 2000.
- [46] S. M. Kauzlarich, S. R. Brown, and G. Jeffrey Snyder, "Zintl phases for thermoelectric devices," *Dalton Trans.*, no. 21, p. 2099, 2007.
- [47] Z.-H. Jin, T. T. Wallace, R. J. Lad, and J. Su, "Energy Conversion Efficiency of an Exponentially Graded Thermoelectric Material," *J. Electron. Mater.*, vol. 43, no. 2, pp. 308–313, Nov. 2013.
- [48] E. Müller, Č. Drašar, J. Schilz, and W. A. Kaysser, "Functionally graded materials for sensor and energy applications," *Mater. Sci. Eng. A*, vol. 362, no. 1–2, pp. 17–39, Dec. 2003.
- [49] Z. Dashevsky, Y. Gelbstein, I. Edry, I. Drabkin, and M. P. Dariel, "Optimization of thermoelectric efficiency in graded materials," in *Thermoelectrics, 2003 Twenty-Second International Conference on - ICT*, 2003, pp. 421–424.

- [50] A. E. Kaliazin, V. L. Kuznetsov, and D. M. Rowe, "Rigorous calculations related to functionally graded and segmented thermoelements," in *XX International Conference on Thermoelectrics, 2001. Proceedings ICT 2001*, 2001, pp. 286–292.
- [51] V. L. Kuznetsov, L. A. Kuznetsova, A. E. Kaliazin, and D. M. Rowe, "High performance functionally graded and segmented Bi₂Te₃-based materials for thermoelectric power generation," *J. Mater. Sci.*, vol. 37, no. 14, pp. 2893–2897, Jul. 2002.
- [52] M. P. Dariel, Z. Dashevsky, A. Jarashnely, S. Shusterman, and A. Horowitz, "Carrier concentration gradient generated in p-type PbTe crystals by unidirectional solidification," *J. Cryst. Growth*, vol. 234, no. 1, pp. 164–170, Jan. 2002.
- [53] Z. Dashevsky, S. Shusterman, M. P. Dariel, and I. Drabkin, "Thermoelectric efficiency in graded indium-doped PbTe crystals," *J. Appl. Phys.*, vol. 92, no. 3, pp. 1425–1430, Aug. 2002.
- [54] E. M. J. Hedegaard, S. Johnsen, L. Bjerg, K. A. Borup, and B. B. Iversen, "Functionally Graded Ge_{1-x}Si_x Thermoelectrics by Simultaneous Band Gap and Carrier Density Engineering," *Chem. Mater.*, vol. 26, no. 17, pp. 4992–4997, Sep. 2014.
- [55] Y. Gelbstein, Z. Dashevsky, and M. P. Dariel, "High performance n-type PbTe-based materials for thermoelectric applications," *Phys. B Condens. Matter*, vol. 363, no. 1–4, pp. 196–205, Jun. 2005.
- [56] Z.-H. Jin and T. T. Wallace, "Functionally Graded Thermoelectric Materials with Arbitrary Property Gradations: A One-Dimensional Semianalytical Study," *J. Electron. Mater.*, vol. 44, no. 6, pp. 1444–1449, Jun. 2015.
- [57] W.-T. Chiu, C.-L. Chen, and Y.-Y. Chen, "A strategy to optimize the thermoelectric performance in a spark plasma sintering process," *Sci. Rep.*, vol. 6, p. 23143, Mar. 2016.
- [58] D. Giuntini, J. Raethel, M. Herrmann, A. Michaelis, and E. A. Olevsky, "Advancement of Tooling for Spark Plasma Sintering," *J. Am. Ceram. Soc.*, vol. 98, no. 11, pp. 3529–3537, Nov. 2015.
- [59] C.-Q. Hong, X.-H. Zhang, W.-J. Li, J.-C. Han, and S.-H. Meng, "A novel functionally graded material in the ZrB₂-SiC and ZrO₂ system by spark plasma sintering," *Mater. Sci. Eng. A*, vol. 498, no. 1–2, pp. 437–441, Dec. 2008.
- [60] D. M. Hulbert, D. Jiang, U. Anselmi-Tamburini, C. Unuvar, and A. K. Mukherjee, "Continuous functionally graded boron carbide-aluminum nanocomposites by spark plasma sintering," *Mater. Sci. Eng. A*, vol. 493, no. 1–2, pp. 251–255, Oct. 2008.
- [61] M. Belmonte, J. Gonzalez-Julian, P. Miranzo, and M. I. Osendi, "Continuous in situ functionally graded silicon nitride materials," *Acta Mater.*, vol. 57, no. 9, pp. 2607–2612, May 2009.
- [62] L. P. Bulat *et al.*, "On fabrication of functionally graded thermoelectric materials by spark plasma sintering," *Tech. Phys. Lett.*, vol. 40, no. 11, pp. 972–975, Dec. 2014.
- [63] Y. Gelbstein, Z. Dashevsky, and M. P. Dariel, "Powder metallurgical processing of functionally graded p-Pb_{1-x}Sn_xTe materials for thermoelectric applications," *Phys. B Condens. Matter*, vol. 391, no. 2, pp. 256–265, Apr. 2007.
- [64] R. Chaim and M. Hefetz, "Effect of grain size on elastic modulus and hardness of nanocrystalline ZrO₂-3 wt% Y₂O₃ ceramic," *J. Mater. Sci.*, vol. 39, no. 9, pp. 3057–3061, May 2004.
- [65] R. W. Rice, C. C. Wu, and F. Boichelt, "Hardness-Grain-Size Relations in Ceramics," *J. Am. Ceram. Soc.*, vol. 77, no. 10, pp. 2539–2553, Oct. 1994.

- [66] N. Hansen, "Hall–Petch relation and boundary strengthening," *Scr. Mater.*, vol. 51, no. 8, pp. 801–806, Oct. 2004.
- [67] M. Takashiri, K. Miyazaki, S. Tanaka, J. Kurosaki, D. Nagai, and H. Tsukamoto, "Effect of grain size on thermoelectric properties of n-type nanocrystalline bismuth-telluride based thin films," *J. Appl. Phys.*, vol. 104, no. 8, p. 084302, Oct. 2008.
- [68] Y. Gao, Y. He, and L. Zhu, "Impact of grain size on the Seebeck coefficient of bulk polycrystalline thermoelectric materials," *Chin. Sci. Bull.*, vol. 55, no. 1, pp. 16–21, Jan. 2010.
- [69] W. Kim, "Strategies for engineering phonon transport in thermoelectrics," *J. Mater. Chem. C*, vol. 3, no. 40, pp. 10336–10348, Oct. 2015.
- [70] M. N. Rahaman, *Ceramic processing and sintering*. CRC, 2003.
- [71] M. N. Rahaman, *Ceramic Processing and Sintering*. CRC Press, 2003.
- [72] F. Wakai, "Modeling and Simulation of Elementary Processes in Ideal Sintering," *J. Am. Ceram. Soc.*, vol. 89, no. 5, pp. 1471–1484, May 2006.
- [73] S.-J. L. Kang, *Sintering: Densification, Grain Growth and Microstructure*. Butterworth-Heinemann, 2004.
- [74] R. M. German, *Sintering Theory and Practice*. 1996.
- [75] E. A. Olevsky, "Theory of sintering: from discrete to continuum," *Mater. Sci. Eng. R Rep.*, vol. 23, no. 2, pp. 41–100, Jun. 1998.
- [76] J. S. Reed, *Principles of Ceramics Processing*, 2nd ed. Wiley VHC, 1995.
- [77] R. M. Christensen, "Chapter I - Viscoelastic Stress Strain Constitutive Relations," in *Theory of Viscoelasticity (SECOND EDITION)*, Academic Press, 1982, pp. 1–34.
- [78] E. Olevsky and L. Froyen, "Constitutive modeling of spark-plasma sintering of conductive materials," *Scr. Mater.*, vol. 55, no. 12, pp. 1175–1178, Dec. 2006.
- [79] E. A. Olevsky, V. Tikare, and T. Garino, "Multi-Scale Study of Sintering: A Review," *J. Am. Ceram. Soc.*, vol. 89, no. 6, pp. 1914–1922, Jun. 2006.
- [80] R. Zuo, E. Aulbach, and J. Rödel, "Viscous Poisson's coefficient determined by discontinuous hot forging," *J. Mater. Res.*, vol. 18, no. 9, pp. 2170–2176, Sep. 2003.
- [81] R. Zuo and J. Rödel, "Temperature dependence of constitutive behaviour for solid-state sintering of alumina," *Acta Mater.*, vol. 52, no. 10, pp. 3059–3067, Jun. 2004.
- [82] S.-H. Lee, G. L. Messing, and D. J. Green, "Bending Creep Test to Measure the Viscosity of Porous Materials during Sintering," *J. Am. Ceram. Soc.*, vol. 86, no. 6, pp. 877–882, Jun. 2003.
- [83] L. C. De Jonghe, M. N. Rahaman, and C. H. Hsueh, "Transient stresses in bimodal compacts during sintering," *Acta Metall.*, vol. 34, no. 7, pp. 1467–1471, Jul. 1986.
- [84] R. K. Bordia and G. W. Scherer, "On constrained sintering—I. Constitutive model for a sintering body," *Acta Metall.*, vol. 36, no. 9, pp. 2393–2397, Sep. 1988.
- [85] R. K. Bordia and G. W. Scherer, "On constrained sintering—II. Comparison of constitutive models," *Acta Metall.*, vol. 36, no. 9, pp. 2399–2409, Sep. 1988.
- [86] R. K. Bordia and G. W. Scherer, "On constrained sintering—III. Rigid inclusions," *Acta Metall.*, vol. 36, no. 9, pp. 2411–2416, Sep. 1988.
- [87] C. C. Jamin, "Constrained Sintering of Patterned Ceramic Films on Stiff Substrates," Ph.D. Thesis, Technische Universität, Darmstadt, 2014.
- [88] T. Rabe, W. A. Schiller, T. Hochheimer, C. Modes, and A. Kipka, "Zero Shrinkage of LTCC by Self-Constrained Sintering," *Int. J. Appl. Ceram. Technol.*, vol. 2, no. 5, pp. 374–382, Sep. 2005.

- [89] S.-Y. Tzeng and J.-H. Jean, "Stress Development during Constrained Sintering of Alumina/Glass/Alumina Sandwich Structure," *J. Am. Ceram. Soc.*, vol. 85, no. 2, pp. 335–340, Feb. 2002.
- [90] Y. Nakada and T. Kimura, "Effects of Shape and Size of Inclusions on the Sintering of ZnO—ZrO₂ Composites," *J. Am. Ceram. Soc.*, vol. 80, no. 2, pp. 401–406, Feb. 1997.
- [91] R. M. German, "Prediction of sintered density for bimodal powder mixtures," *Metall. Trans. A*, vol. 23, no. 5, pp. 1455–1465, May 1992.
- [92] C.-W. Nahm, "Nonohmic properties of V/Mn/Nb/Gd co-doped zinc oxide semiconducting varistors with low-temperature sintering process," *Mater. Sci. Semicond. Process.*, vol. 23, pp. 58–62, Jul. 2014.
- [93] R. N. Viswanath, S. Ramasamy, R. Ramamoorthy, P. Jayavel, and T. Nagarajan, "Preparation and characterization of nanocrystalline ZnO based materials for varistor applications," *Nanostructured Mater.*, vol. 6, no. 5–8, pp. 993–996, 1995.
- [94] K. H. Kim, S. H. Shim, K. B. Shim, K. Niihara, and J. Hojo, "Microstructural and Thermoelectric Characteristics of Zinc Oxide-Based Thermoelectric Materials Fabricated Using a Spark Plasma Sintering Process," *J. Am. Ceram. Soc.*, vol. 88, no. 3, pp. 628–632, Mar. 2005.
- [95] T. J. Gray, "Sintering of Zinc Oxide," *J Am Ceram Soc*, vol. 37, no. 11, 1954.
- [96] M. Mazaheri, S. A. Hassanzadeh-Tabrizi, and S. K. Sadrnezhaad, "Hot pressing of nanocrystalline zinc oxide compacts: Densification and grain growth during sintering," *Ceram. Int.*, vol. 35, no. 3, pp. 991–995, Apr. 2009.
- [97] J. Langer, M. J. Hoffmann, and O. Guillon, "Electric Field-Assisted Sintering and Hot Pressing of Semiconductive Zinc Oxide: A Comparative Study," *J. Am. Ceram. Soc.*, vol. 94, no. 8, pp. 2344–2353, Aug. 2011.
- [98] A. P. Hynes, R. H. Doremus, and R. W. Siegel, "Sintering and characterization of nanophase zinc oxide," *J. Am. Ceram. Soc.*, vol. 85, no. 8, pp. 1979–1987, 2002.
- [99] L. Gao, Q. Li, W. Luan, H. Kawaoka, T. Sekino, and K. Niihara, "Preparation and Electric Properties of Dense Nanocrystalline Zinc Oxide Ceramics," *J. Am. Ceram. Soc.*, vol. 85, no. 4, pp. 1016–1018, Apr. 2002.
- [100] C. Schmerbauch, J. Gonzalez-Julian, R. Röder, C. Ronning, and O. Guillon, "Flash Sintering of Nanocrystalline Zinc Oxide and its Influence on Microstructure and Defect Formation," *J. Am. Ceram. Soc.*, vol. 97, no. 6, pp. 1728–1735, Jun. 2014.
- [101] Y. Zhang and J. Luo, "Promoting the flash sintering of ZnO in reduced atmospheres to achieve nearly full densities at furnace temperatures of <120 °C," *Scr. Mater.*, vol. 106, pp. 26–29, Sep. 2015.
- [102] R. F. K. Gunnewiek and R. H. G. A. Kiminami, "Effect of heating rate on microwave sintering of nanocrystalline zinc oxide," *Ceram. Int.*, vol. 40, no. 7, Part B, pp. 10667–10675, Aug. 2014.
- [103] J. G.-J. Benjamin Dargatz, "Improved compaction of ZnO nano-powder triggered by the presence of acetate and its effect on sintering," *Sci. Technol. Adv. Mater.*, vol. 16, no. 2, p. 025008, 2015.
- [104] J. G.-J. Benjamin Dargatz, "Effect of electric field and atmosphere on the processing of nanocrystalline ZnO," *Proc. SPIE - Int. Soc. Opt. Eng.*, vol. 8987, 2014.
- [105] S. Schwarz, A. M. Thron, J. Rufner, K. Benthem, and O. Guillon, "Low Temperature Sintering of Nanocrystalline Zinc Oxide: Effect of Heating Rate Achieved by Field

- Assisted Sintering/Spark Plasma Sintering," *J. Am. Ceram. Soc.*, vol. 95, no. 8, pp. 2451–2457, Aug. 2012.
- [106] B. Dargatz *et al.*, "FAST/SPS sintering of nanocrystalline zinc oxide—Part I: Enhanced densification and formation of hydrogen-related defects in presence of adsorbed water," *J. Eur. Ceram. Soc.* 36.5 (2016): 1207-1220.
- [107] B. Dargatz, J. Gonzalez-Julian, M. Bram, Y. Shinoda, F. Wakai, and O. Guillon, "FAST/SPS sintering of nanocrystalline zinc oxide—Part II: Abnormal grain growth, texture and grain anisotropy," *J. Eur. Ceram. Soc.* 36.5 (2016): 1221-1232.
- [108] P. Jood *et al.*, "Al-Doped Zinc Oxide Nanocomposites with Enhanced Thermoelectric Properties," *Nano Lett.*, vol. 11, no. 10, pp. 4337–4342, Oct. 2011.
- [109] N. Ma, J.-F. Li, B. P. Zhang, Y. H. Lin, L. R. Ren, and G. F. Chen, "Microstructure and thermoelectric properties of Zn_{1-x}Al_xO ceramics fabricated by spark plasma sintering," *J. Phys. Chem. Solids*, vol. 71, no. 9, pp. 1344–1349, Sep. 2010.
- [110] L. Han *et al.*, "The influence of α - and γ -Al₂O₃ phases on the thermoelectric properties of Al-doped ZnO," *J. Alloys Compd.*, vol. 555, pp. 291–296, Apr. 2013.
- [111] T. Tsubota, M. Ohtaki, K. Eguchi, and H. Arai, "Thermoelectric properties of Al-doped ZnO as a promising oxidematerial for high-temperature thermoelectric conversion," *J. Mater. Chem.*, vol. 7, no. 1, pp. 85–90, Jan. 1997.
- [112] M. Ohtaki, S. Maehara, and S. Shige, "Thermoelectric properties of Al-doped ZnO sintered with nanosized void forming agents," in *Thermoelectrics, 2003 Twenty-Second International Conference on - ICT*, 2003, pp. 171–174.
- [113] M. Ohtaki, T. Tsubota, and K. Eguchi, "Thermoelectric properties of oxide solid solutions based on Al-doped ZnO," in *XVII International Conference on Thermoelectrics, 1998. Proceedings ICT 98*, 1998, pp. 610–613.
- [114] T. Tsubota, M. Ohtaki, K. Eguchi, and H. Arai, "Thermoelectric properties of ZnO doped with the group 13 elements," in *XVI International Conference on Thermoelectrics, 1997. Proceedings ICT '97*, 1997, pp. 240–243.
- [115] T. Tsubota, M. Ohtaki, K. Eguchi, and H. Arai, "Transport properties and thermoelectric performance of (Zn_{1-y}Mg_y)_{1-x}Al_xO," *J Mater Chem*, vol. 8, no. 2, pp. 409–412, 1998.
- [116] Y.-H. Chou, J. L. H. Chau, W. L. Wang, C. S. Chen, S. H. Wang, and C. C. Yang, "Preparation and characterization of solid-state sintered aluminum-doped zinc oxide with different alumina contents," *Bull. Mater. Sci.*, vol. 34, no. 3, pp. 477–482, Sep. 2011.
- [117] J. Han, P. Q. Mantas, and A. M. R. Senos, "Densification and grain growth of Al-doped ZnO," *J. Mater. Res.*, vol. 16, no. 02, pp. 459–468, 2001.
- [118] K. F. Cai, E. Müller, C. Drašar, and A. Mrotzek, "Preparation and thermoelectric properties of Al-doped ZnO ceramics," *Mater. Sci. Eng. B*, vol. 104, no. 1–2, pp. 45–48, Nov. 2003.
- [119] K. J. Chen *et al.*, "The crystallization and physical properties of Al-doped ZnO nanoparticles," *Appl. Surf. Sci.*, vol. 254, no. 18, pp. 5791–5795, Jul. 2008.
- [120] D. G. Cahill *et al.*, "Nanoscale thermal transport," *J. Appl. Phys.*, vol. 93, no. 2, pp. 793–818, Jan. 2003.
- [121] C. Dreßler, R. Löhnert, J. Gonzalez-Julian, O. Guillon, J. Töpfer, and S. Teichert, "Effect of Carbon Nanotubes on Thermoelectric Properties in Zn_{0.98}Al_{0.02}O," *J. Electron. Mater.*, pp. 1–5, Oct. 2015.

- [122] Y. Kinemuchi, H. Nakano, M. Mikami, K. Kobayashi, K. Watari, and Y. Hotta, "Enhanced boundary-scattering of electrons and phonons in nanograined zinc oxide," *J. Appl. Phys.*, vol. 108, no. 5, p. 053721, Sep. 2010.
- [123] Y. Zhou, I. Matsubara, W. Shin, N. Izu, and N. Murayama, "Effect of grain size on electric resistivity and thermopower of $(\text{Ca}_{2.6}\text{Bi}_{0.4})\text{Co}_4\text{O}_9$ thin films," *J. Appl. Phys.*, vol. 95, no. 2, pp. 625–628, Jan. 2004.
- [124] D. P. Joshi and K. Sen, "Effect of grain size on the resistivity of polycrystalline material," *Sol. Cells*, vol. 9, no. 4, pp. 261–267, Sep. 1983.
- [125] D. Chaverri, A. Saenz, and V. Castano, "Grain size and electrical resistivity measurements on aluminum polycrystalline thin films," *Mater. Lett.*, vol. 12, no. 5, pp. 344–348, Dec. 1991.
- [126] K. Watari, K. Hirao, M. Toriyama, and K. Ishizaki, "Effect of Grain Size on the Thermal Conductivity of Si_3N_4 ," *J. Am. Ceram. Soc.*, vol. 82, no. 3, pp. 777–779, Mar. 1999.
- [127] J. A. Wollmershauser *et al.*, "An extended hardness limit in bulk nanoceramics," *Acta Mater.*, vol. 69, pp. 9–16, May 2014.

CHAPTER 3 - CONTINUOUS FUNCTIONALLY GRADED MATERIAL TO IMPROVE THE THERMOELECTRIC PROPERTIES USING ZNO

This chapter describes the methods employed to process a continuous functionally graded microstructure. A continuous grain size gradation is achieved in ZnO using a water sintering strategy via SPS in combination with modified tooling and strategic mechanical load schedules. The grain size gradation of a 10-mm thick, fully dense ZnO sample goes from submicron-sized grains of around 180 nm down to micron-sized grains of about 1.2 micrometers. This is the largest known microstructural gradation done in one step. Predictions of the grain size with a Master Sintering Curve (MSC) approach are done with a series of isothermal experiments on two different mechanical load schedules. A slight overestimate of the grain size is seen from the predictions of samples sintered isothermally to a sample sintered in a thermal gradient due to a stress shielding effect. The mechanical properties of the FGM were tested with an axial traverse in Vickers micro hardness showing a gradient from 2.6 GPa to 4.2 GPa. In addition, the thermoelectric properties of the FGM were measured. The results show an enhancement of the zT at lower temperature by an order of magnitude compared to the baseline samples with uniform grain sizes providing a new path for bandwidth improvements of bulk thermoelectric material.

3.1 INTRODUCTION

Transient heat sources are seeking thermoelectric generators (TEGs) with better thermal stress mitigation and wider temperature bandwidth to capture more waste heat in a larger temperature range [1]. TEGs with segmentation improvements [2] as well as well as homogenous property manipulation [3] have shown to improve efficiency in bulk

material. FGM is one way to improve the efficiency and useful temperature range of thermoelectrics [1]. TEGs based on carrier concentration manipulation have improved the efficiency by 8-12 % [4], [5]. FGM thermoelectrics in terms of segmentation, carrier concentration, and microstructure was achieved in some work [1].

Grain size has a large effect on the thermoelectric properties [6], [7]. A study on small, large, and randomly mixed grain size thermoelectric samples showed that small grains had the best performance [8]. Spark plasma sintering (SPS) techniques have already been explored to fabricate FGMs with modified tooling [9]. A conical die arrangement was used to densify different phases of material at different spots in the die axially using a thermal gradient during sintering [10]. One group created an axial microstructural gradient from fully dense to open porosity in a single step by using an offset die arrangement [11]. The concept of an offset die is used in another study to stabilize phases creating the first grain size gradient in an axial sample [12]. Tailored microstructure in FGM TEGs was achieved for the first time using SPS process with a conical die [13]. A layered powder system of $Pb_{1-x}Sn_xTe$ with different dopant concentrations was fabricated using a free sintering method. However, the study was lack of a comparison to samples with homogenous grain size [14].

Zinc oxide (ZnO) is a good candidate for microelectronic and high temperature thermoelectric devices due to enhanced electrical conductivity in pure nanocrystalline ZnO caused by interstitial Zn and oxygen vacancies as well as high Seebeck coefficient at elevated temperatures [15]. It is a good model material to use for thermoelectrics because it is abundant, safe, cost efficient, and relatively easy to process. Some SPS work on ZnO showed that with sintering aids the temperature at which it sinters can be reduced to

400°C [16], [17]. It was later shown that the compaction using acetate phase is necessary to achieve sintering at this low of temperature [18]. Also SPS studies have also shown that the heating rate significantly lowers the sintering temperature of ZnO [19], [20]. The largest improvement in sintering ZnO was done by adding 1.5 monolayers of deionized water on the surface of the ZnO by injection into the compacted green body. The water is thought to help the densification in four major ways. First, there is improved initial packing density due to less friction between particles. Second is a purposed hydroxide ion mass transport. Third is a liquid phase surface transport of the Zn and O ions. Fourth is a surface cleaning that consumes the carbonate that would inhibit mass transport [21], [22].

The current work aims to improve TE material by using a microstructural transition in terms of grain size using ZnO as a model material. A continuous grain size gradient is processed in one step. Rather than making a graded composition or phase, a continuous gradation of grain size is achieved in a 10-mm thick ZnO sample using a water sintering strategy via spark plasma sintering (SPS) with a thermal gradient, in combination with modified tooling and strategic mechanical load schedules. In order to capture a large range of microstructure, optimized sintering at lower temperatures is used [22]. The higher temperature sintering contributes to grain growth of fully dense material. With a Master Sinter Curve (MSC) approach [23], the effects of various heating rates and temperatures on the sintering of ZnO can be used to help predict the microstructure with a series of isothermal experiments. The microstructural gradient is a brand-new method for improving the figure of merit range for a thermoelectric material (zT). The zT for many ZnO systems including doped polycrystalline ZnO has been in the range of 10^{-5} to 10^{-2} in the temperature range of 100°C to 400°C, which already makes our pure ZnO competitive with

what is currently used [15], [24], [25]. In terms of FGM TEGs, this is the first ceramic and semiconductor material to be fabricated with grain size gradation of an order of magnitude in a continuous sample made in one step. Sintering FGM ZnO in terms of grain size allows for better controllability of properties and tunability for higher efficiency thermoelectrics, varistors, and piezoelectrics.

3.2 PROCEDURE

Commercially available ZnO nanopowder (US Research Nanomaterials, Inc.) with high purity of 99.95 % and average particle size of 18 nm was used in these studies. Transmission Electron Microscope (TEM), Scanning Electron Microscope (SEM), and X-ray diffraction (XRD) are performed on the ZnO powder.

To achieve different heating schedules spatially in one sintering setup, a novel sintering setup is made to achieve a large temperature difference across a sintering green body. In this approach, one plunger has less contacting area with the die and thus has higher current density as shown in Figure 3.1. This creates a local hot spot on that side and a temperature field or thermal gradient (TG) across the sintering specimen. For samples sintered in a TG, the material near the hot side will densify more quickly and start grain growth while the material on the other side will densify more slowly due to lower temperature. This differential sintering across the sample results in a continuously graded microstructure in terms of grain size.

Prior to sintering, the powder is stored in a desiccator. Eighteen grams of ZnO is used to get a fully dense material that is 10-mm thick. The powder is pressed once to consolidate a green part, 2 wt.% water is injected into the green part with a micropipette allowing for capillary action to wet the lightly compacted green part. The plunger faces are

sprayed with BN, and the powder is pressed again to the initial sintering load. For samples sintered in a TG, the setup used is shown in Figure 3.1. There is an alumina sleeve to aid in mechanical support and insulation of the hot side graphite punch. BN spray is used around the hot side punch for more insulation. An external graphite sleeve is used for more support and a heat sink. BN is also sprayed on the plunger faces to achieve higher thermal gradient and negate the effects of electric field. These modifications are necessary to get the maximum temperature gradient across the sintering sample. The TG sintering setup is controlled from the hot side plunger and the cold side temperature is monitored to investigate the total temperature gradient and heating rates within the TG system.

For predictions of the grain size that can be achieved in a sample sintered in a thermal gradient, a typical SPS graphite die setup is used. Samples are sintering isothermally to predict the density and grain size evolution over time using an MSC approach. Three different heating schedules (175°C/min to 900°C, 125°C/min to 700°C, and 75°C/min to 500°C) were used representing the hot side, cold side, and the geometric middle, respectively. The densification curves were plotted to show the predictive behavior that should occur in a TG sintering setup. The grain sizes are monitored for the three heating schedules at cut off times corresponding to 97% dense, half the holding time, and the full holding time. This gives a density-grain size-time (DGT) plot of conditions that can predict the final microstructure of system with differential heating schedules. The load schedule started with a low value (35 MPa) during the low temperature bake out, and it was increased to 73 MPa before the large water outgassing. The load is controlled at 0.1 kN per second. A novel sintering setup was developed for the TG to include the wide range of heating schedules in one die setup.

The sintering setup of samples processed with a TG is modeled in COMSOL to help predict the temperature difference across the sintering specimen. This provides temperature field data of the hot spots in the plungers and uniformity of the isotherms across the sintering specimen. The pulsed DC current and temperature distributions used in COMSOL are governed by the system of simultaneous partial differential equations (PDEs) below:

$$\nabla \cdot J = 0 \quad (3.1)$$

$$\rho c_p \frac{\partial T}{\partial t} - \nabla \cdot (k \nabla T) = q_i \quad (3.2)$$

where $J = \sigma E$ is the current density with E as the electric field, σ is the electrical conductivity. $(-k \nabla T)$ is the heat flux density, T is the temperature, k is the thermal conductivity, ρ is the density, c_p is the heat capacity, and $q_i = JE$ is the heat generated by the flowing current per unit volume per unit time.

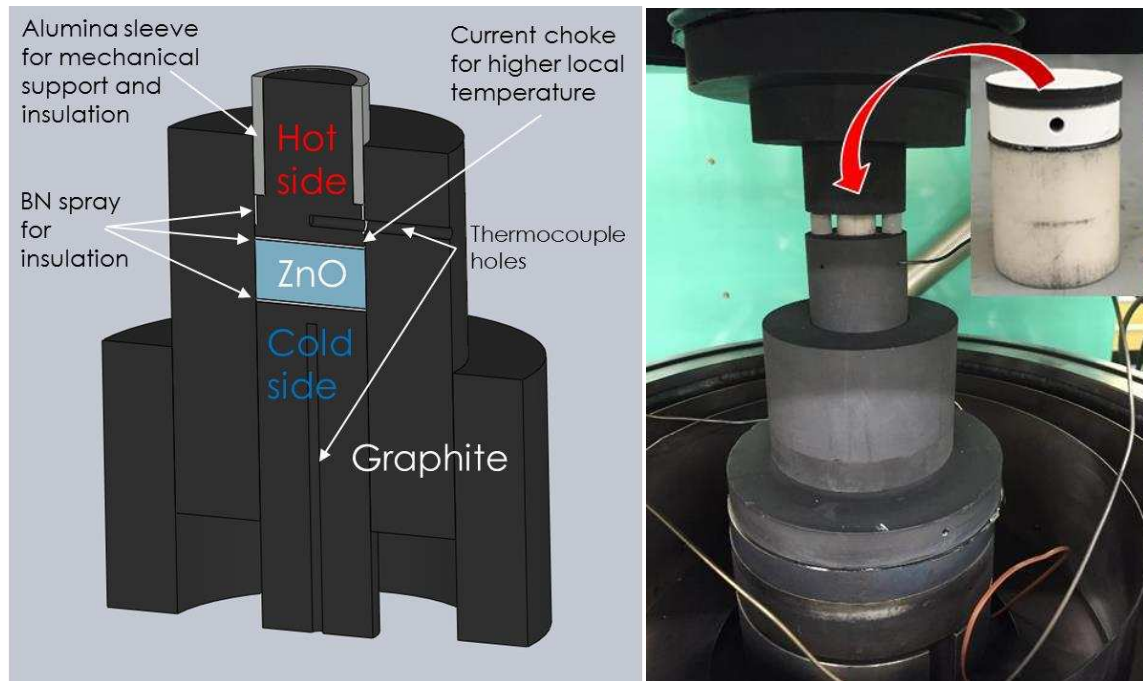


Figure 3.1: 3-D representation of the whole sintering setup (left) and fully machined sintering setup used in sintering of specimens in a thermal gradient (right).

SEM images were analyzed to estimate the grains sizes of the samples sintered with a TG, compared to that of the samples sintered isothermally for predictions of the grain size or porosity. Image analysis using polished surfaces and the intercept procedure (ASTM E112, [26]) with a correction factor of 1.56 was performed to determine the grain size, and histograms are made for samples processed with a TG and the samples processed isothermally. Densities were first measured geometrically, verified with the Archimedes Principle method, and checked with areal density. Vickers Micro hardness is done on a fully dense FGM sample at a load of 9.8 kgf and dwell time of fifteen seconds taking six indentations at every location tested. Thermoelectric properties including Seebeck coefficient, electrical resistivity, and thermal conductivity were measured as a function of temperature up to 400°C on the fully dense FGM and compared to baseline samples of small grains and large grains. The Seebeck coefficient and resistivity were measured with

the Kohlrausch method where sections are 2 x 2 x 10 mm sections [27], [28], and the thermal conductivity is measured using a modified transient plane method with geometry of the final sintered specimens [29]–[31]. All sample properties were measured after calcining to ensure defect equilibrium is achieved.

3.3 RESULTS AND DISCUSSION

The particle size is verified with SEM and XRD using the Williamson-Hall method [32]. The powder shows that there are very small particles with a small deviation from the average, and there are different shaped particles such as longer particles, spheres, and sharper edged particles. Also, the powder is loosely agglomerated making it ideal for sintering as shown in Figure 3.2.

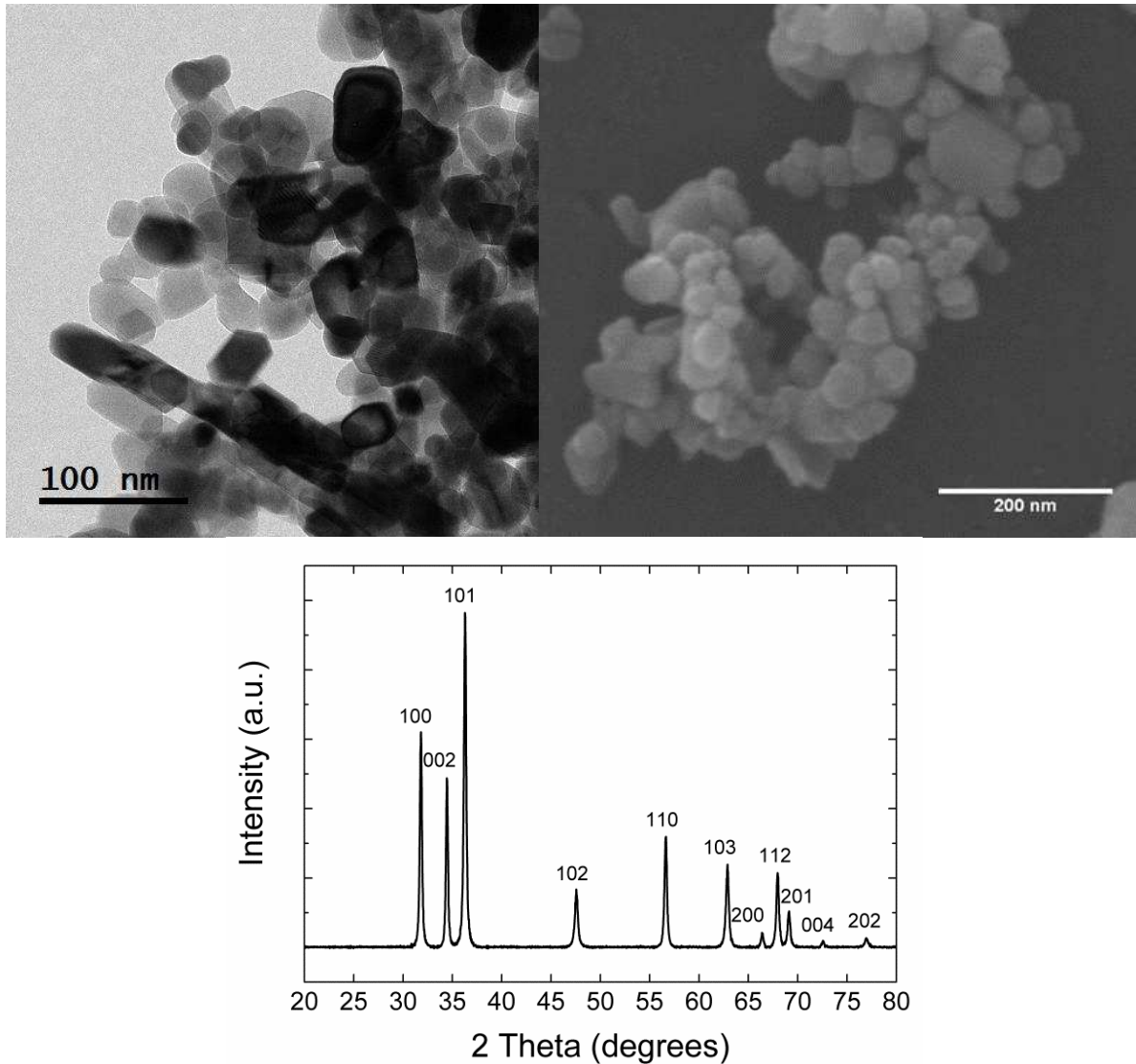


Figure 3.2: ZnO powder from US Research Nanomaterials, Inc. (US Nano). TEM image (top left). SEM image (top right) and XRD pattern (bottom).

A. ISOTHERMAL SINTERING FOR PREDICTIONS OF MICROSTRUCTURE

Isothermal sintering is done for three heating schedules, 175°C/min to 900°C, 125°C/min to 700°C, and 75°C/min to 500°C, and a mechanical load starting at 35 MPa increasing to 75 MPa after water outgassing to obtain the DGT predictive model for a fully dense FGM ZnO. This DGT predicts a fully dense system where the grain size is about 1.8 micrometers on one side and 0.3 micrometers on the other as shown in Figure 3.3. The DGT

plot shows the grain size and reports the standard deviation showing that there is a large distribution in grains. The standard deviation and thus grain size distribution gets larger with larger grains. Heating rate and temperature are dependent on the current through the graphite. Since ZnO is somewhat conductive, current can also go through the compacted powder. The higher heating rates and higher temperature correspond to higher current. This could influence the sintering.

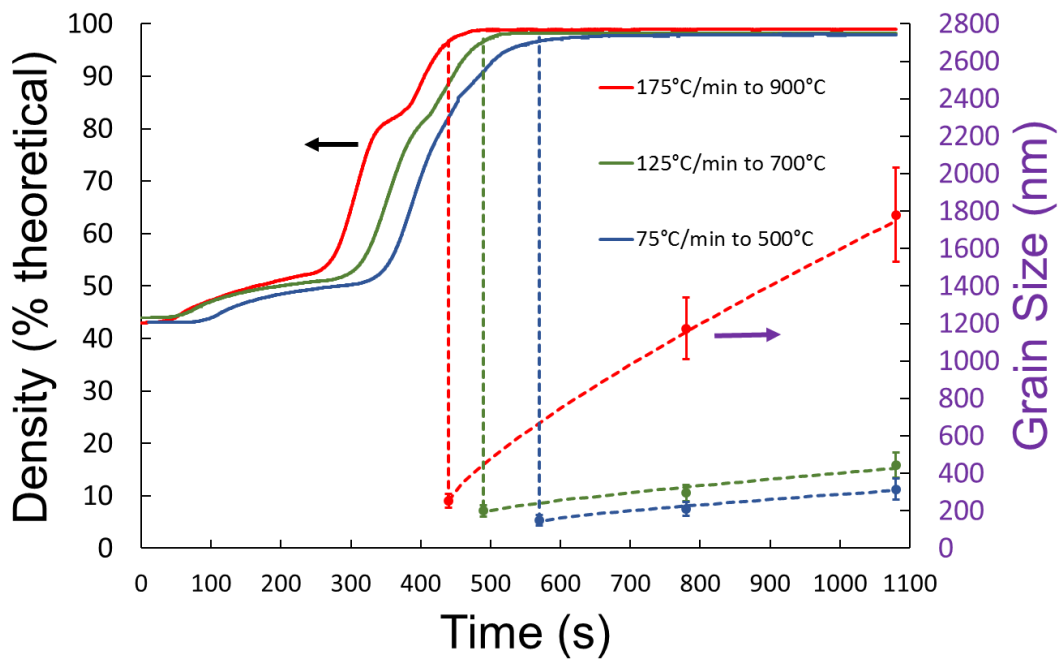


Figure 3.3: DGT plot for prediction of grain size and porosity in a sample sintered with a TG when load is ramped to 73 MPa after large water outgassing.

A second DGT is done with a different load schedule: load starts at 73 MPa and is decreased to 35 MPa before the water outgassing. This DGT is done to investigate the pressure effects on the ZnO system. In this DGT, the prediction of the microstructure is a fully dense side with some noticeable grain growth to a continuously smaller grain size portion that eventually becomes porous as indicated in Figure 3.4. It is clearly seen the

pressure affects this system significantly. Fully dense samples will need sufficient mechanical load.

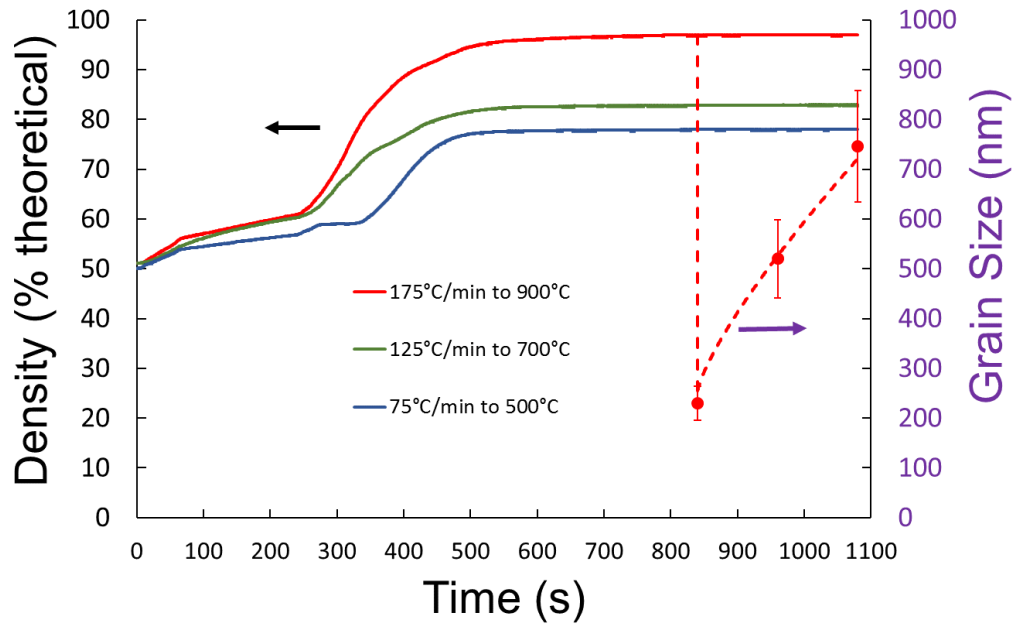


Figure 3.4: DGT plot for prediction of grain size and porosity in a sample sintered with a TG when the load is decreased to 35 MPa before the large water outgassing.

B. COMSOL MODELING

The model of the graphite setup for sintering with thermal gradients is shown in Figure 3.5. It verifies the temperature range that can be achieved. There is a hot spot in the plunger that has less contact area. The hot side thermocouple is inserted radially to avoid interference from the SPS current. Controlling with the hot side thermocouple allows for less overshoot of the hot side temperature. A large temperature field of about 400°C can be created for the ZnO TG sintering as shown in Figure 3.5, and the isotherms across the sintering sample are mostly flat indicating that there should be less variation in microstructural evolution in the radial direction.

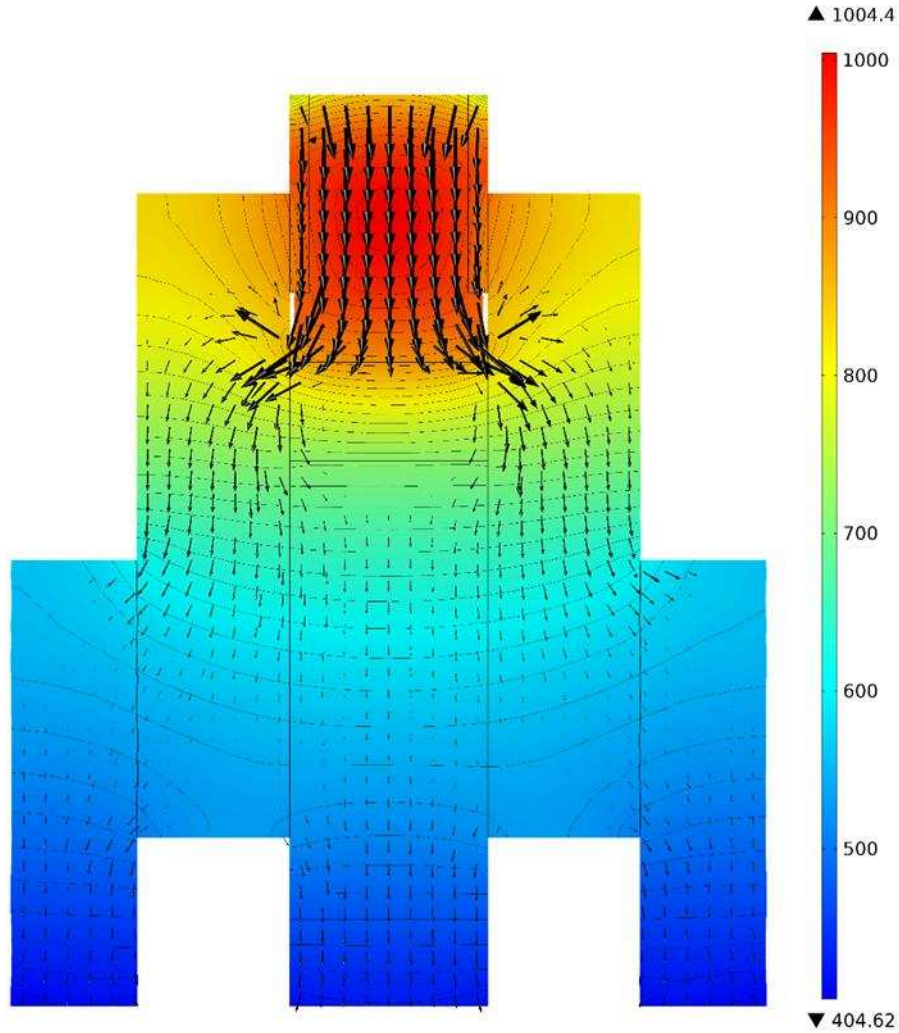


Figure 3.5: COMSOL Model of TG sintering setup for temperature field for ZnO.

C. THERMAL GRADIENT SINTERING

The temperature and vacuum schedules for the samples sintered in a TG are shown in Figure 3.6. The temperature schedule of the hot side control point (175°C/min to 900°C) and the cold side (75°C/min to 500°C) in the sample sintered in a TG are measured showing strong correlation to the DGT heating schedules for the 175°C/min to 900°C and 75°C/min to 500°C. The sintering parameters accommodate TG sintering. It took some iterations to achieve replication of the heating schedule between the samples sintered

isothermally for the DGT predictions and the samples sintered with an induced TG. The largest challenge with processing is the mechanical load schedule because it was strategically increased or decreased because of outgassing water, which is not common SPS practice. The temperature of the geometric middle in a sample sintered in a TG is assumed to be an average of the hot and cold side temperatures at 125°C/min to 700°C. Nevertheless, the heating rates and hold temperatures in Figure 3.6 are spatially recreated in one sintering arrangement using the modified tooling setup from Figure 3.1. Although the sintering conditions in the TG were setup to mimic the same conditions as the DGT in one setup, the current that goes through the FGM sample is yet different from that goes through the samples sintered isothermally.

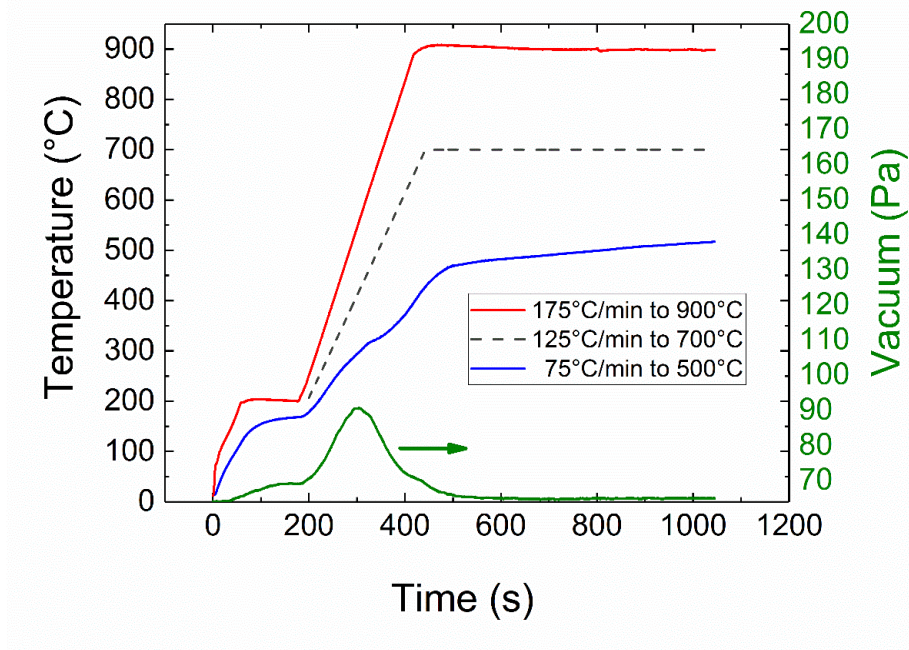


Figure 3.6: Temperature data collected from a sample sintered in a TG when load is ramped to 73 MPa after the large water outgassing.

The two samples that were sintered with a TG are compared below in Table 3.1. It shows that decreasing the load before outgassing results in a sample that does not reach

full density. Mechanical load has a profound effect on the system, and a sufficient amount is needed to close pores and keep densification as the favorable mechanism in a wide range of sintering temperatures. The sample sintered in a TG where load is applied after the large water outgassing reaches full density. The mechanical load is ramped during stage two sintering revealing that sufficient mechanical load is needed during stage two sintering.

Table 3.1: Comparison of samples sintered in a Showing the load schedule and density.

Condition	Load during bake out (MPa)	Load after large water outgassing (MPa)	Total theoretical density of TG sample (%)
1	35	73	98
2	73	35	86

A macro- and microscopic view of the sample sintered in a TG that was sintered to full density can be seen in Figure 3.7. The yellowish/white color indicates correct stoichiometry in ZnO. Also, it is important to note that there was no notable grain size gradient radially. Some samples sintered at lower temperature to retain submicron grain sizes exhibited a blue color after SPS processing. This color is due to a defect in the ZnO as Zinc hydroxide. Samples processed at high temperatures do not exhibit the blue region as the hydroxide ion is relieved at high temperatures. The hydroxide is effectively removed by annealing. Thus, all the samples were annealed after SPS in the current work. It should also be noted that annealing was done at a temperature low enough to restrict grain growth in the ZnO.

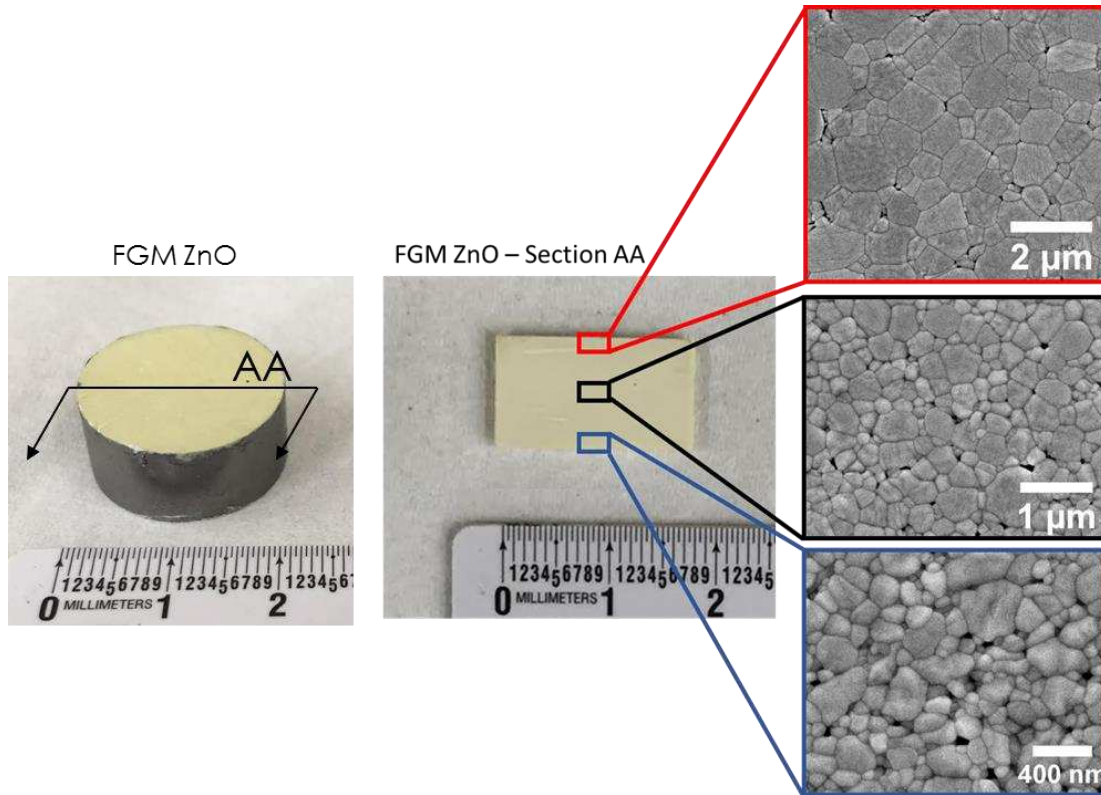


Figure 3.7: Macroscopic cross section and microscopic images of ZnO that is fully dense with a graded grain size distribution.

A plot of grain size versus distance from the hot side plunger of the fully dense sample that was sintered in a TG is shown in Figure 3.8. The axial grain size distribution follows a decaying exponential because each (mm) increment is representative of a different temperature. Temperature is known to affect the grain growth exponentially [33]–[35]. The achieved grain size gradation is close to an order of magnitude, which should have an influence on the electrical, thermal, and mechanical properties along the axial direction of the sample sintered in a TG [36]. Others have achieved small changes in microstructure targeting different phases [10] [11] [12]. This is the first semiconductor or ceramic to be graded to this extent with microstructure.

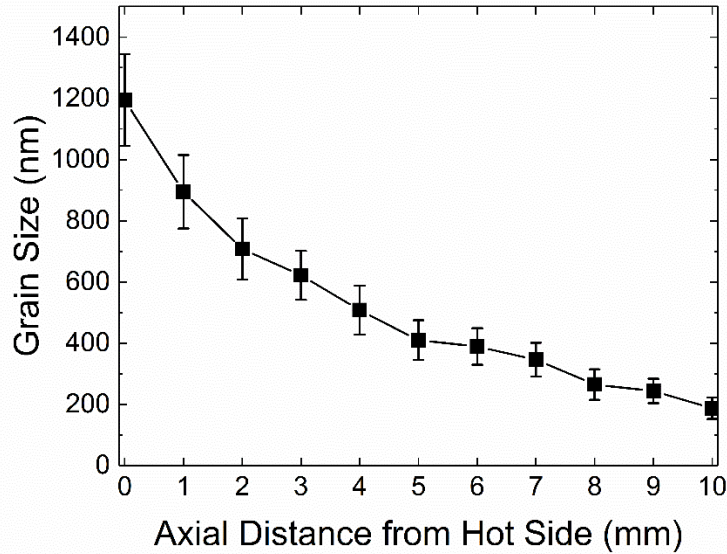


Figure 3.8: Grain size gradation of fully dense sample sintered in a TG.

D. MICROSTRUCTURE OF SAMPLES SINTERED ISOTHERMALLY FOR PREDICTIONS VS. A SAMPLE SINTERED IN A THERMAL GRADIENT

The microstructure of locations in the thermal gradient are compared to samples that have the same temperature and pressure schedules but are done isothermally to predict the grain size gradation that should occur in a sample sintered with a TG. For the first load schedule, the comparison (Table 3.2) shows that the prediction of grain size from the samples run isothermally are different from the that of the sample sintered with a TG. The final grain sizes in the samples run isothermally for predictions are larger than those at the corresponding location in the sample sintered with a TG at each condition yielding evidence of a system with stress shielding in the thermal gradient sintering system.

Table 3.2: Comparison of final grain size for a sample sintered with a TG versus samples sintered isothermally for predictions done when load is ramped to 73 MPa after the large water outgassing.

Isothermal Sintering (DGT)		Thermal Gradient Sintering (FGM)	
Condition	Final Grain Size (nm)	Condition	Final Grain Size (nm)
175°C/min to 900°C	1781 ± 617	175°C/min to 900°C	1194 ± 430
125°C/min to 700°C	436 ± 125	125°C/min to 700°C	389 ± 133
75°C/min to 500°C	316 ± 96	75°C/min to 500°C	187 ± 98

A look at the grain size and distribution of the sample sintered in a TG versus the samples sintered isothermally for predictions can be seen in Figure 3.9. and All samples show a large distribution of grain sizes. A clear difference in the average grain size between the samples sintered in a TG versus samples sintered isothermally is shown due to the varied strain rates across the sample when it is sintered in a TG. The time variant strain rates shield the material at the bottom from the same stress, as the material at the bottom will not shrink at the same rate and oppose the sintering shrinkage of the material above it. The morphology and pore locations show little differences in the sintering process as shown from the SEM images in Figure 3.9.

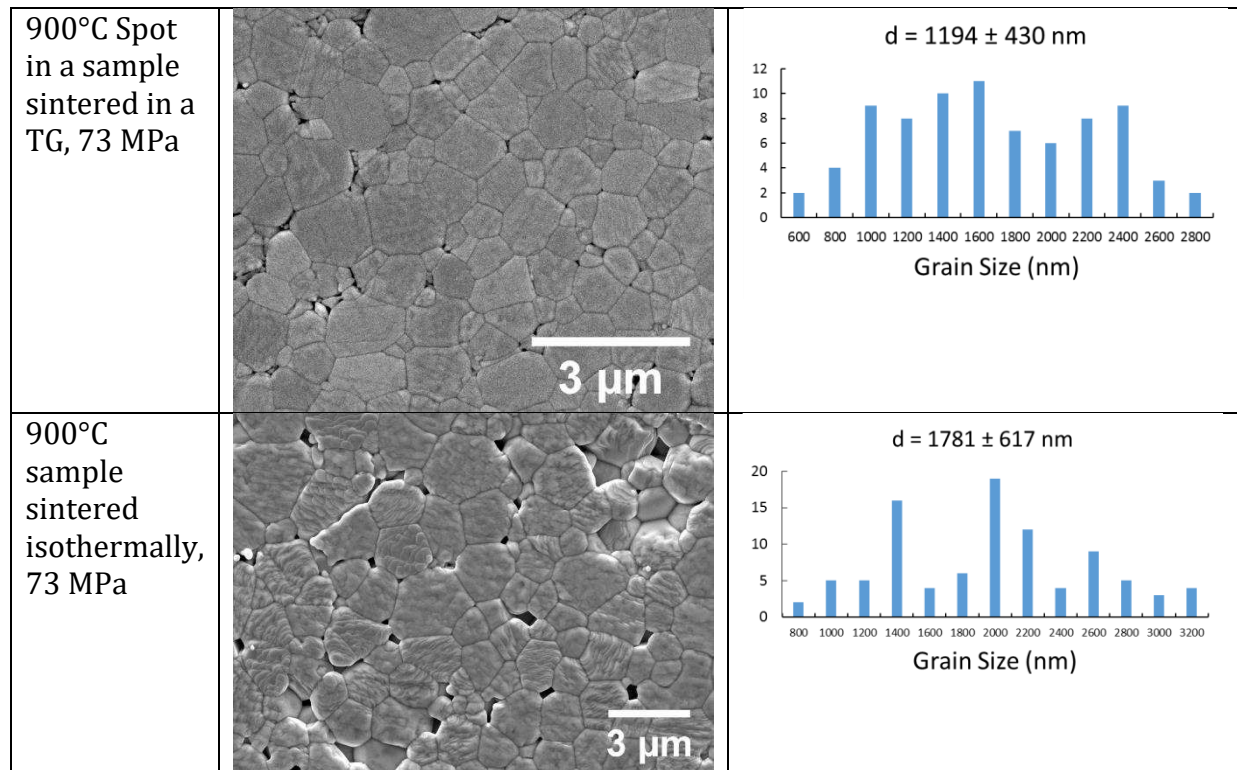


Figure 3.9: Microstructural comparisons for a sample sintered in a TG versus a sample sintered isothermally when load is ramped to 73 MPa after the large water outgassing.

The DGT where mechanical load is decreased during water outgassing yields a microstructure prediction that is not fully dense, and the sample sintered in a TG is made to compare to the isothermally sintered samples. The results of the isothermally sintered predictions and the sample sintered in a TG are present in Figure 3.10 and Table 3.3. The sample sintered in a TG follows the same trend as the DGT but again the grain size or porosity, in this case, is lower in the sample sintered in a TG compared to samples sintered isothermally. This observation further supports the presence of a stress shielding effect and suggested that the same stress phenomenon arises in another load schedule.

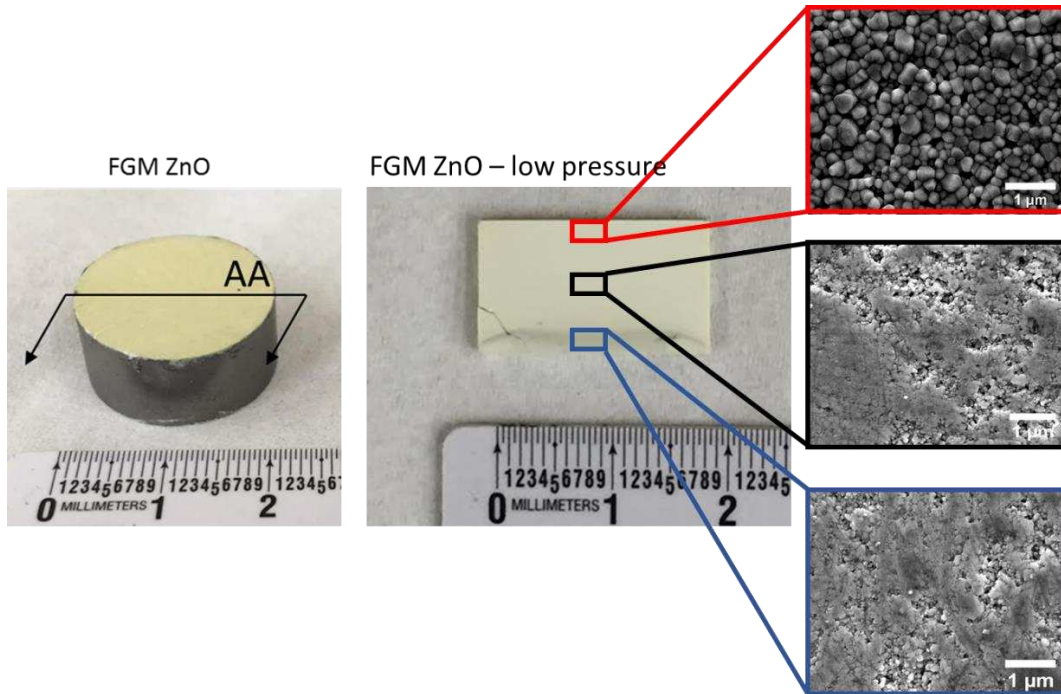


Figure 3.10: Macro- and microstructural image of the sample sintered in a TG done when the load is decreased to 35 MPa before the large water outgassing.

Table 3.3: Comparison of final grain size or density for samples sintered with a TG versus samples sintered isothermally for predictions done when load is released to 35 MPa before the large water outgassing.

Isothermal Sintering (DGT)		Thermal Gradient Sintering (FGM)	
Condition	Final Microstructure	Condition	Final Microstructure
175°C/min to 900°C	750 ± 273 nm, 98 ± 1%	175°C/min to 900°C	397 ± 146 nm, 98 ± 1%
125°C/min to 700°C	83 ± 2%	125°C/min to 700°C	80 ± 2%
75°C/min to 500°C	78 ± 2%	75°C/min to 500°C	76 ± 2%

The stress shielding is from time variant sintering where there is a large axial temperature field causing differential strain rates or differential shrinkage as seen in Figure 3.3 and Figure 3.4. The higher temperature sinters more quickly having closed porosity sooner than the underlying material at less temperature. This causes the stress states to change continuously along the specimen sintering in a TG. The effects of different stress states on ceramic sintering is explored in Bordia and Raj [37]. The stress states have

been known to affect the densification of a porous body by affecting the diffusion paths [38]. In our case, the stress states at the colder side most likely retard diffusion mechanisms yielding a less developed microstructure than the samples sintered isothermally for predictions which have the same stress state throughout the sample. Initial evidence of this hindrance is the smaller grain sizes in the sample sintered in a TG compared to the samples were sintered isothermally to predict the grains size at three different spots. The amount of pressure to overcome this could be calculated, and it is estimated from our work and one previous study to be between 19 MPa and 30 MPa [22].

E. MICRO HARDNESS DATA ON FULLY DENSE FGM ZNO

Typical values for the hardness of ZnO are in the range of 1-2.5 GPa for grain sizes varying from 2-5 micrometers [39]. The lower value of that hardness range lines up with our hot side of the sample which has grain size of about 1.2 micrometers and hardness of about 2.6 GPa as shown in Figure 3.11. The side with smaller grains has improved hardness. The decrease in grain size shows an increase in hardness showing a Hall-Petch-like relationship [40]–[42]. This relationship arose from the smaller grains and less cracks of critical length. This fabrication method provides a designable grain size FGM other than thermoelectrics that could be used for thermal stress mitigation purposes, cutting tools, and piezoelectrics.

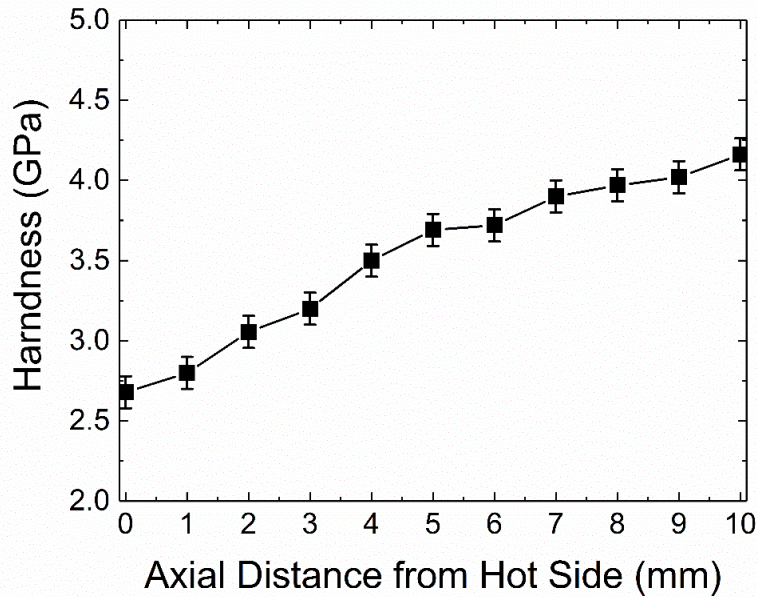


Figure 3.11: Vickers Micro Hardness axial traverse down the fully dense FGM ZnO.

F.TEG PROPERTIES ON FULLY DENSE FGM ZNO

Baseline samples with uniform grain sizes to be made and compared to the samples sintered in a TG for three conditions: the hot side, geometric middle, and the cold side. The small-grained baseline sample has grain size of $200 \text{ nm} \pm 30 \text{ nm}$ and is associated with the cold side processing, and the large grained baseline sample has grain size of $1250 \text{ nm} \pm 240 \text{ nm}$ and is associated with the hot side processing. The FGM Thermoelectric (TE) ZnO material is tested with heat flow in both directions showing no differences in properties except the thermal conductivity. Thermal conductivity of the FGM is higher when the heat flux is exposed to the large-grained side as opposed to the small-grained side.

It is evident that this microstructural gradation affects the FGM Seebeck coefficient. At lower temperatures, the Seebeck coefficient is closer to the small-grained sample values. At higher temperatures, the Seebeck coefficient is closer to the large-grained sample value. The grain size effects are more dominant at lower temperatures as evident in the resistivity

convergence at the higher temperatures where temperature effects dominate. Also, the resistivity is dependent on length, so it can be shown that the resistivity of the FGM is closer to the large-grain sample's resistivity value. The FGM TE ZnO material's resistivity and thermal conductivity behave more like the large-grained sample at all temperatures. The small-grained sample has the highest zT at a temperature of 400°C. The large-grained sample has a similar trend in zT as the small-grained sample but is less in magnitude. The trends in thermoelectric properties of the small-grained and large-grained samples are in accord with many studies done on grain size effects [6], [8], [43]. The FGM TE ZnO material has an order of magnitude higher zT at lower temperature compared to the small- and large-grained samples, and the FGM has lower zT at higher temperature.

The tail-end of the zT is improved in our system. The Seebeck coefficient transitions from a value near the small-grained sample value at lower temperature to a value closer to the large-grained at higher temperature. This is evidence of an enhanced system and a compensation of the thermoelectric voltage. The resistivity of the FGM is lower than the large-grained sample, so it should have Seebeck that is less than that of the large-grained sample [44]. Because the Seebeck coefficient of the FGM has not depleted is more evidence of a Seebeck coefficient enhancement along the sample. The enhancement of the zT temperature range is similar to the one proposed in Jin et al. where the properties are optimized for given locations in the material based on the temperature to maximize the current density [45]. It has also been shown that there is an averaging effect with the Seebeck of segmented TEGs, and this Seebeck coefficient enhancement renders an apparent Seebeck coefficient in the FGM [46]. This is because the voltage drops along the length of the material add together as in voltage sources in series. It is also confirmed that the

resistivity can be less in magnitude in an FGM compared to uniform samples [47]. Another reason for enhanced resistivity in the FGM can be attributed to contact resistance and adherence. Since the samples are calcined after SPS, there should be no defect effects on the electrical properties. The enhancements do not seem to resemble a dopant FGM system [1]. The enhancements are also very similar to segmented systems[48]–[51].

The FGM ZnO improves the zT by an order of magnitude at the lower temperatures tested. We have successfully made a path for improving thermoelectric temperature range with ZnO as a candidate material and a model process using the grain size as the variable. This method is not optimized but shows that this is a new method for improving thermoelectrics. Since the effects are prevalent in ZnO, this method should in theory work on any bulk thermoelectric material. Also, our system should provide higher efficiency compared to a segmented TEG because there is no contact resistance between segments as the gradation is continuous, but no direct comparison has been done yet.

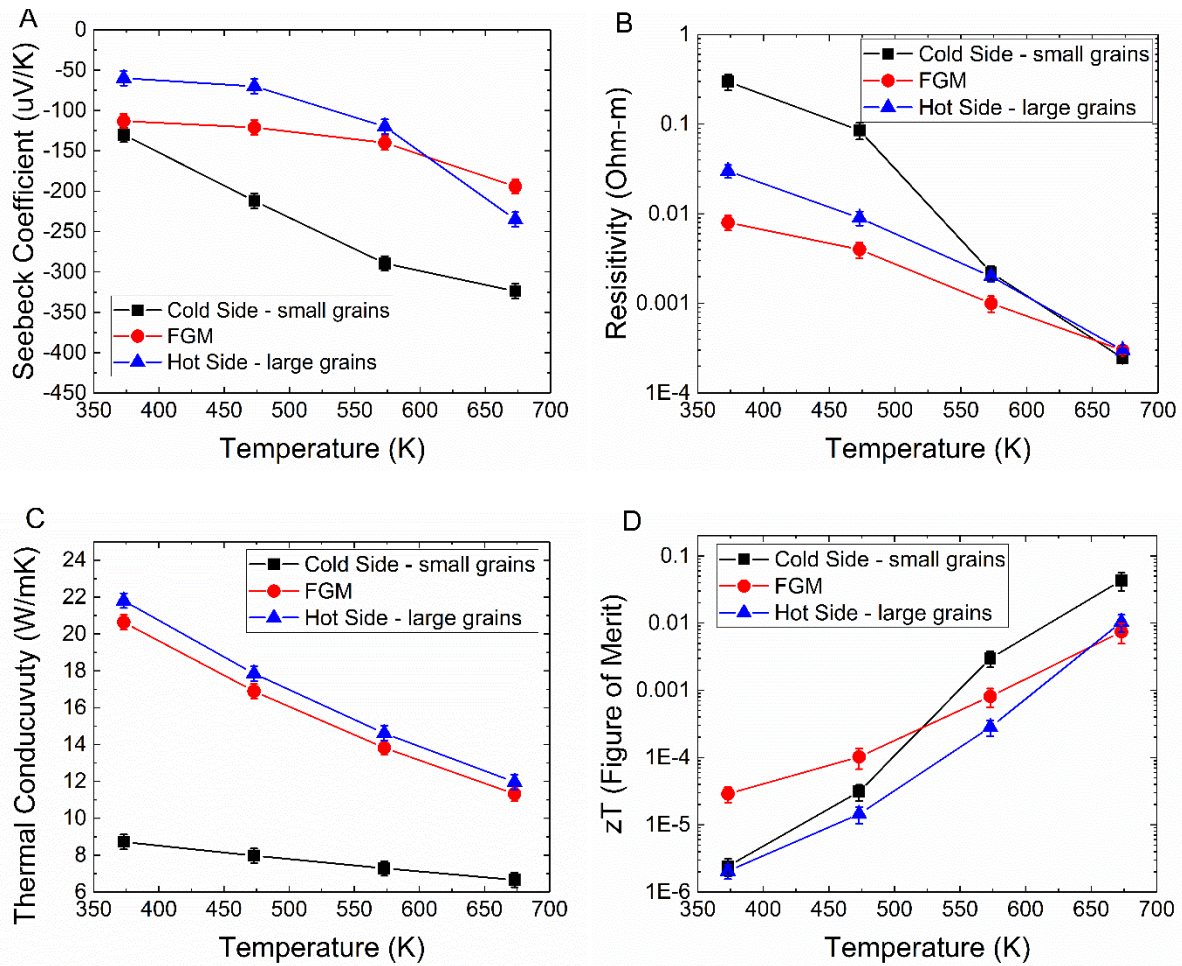


Figure 3.12: Thermoelectric properties of the fully dense material sintered in a TG versus samples sintered isothermally having the size grains as the hot and cold side of the sample sintered in a TG. (a) Seebeck and (b) resistivity, and (c) thermal conductivity are measured, and the zT (d) is calculated.

3.4 CONCLUSION

We fabricate a continuous sample in one step with a grain size gradation of almost an order of magnitude in a 10-mm thick material using modified tooling, transient water assisted sintering, and strategic loads with commercially available material. The maximum temperature on the plunger of 900°C is not enough to reduce the material. The grain size gradation follows an exponential decay along the axial direction. A stress shielding effect occurs in the sample that was sintered with a TG. The loss of uniform stress in a sample

sintered in a TG inhibits the final grain growth, which was predicted in the DGT model with samples sintered isothermally. It is apparent that load plays a significant role in the FGM ZnO system for a wide range of sintering temperatures to reach full density. This is proved with DGTs for two different applied mechanical loads. The mechanical properties show a gradation along the sample that could benefit many micromechanical systems. Lastly, the thermoelectric properties show an enhanced zT temperature bandwidth with an order of magnitude improvement at lower temperature by mechanisms of property gradient. This is a new method for improving bulk thermoelectric material and can be applied to many other materials.

REFERENCES

- [1] M. Koizumi, "FGM activities in Japan," *Composites Part B: Engineering*, vol. 28, no. 1–2, pp. 1–4, 1997.
- [2] J. Schilz, L. Helmers, W. E. Müller, and M. Niino, "A local selection criterion for the composition of graded thermoelectric generators," *Journal of Applied Physics*, vol. 83, no. 2, pp. 1150–1152, Jan. 1998.
- [3] E. Muller, S. Walczak, W. Seifert, C. Stiewe, and G. Karpinski, "Numerical performance estimation of segmented thermoelectric elements," in *ICT 2005. 24th International Conference on Thermoelectrics, 2005.*, 2005, pp. 364–369.
- [4] A. E. Kaliazin, V. L. Kuznetsov, and D. M. Rowe, "Rigorous calculations related to functionally graded and segmented thermoelements," in *XX International Conference on Thermoelectrics, 2001. Proceedings ICT 2001*, 2001, pp. 286–292.
- [5] Z. Dashevsky, Y. Gelbstein, I. Edry, I. Drabkin, and M. P. Dariel, "Optimization of thermoelectric efficiency in graded materials," in *Thermoelectrics, 2003 Twenty-Second International Conference on - ICT*, 2003, pp. 421–424.
- [6] K. Kishimoto and T. Koyanagi, "Preparation of sintered degenerate n-type PbTe with a small grain size and its thermoelectric properties," *Journal of Applied Physics*, vol. 92, no. 5, pp. 2544–2549, Sep. 2002.
- [7] Y. Gao, Y. He, and L. Zhu, "Impact of grain size on the Seebeck coefficient of bulk polycrystalline thermoelectric materials," *Chin. Sci. Bull.*, vol. 55, no. 1, pp. 16–21, Jan. 2010.
- [8] L.-D. Zhao, B.-P. Zhang, W.-S. Liu, and J.-F. Li, "Effect of mixed grain sizes on thermoelectric performance of Bi₂Te₃ compound," *Journal of Applied Physics*, vol. 105, no. 2, p. 023704, Jan. 2009.
- [9] D. Giuntini, J. Raethel, M. Herrmann, A. Michaelis, and E. A. Olevsky, "Advancement of Tooling for Spark Plasma Sintering," *J. Am. Ceram. Soc.*, vol. 98, no. 11, pp. 3529–3537, Nov. 2015.
- [10] C.-Q. Hong, X.-H. Zhang, W.-J. Li, J.-C. Han, and S.-H. Meng, "A novel functionally graded material in the ZrB₂-SiC and ZrO₂ system by spark plasma sintering," *Materials Science and Engineering: A*, vol. 498, no. 1–2, pp. 437–441, Dec. 2008.
- [11] D. M. Hulbert, D. Jiang, U. Anselmi-Tamburini, C. Unuvar, and A. K. Mukherjee, "Continuous functionally graded boron carbide-aluminum nanocomposites by spark plasma sintering," *Materials Science and Engineering: A*, vol. 493, no. 1–2, pp. 251–255, Oct. 2008.
- [12] M. Belmonte, J. Gonzalez-Julian, P. Miranzo, and M. I. Osendi, "Continuous in situ functionally graded silicon nitride materials," *Acta Materialia*, vol. 57, no. 9, pp. 2607–2612, May 2009.
- [13] L. P. Bulat *et al.*, "On fabrication of functionally graded thermoelectric materials by spark plasma sintering," *Tech. Phys. Lett.*, vol. 40, no. 11, pp. 972–975, Dec. 2014.
- [14] Y. Gelbstein, Z. Dashevsky, and M. P. Dariel, "Powder metallurgical processing of functionally graded p-Pb_{1-x}Sn_xTe materials for thermoelectric applications," *Physica B: Condensed Matter*, vol. 391, no. 2, pp. 256–265, Apr. 2007.
- [15] K. H. Kim, S. H. Shim, K. B. Shim, K. Niihara, and J. Hojo, "Microstructural and Thermoelectric Characteristics of Zinc Oxide-Based Thermoelectric Materials

- Fabricated Using a Spark Plasma Sintering Process,” *Journal of the American Ceramic Society*, vol. 88, no. 3, pp. 628–632, Mar. 2005.
- [16] J. G.-J. Benjamin Dargatz, “Effect of electric field and atmosphere on the processing of nanocrystalline ZnO,” *Proceedings of SPIE - The International Society for Optical Engineering*, vol. 8987, 2014.
- [17] S. Schwarz, A. M. Thron, J. Rufner, K. Benthem, and O. Guillon, “Low Temperature Sintering of Nanocrystalline Zinc Oxide: Effect of Heating Rate Achieved by Field Assisted Sintering/Spark Plasma Sintering,” *Journal of the American Ceramic Society*, vol. 95, no. 8, pp. 2451–2457, Aug. 2012.
- [18] J. G.-J. Benjamin Dargatz, “Improved compaction of ZnO nano-powder triggered by the presence of acetate and its effect on sintering,” *Science and Technology of Advanced Materials*, vol. 16, no. 2, p. 025008, 2015.
- [19] L. Gao, Q. Li, W. Luan, H. Kawaoka, T. Sekino, and K. Niihara, “Preparation and Electric Properties of Dense Nanocrystalline Zinc Oxide Ceramics,” *Journal of the American Ceramic Society*, vol. 85, no. 4, pp. 1016–1018, Apr. 2002.
- [20] J. Wang and L. Gao, “Photoluminescence Properties of Nanocrystalline ZnO Ceramics Prepared by Pressureless Sintering and Spark Plasma Sintering,” *Journal of the American Ceramic Society*, vol. 88, no. 6, pp. 1637–1639, Jun. 2005.
- [21] B. Dargatz, J. Gonzalez-Julian, M. Bram, Y. Shinoda, F. Wakai, and O. Guillon, “FAST/SPS sintering of nanocrystalline zinc oxide—Part II: Abnormal grain growth, texture and grain anisotropy,” *Journal of the European Ceramic Society*. 36.5 (2016): 1221-1232.
- [22] B. Dargatz *et al.*, “FAST/SPS sintering of nanocrystalline zinc oxide—Part I: Enhanced densification and formation of hydrogen-related defects in presence of adsorbed water,” *Journal of the European Ceramic Society* 36.5 (2016): 1207-1220.
- [23] H. Su and D. L. Johnson, “Master Sintering Curve: A Practical Approach to Sintering,” *Journal of the American Ceramic Society*, vol. 79, no. 12, pp. 3211–3217, 1996.
- [24] Y. Kinemuchi, M. Mikami, K. Kobayashi, K. Watari, and Y. Hotta, “Thermoelectric Properties of Nanograined ZnO,” *Journal of Elec Materi*, vol. 39, no. 9, pp. 2059–2063, Dec. 2009.
- [25] S. Walia *et al.*, “Transition metal oxides – Thermoelectric properties,” *Progress in Materials Science*, vol. 58, no. 8, pp. 1443–1489, Oct. 2013.
- [26] R. F. Allen, “Standard Test Methods for Determining Average Grain Size,” *Annual Book of ASTM Standards, Metal-Mechanical Testing; Elevated and Low Temperature Tests; Metallography*, 1999.
- [27] H. G. Jensen, “Kohlrusch Heat Conductivity Apparatus for Intermediate or Advanced Laboratory,” *American Journal of Physics*, vol. 38, no. 7, pp. 870–874, Jul. 1970.
- [28] B. M. Gol’tsman and M. G. Komissarchik, “Measurement of thermal and electrical conductivities of small cross section samples in the 80–400 °K range,” *Journal of Engineering Physics*, vol. 20, no. 3, pp. 385–389, Mar. 1971.
- [29] S. A. Al-Ajlan, “Measurements of thermal properties of insulation materials by using transient plane source technique,” *Applied Thermal Engineering*, vol. 26, no. 17–18, pp. 2184–2191, Dec. 2006.
- [30] C. DIXON, M. R. STRONG, and S. M. ZHANG, “Transient Plane Source technique for measuring thermal properties of silicone materials used in electronic assemblies,”

- The International journal of microcircuits and electronic packaging*, vol. 23, no. 4, pp. 494–500, 2000.
- [31] S. E. Gustafsson, “Transient plane source techniques for thermal conductivity and thermal diffusivity measurements of solid materials,” *Review of Scientific Instruments*, vol. 62, no. 3, pp. 797–804, Mar. 1991.
- [32] G. K. Williamson and W. H. Hall, “X-ray line broadening from filed aluminium and wolfram,” *Acta Metallurgica*, vol. 1, no. 1, pp. 22–31, Jan. 1953.
- [33] D. V. Quach, H. Avila-Paredes, S. Kim, M. Martin, and Z. A. Munir, “Pressure effects and grain growth kinetics in the consolidation of nanostructured fully stabilized zirconia by pulsed electric current sintering,” *Acta Materialia*, vol. 58, no. 15, pp. 5022–5030, 2010.
- [34] R. M. German, “Coarsening in Sintering: Grain Shape Distribution, Grain Size Distribution, and Grain Growth Kinetics in Solid-Pore Systems,” *Critical Reviews in Solid State and Materials Sciences*, vol. 35, no. 4, pp. 263–305, Nov. 2010.
- [35] J. Narayan, “Grain growth model for electric field-assisted processing and flash sintering of materials,” *Scripta Materialia*, vol. 68, no. 10, pp. 785–788, May 2013.
- [36] Y. Zhao, Y. Yan, A. Kumar, H. Wang, W. D. Porter, and S. Priya, “Thermal conductivity of self-assembled nano-structured ZnO bulk ceramics,” *Journal of Applied Physics*, vol. 112, no. 3, p. 034313, Aug. 2012.
- [37] R. K. Bordia and R. Raj, “Sintering Behavior of Ceramic Films Constrained by a Rigid Substrate,” *Journal of the American Ceramic Society*, vol. 68, no. 6, pp. 287–292, Jun. 1985.
- [38] R. K. Bordia and G. W. Scherer, “On constrained sintering—I. Constitutive model for a sintering body,” *Acta metallurgica*, vol. 36, no. 9, pp. 2393–2397, 1988.
- [39] T. K. Roy, “Assessing hardness and fracture toughness in sintered zinc oxide ceramics through indentation technique,” *Materials Science and Engineering: A*, vol. 640, pp. 267–274, Jul. 2015.
- [40] R. W. Rice, C. C. Wu, and F. Boichelt, “Hardness–Grain-Size Relations in Ceramics,” *Journal of the American Ceramic Society*, vol. 77, no. 10, pp. 2539–2553, Oct. 1994.
- [41] N. Hansen, “Hall–Petch relation and boundary strengthening,” *Scripta Materialia*, vol. 51, no. 8, pp. 801–806, Oct. 2004.
- [42] J. A. Wollmershauser *et al.*, “An extended hardness limit in bulk nanoceramics,” *Acta Materialia*, vol. 69, pp. 9–16, May 2014.
- [43] M. Takashiri, K. Miyazaki, S. Tanaka, J. Kurosaki, D. Nagai, and H. Tsukamoto, “Effect of grain size on thermoelectric properties of n-type nanocrystalline bismuth-telluride based thin films,” *Journal of Applied Physics*, vol. 104, no. 8, p. 084302, Oct. 2008.
- [44] D. M. Rowe, *Thermoelectrics Handbook: Macro to Nano*. CRC Press, 2005.
- [45] Z.-H. Jin and T. T. Wallace, “Functionally Graded Thermoelectric Materials with Arbitrary Property Gradations: A One-Dimensional Semianalytical Study,” *Journal of Elec Materi*, vol. 44, no. 6, pp. 1444–1449, Jun. 2015.
- [46] L. N. Vikhor and L. I. Anatyshuk, “Generator modules of segmented thermoelements,” *Energy Conversion and Management*, vol. 50, no. 9, pp. 2366–2372, Sep. 2009.
- [47] J. L. Cui, X. B. Zhao, W. M. Zhao, and Y. P. Lu, “Preparation, thermoelectric properties and interface analysis of n-type graded material FeSi₂/Bi₂Te₃,” *Materials Science and Engineering: B*, vol. 94, no. 2–3, pp. 223–228, Jun. 2002.

- [48] M. S. El-Genk and H. H. Saber, "High efficiency segmented thermoelectric uncouple for operation between 973 and 300 K," *Energy Conversion and Management*, vol. 44, no. 7, pp. 1069–1088, May 2003.
- [49] M. S. El-Genk, H. H. Saber, and T. Caillat, "A performance comparison of SiGe and skutterudite based segmented thermoelectric devices," in *AIP Conference Proceedings*, 2002, vol. 608, pp. 1007–1015.
- [50] P. H. Ngan *et al.*, "Towards high efficiency segmented thermoelectric uncouples," *Phys. Status Solidi A*, vol. 211, no. 1, pp. 9–17, Jan. 2014.
- [51] T. T. Wallace, Z.-H. Jin, and J. Su, "Efficiency of a Sandwiched Thermoelectric Material with a Graded Interlayer and Temperature-Dependent Properties," *Journal of Elec Materi*, vol. 45, no. 4, pp. 2142–2149, Feb. 2016.

CHAPTER 4 - A LAYERED FGM, CONTROLLING EFFICIENCY, AND TESTING THERMAL FATIGUE DEGRADATION IN A ZNO THERMOELECTRIC USING GRAIN SIZE GRADIENTS

This chapter shows how functionally graded material (FGM) in terms of grain size gradation is fabricated using ZnO with a Spark Plasma Sintering (SPS) by diffusion bonding layers of material sintered at different temperatures. This is another technique, in addition to the continuous gradation, that dissipates heat well for longer lasting TEGs while retaining high-energy conversion efficiency. Simulations of the efficiency versus current are conducted on samples with uniform grain size to serve as a baseline for comparison purpose. The efficiency versus current of the FGMs was simulated using uniform TE properties for each layer. The experimental thermoelectric output of the samples is measured and compared to the simulation results. The grain size has a large effect on the efficiency and efficiency range. Each sample is cycled 20 times with a fast heating rate to test thermal stress robustness against thermal expansion, shock, fatigue, and other defect degradation. The resistance at the highest temperature is measured to characterize the degradation from thermal degradation or cracking. The experimental results of the efficiency after the cycling suggest that the FGMs do not degrade as much as the baseline samples with uniform grain sizes, indicating longer lifetime may be achieved in FGMs. One sample of each material or FGM is measured for the 20 cycles, so it is a first step to realizing improved lifetime. It is necessary to test multiple samples for statistical accuracy of the results, which is proposed as future work.

4.1 INTRODUCTION

Mid- to high-temperature TE materials are subjected to thermal stresses from thermal expansion, shock, and fatigue due to aggressive heat schedules, which resulted in poor lifetime [1], [2]. Studies to mitigate thermal stresses on thermoelectric material and TEG lifetime have been done with property gradients, segmentation, and geometric pinning [2]–[7]. Strategies to reduce thermal stresses and mitigate thermal stress cracking on the side of the material exposed to the heat source has led to functionally graded materials (FGMs) by fabricating materials with thermal conductivity gradients across the length of materials. A radial thermal conductivity gradient was previously made on a circular part to reduce thermal stresses in structural materials [8], [9]. Thermal shock resistance in FGMs was first tested with a graded microstructure and composites for structural purposes [7], [10]. The idea of mitigating thermal stress with microstructure was started in Japan but was not done with grain size gradation [11]. Balak et al. have successfully processed an FGM composite for mitigating thermal shock [12]. One method to help alleviate high stresses in TEGs is geometric pinning [13], [14]. Other groups have successfully mitigated thermal stress from layering, segmentation, and composite fabrication [4], [15], [16]. Hatzikraniotis et al. characterized the efficiency and lifetime of a thermoelectric in terms of the crack degradation [17].

TE materials with large grains spread heat more effectively and provide better stability than the material with small grains [18], [19]. However, materials with small grains exhibit higher zT and efficiency than the materials with large grains. Therefore, it is imperative to have small grains in the FGMs in order to retain high efficiency [20]–[22]. Arai et al. achieved thermal stress mitigation in a thermoelectric with a compositional

gradient [23]. It was shown that the property gradient from a grain size gradation is favorable for TEGs [24]. FGM is one way to change the efficiency and affect the temperature range of a thermoelectric because of the inherent property gradient [25]. In addition, property gradients in terms of carrier concentration improved the efficiency by 3-8 % and affected the useful temperature range [26]–[28]. One method for FGM TEGs is grain size gradation exposing the large-grained side to the heat source. The small grains on cold side retain the high efficiency.

A previous study [24] showed that a continuous grain size gradation improved the temperature range in ZnO. Theoretical work done by Zabrocki et al [29] and Jin et al. [25],[26] showed that the efficiency could be improved if linear, exponential, or sigmoidal distributions in the Seebeck coefficient, resistivity, and thermal conductivity are achieved. Those proposed gradations are difficult to achieve in practice but show that functionally graded materials will improve thermoelectric efficiency. A property gradation is achievable with a continuous grains size gradation as well as a layered grain size gradation. The concept of a graded interlayer was introduced, modeled, and experimentally tested. Studies showed that layers of different material with graded thermoelectric properties will improve the efficiency. [30]. Ceramic processing of interlayers has been achieved with mechanical systems and air furnaces [31], and plasma sintering machines have been used to diffusion bond materials together to form intimate interfaces [32].

In this study, the energy conversion efficiency is simulated using the model in [25] for a five-layer ZnO FGM; continuous ZnO FGM; and homogeneous, uniform grain size ZnO with an average grain size of 180 nm, 1400 nm and 540 nm, respectively. For the two FGM specimens, the small grain size (180 nm) is at the cold side and the large grain size (1400

nm) is at the hot side. The material properties for the homogeneous ZnO specimens are taken at the midpoint of the temperature range (between $T_c = 400$ K at the cold side and $T_h = 900$ K at the hot side). The temperature-dependence of the FGM properties is included approximately by considering the layer location and the temperature field which does not deviate significantly from the linear distribution. The efficiency, η , is calculated using a multilayered material model [25] as following:

$$\eta = \frac{J \sum_{n=0}^N S_N (T_{n+1} - T_n) + J^2 \sum_{n=0}^N \rho_n h_n}{-k_N \frac{T_h - T_N}{h_N} + \frac{1}{2} \rho_N J^2 h_N + J S_N T_h} \quad (4.1)$$

where J is the current density, T_n ($n = 1, 2, \dots, N$) are the temperatures at the interfaces between the layers, $T_0 = T_c$, $T_{N+1} = T_h$, k_n , S_n , and ρ_n are the thermal conductivity, Seebeck coefficient and electrical resistivity of the n th layer, respectively, and h_n is the thickness of the n th layer. For the five-layer FGM, $N = 4$ in Equation (4.1), number of interfaces, and the measured properties are used. For the continuous FGM, N must be large to simulate the continuous property gradation. N is taken as 100 in the simulation and the property gradation is assumed to follow an exponential distribution that also approximately fits the measured data for the five-layer FGM. The contact resistance at the layer interfaces for the five-layer FGM is not considered.

In our system, a gradation is made with discrete layers of the same material but varying microstructure to mimic the same gradation as seen in a continuous system. The layered grain size gradation is achieved by bonding the individual layers together with heat. The layered method explores a parallel manufacturing method for FGMs to the continuously graded approach, compares properties to the continuously graded system, and helps model the grain size gradation for potential optimization of custom

thermoelectric applications. The microstructure not only provides a method to mitigate the thermal stress cracking but also accounts for a property gradation that affects the thermoelectric output. Having the same material allows for better interfaces and limited extra contact resistance in an FGM as opposed to a segmented design.

4.2 PROCEDURE

Using the grain size distribution in a continuously graded sample [24], layers of material are sintered individually with similar conditions to get a stack of material with the same grain size distribution but in discrete layers instead of a continuous gradation. The first layer is sintered to mimic the minimum grain size in the continuous sample, and then the proceeding layers are sintered with higher temperatures until the last layer is close to the maximum grain size in the continuous sample. The layers are each 2 mm in thickness, and there are five discrete layers that were sintered at 400, 500, 600, 700, and 800°C. Five layers are done because that is the maximum amount layers the current work could physically work with; more layers mean the layers would be thinner and more arduous for post processing. These layers are each sintered with 2% adsorbed water that gets added to the green body. The effects of using water are explained elsewhere [33], [34]. All samples are sintering to 97-99% theoretical density and measured by geometric, Archimedes, and areal density. These samples are polished with 320 grit sand paper and then put back in the SPS for a heat treatment at 700°C with a slow heating rate to diffusion bond the layers together into a fully consolidated, layered FGM sample. Once the hold temperature is reached, the load is increased slightly from 3 MPa to 10 MPa to encourage surface intimacy and bonding.

The discrete layered FGM is compared to the continuous FGM's efficiency both in a model and experimentally. The two FGMs are compared to baseline uniform samples of small, mid-sized, and large grains in terms of thermoelectric efficiency. The layered FGM provides a parallel processing technique to the continuous method without using complex SPS tooling. Effects of the grain size on the efficiency and current range are investigated.

The properties of individual layers are measured and input into the model to simulate the FGM. The properties of the uniform grain size layers # 1-5 are measured with thin samples on a ULVAC ZEM-3 TEG tester with samples setup schematically below in Figure 4.1.

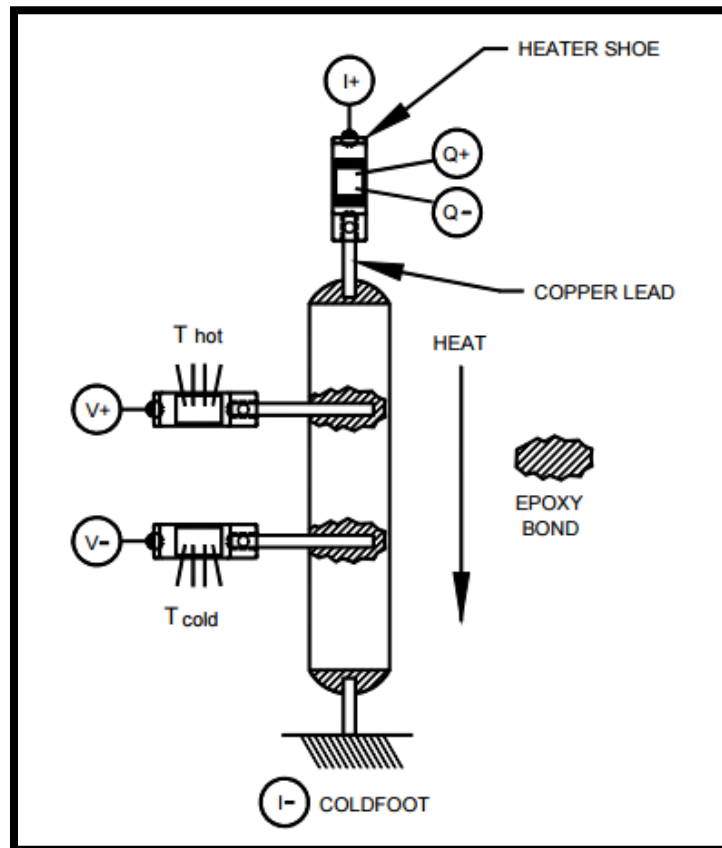


Figure 4.1: Sample setup for TEG testing on a ZEM-3 from ULVAC.

The grain size of the cross section of the layered FGM is investigated with SEM to compare to the continuous sample and ensure that minimal grain growth occurred in the diffusion-bonded sample. Also, SEM of the diffusion bonding investigates the intimacy of contact between the layers. A model from the work of Jin and Wallace [25], [30], [35] is used to simulate the efficiency versus current density for large, small, and an intermediate grain size as well as the continuous and five-layer FGMs.

For the experimental validation of the model, a test rig for large temperature differences is made for the thermoelectric output measurements. Before building the test rig, a COMSOL model is done as shown in Figure 4.2 where a cartridge heater is insulated and heat is concentrated onto a TEG sample. The model shows that a large temperature difference is achieved with a heater flux of 400 W.

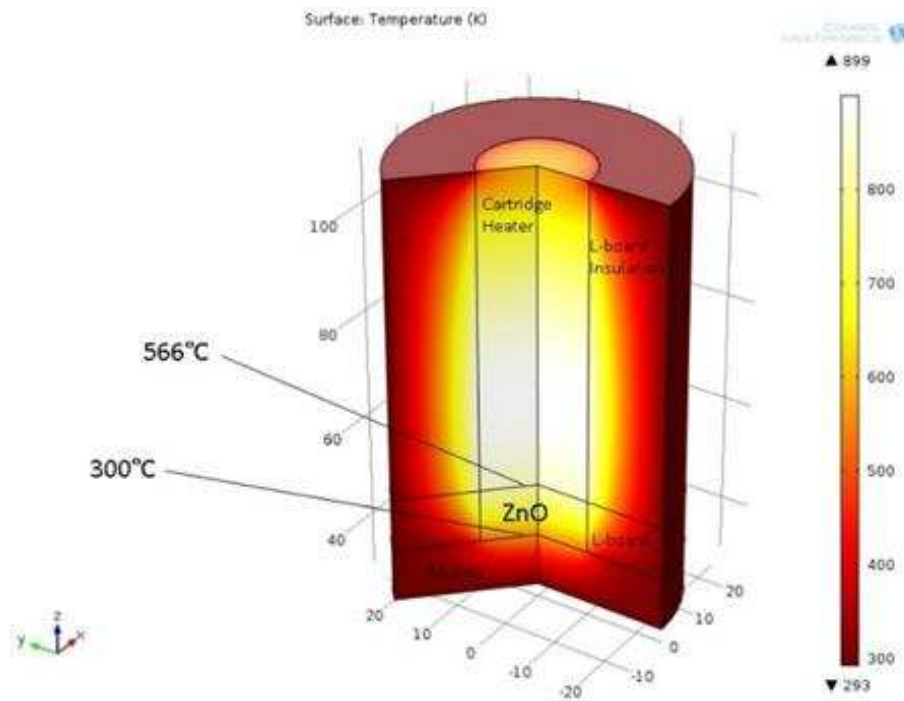


Figure 4.2: COMSOL simulation of thermoelectric tester rig for large temperature difference across the sample.

The experimental setup is shown in Figure 4.3. In the setup, the cartridge heater is insulated with L-board insulation squares, and a large power supply is connected for electrical power and for controls. The voltages and resistances are measured with an Agilent 34970a. A LabVIEW program and DAQ control is setup to control the heating and measure the appropriate values for TEG properties, namely the voltage across the sample and the resistance of the sample.

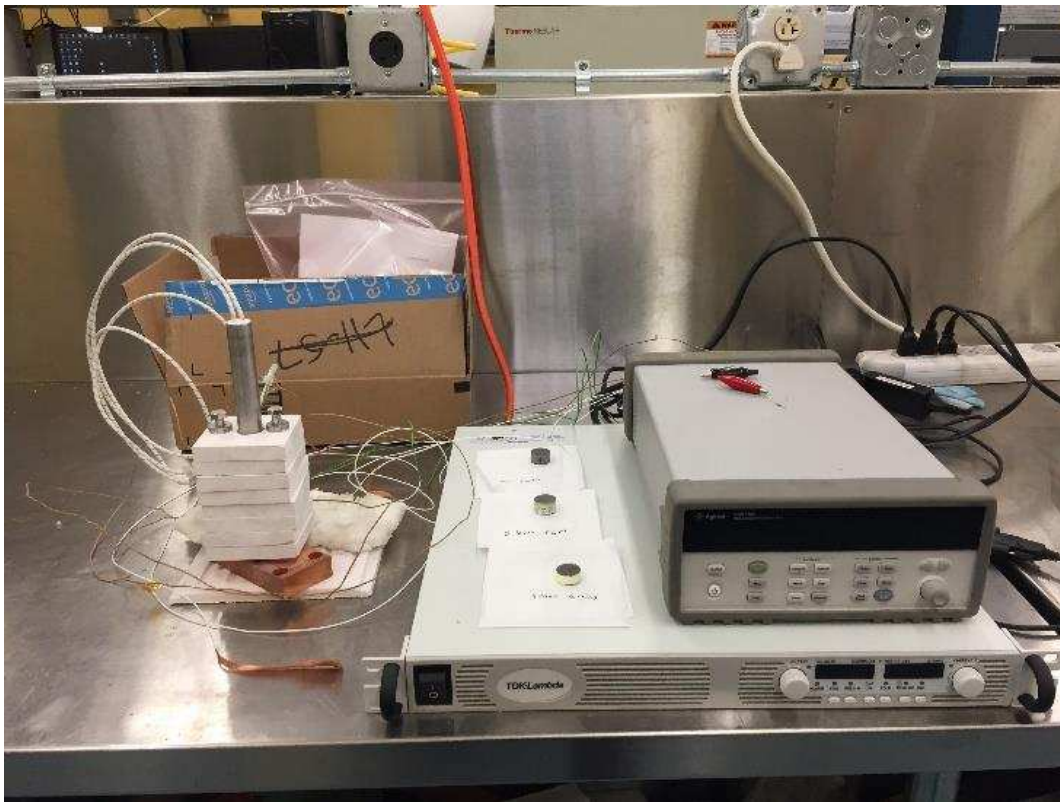


Figure 4.3: Thermoelectric tester setup.

Since there is no ASTM standard for lifetime testing of TEGs, a testing strategy for degradation in terms of properties is implemented. The only property to significantly degrade is the resistivity. The resistance at the end of the heating cycle is thus monitored by measuring at 600°C. The resistance degradation most likely resulted from thermal

cracking. Previous studies have analyzed the lifetime of TEGs by monitoring the property degradation [2], [13].

4.3 RESULTS AND DISCUSSION

Diffusion bonding of the five-layer FGM is intimate and the resistance of the sample is close to predictions. The reason for five layers of two mm each is to obtain a sample with the same height as the continuous FGM for comparable thermoelectric property testing. A look at the macroscopic layered sample is shown in Figure 4.4. The macroscopic image shows the layers after bonding. The samples are mostly white corresponding to correct stoichiometry. The layers are intimately bonded, but there are some minor cracks from processing during the diffusion bond step.

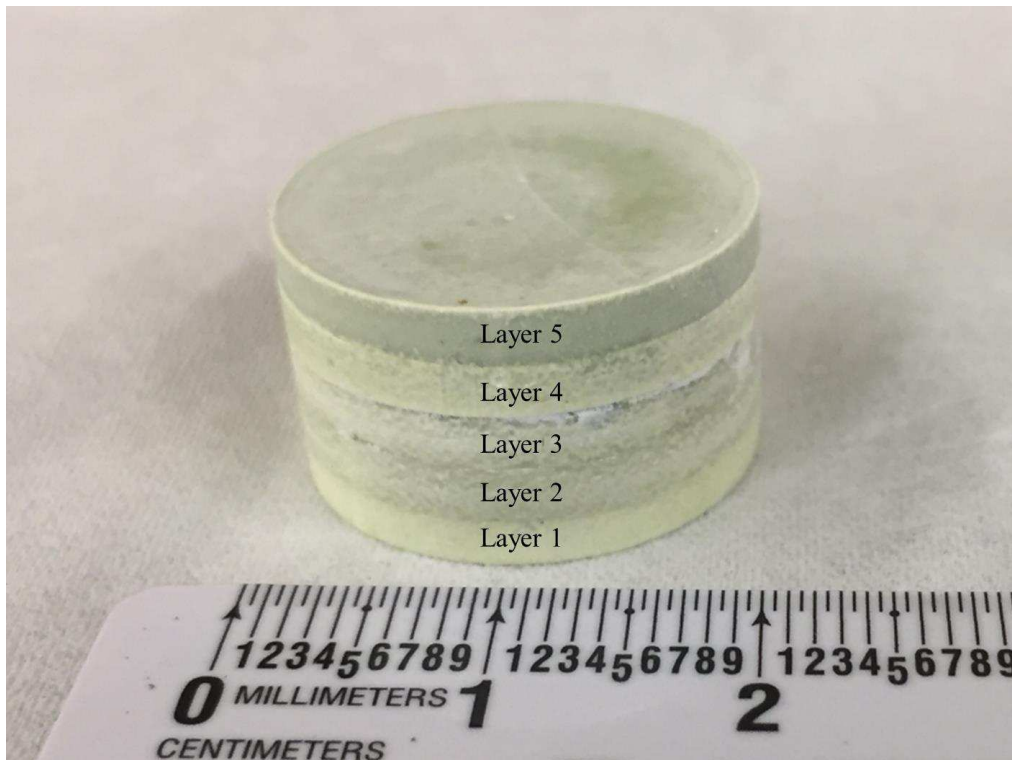


Figure 4.4: Macroscopic image of the five-layer FGM sample.

SEM of the individual layers is done to show the grain size and distribution. The images can be seen in Figure 4.5. Statistics are done to find the average value as well as the standard deviation. The images show the grainy microstructure, and it is easy to depict specific grains of ZnO. There are some large grains amongst the smaller ones in layer #s 1 and 2, which is inherent to sintering because larger grains grow at the cost of other shrinking, but the small ones eventually evolve closer to the size of the larger ones with increased sintering temperature.

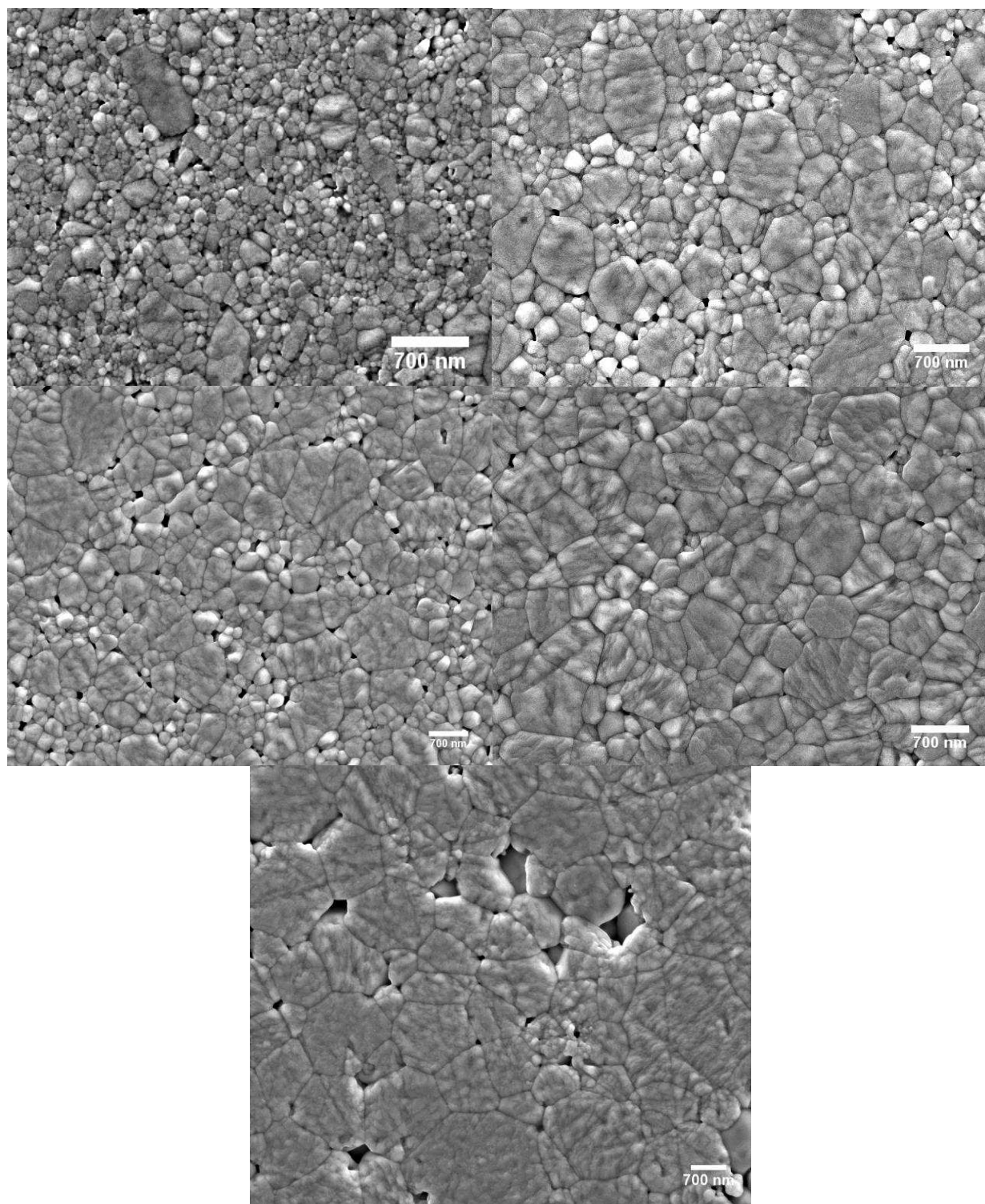


Figure 4.5: SEM images of individual layers where the top left is layer # 1, top right is layer # 2, middle left is layer # 3, middle right is layer # 4, and the bottom is layer # 5.

The grain sizes are very distinct as in Table 4.1. There is minimal grain growth and cracking after bonding the samples together. The grain sizes for each layer have relatively large distribution in size which is attributed to the grain growth during sintering. Also, the grain size standard deviation increases with the sintering temperature. The grain sizes are consistent with the gradation in the continuous sample except that there are discrete two mm sections of grain size distribution instead of the continuous gradation.

Table 4.1: Sintering Conditions for Individual Layers.

Layer	Sintering conditions	Grain Size (nm)
# 1	100°C/min, 400°C, 10 min hold, 50 MPa	180 nm ± 24
# 2	125°C/min, 500°C, 10 min hold, 50 MPa	320 nm ± 76
# 3	150°C/min, 600°C, 10 min hold, 50 MPa	540 nm ± 145
# 4	175°C/min, 700°C, 10 min hold, 50 MPa	950 nm ± 240
# 5	200°C/min, 800°C, 10 min hold, 50 MPa	1400 nm ± 450

SEM of the interface between layer # 1 and #2 shows the diffusion bond. Figure 4.6 shows an SEM image of a well consolidated interface from the diffusion bonding. Sufficient mixing of ZnO at these interfaces is very important for the electrical properties. Polishing the surface of the FGM to look at the diffusion bond interface can affect the surface and cause mixing making the appearance of a good interface false. The only part of the sample that is not well bonded is near the surface, so it is not an artifact of polishing. The bond is not porous and has mixed sufficiently. To further confirm the layers are bonded well, the resistance is measured and compared to a sample that is porous.

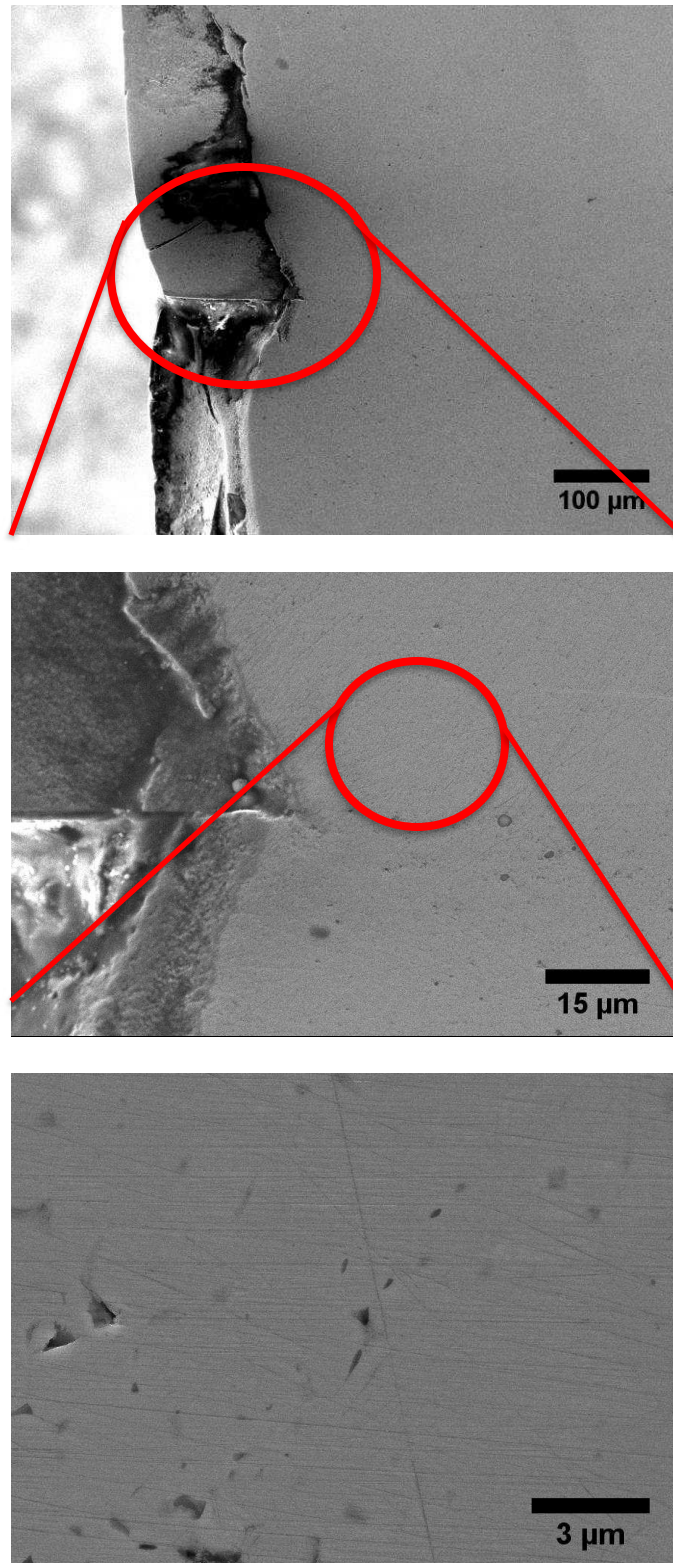


Figure 4.6: SEM images of a diffusion bonded joint in the five-layer ZnO FGM.

A model for efficiency versus current is run using the thermoelectric properties of baseline, uniform grain conditions. The properties as a function of temperature are used for the individual layers and used as the properties for the simulated five-layer FGM. Figure 4.7 shows how the grain size affects all the TE properties. Large grain samples have higher Seebeck, higher resistivity, and higher thermal conductivity.

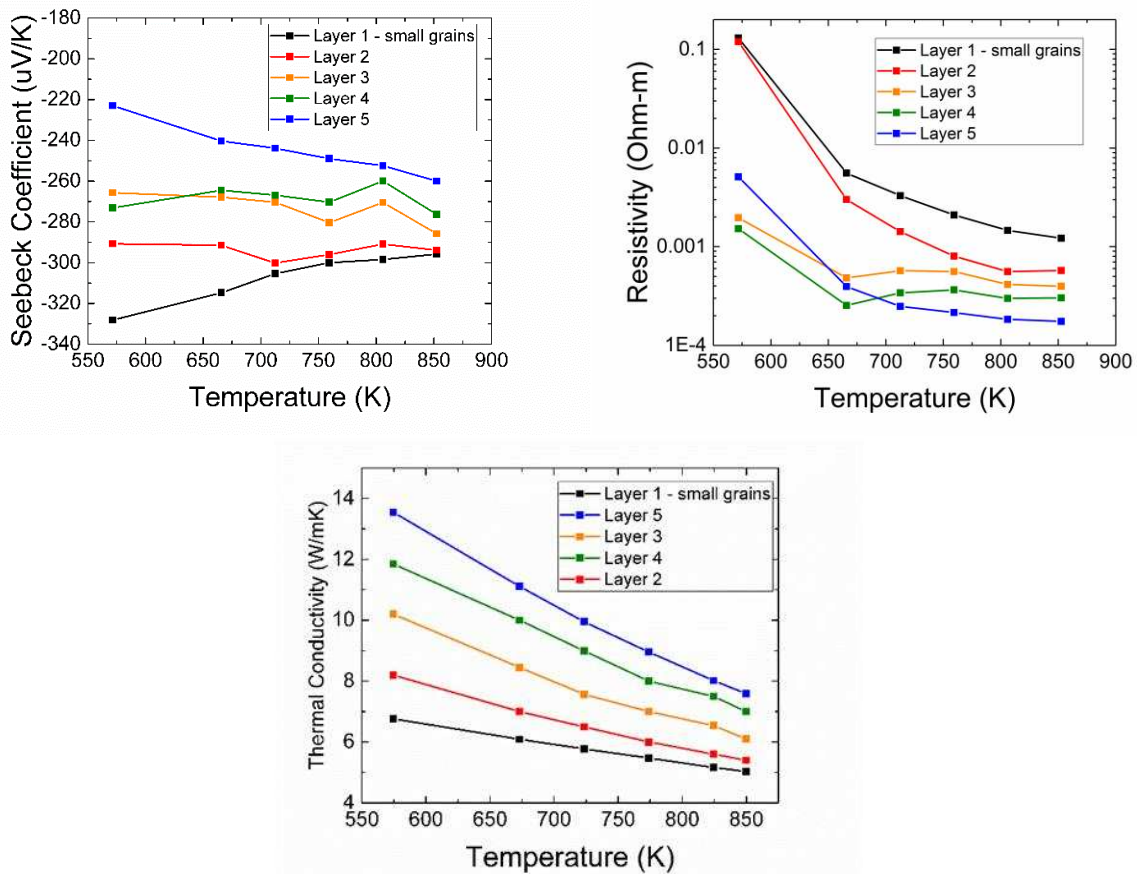


Figure 4.7: Thermoelectric property data for individual layers.

For the continuously graded sample, the properties of the layers with different grain sizes are used as in the five-layer FGM but the property trends are used in the amount of 100 layers. It clearly shows how the efficiency range changes with grain size.

Figure 4.8 shows the simulated efficiency versus current with non-dimensional efficiency for all five materials. The non-dimensional efficiency is normalized to 20% higher

than the highest efficiency of all the ZnO samples, which is the initial small-grained ZnO sample, so its peak is at 0.8. The value of the efficiencies is in the 10^{-7} range, and the zT at 600°C is 0.04. Therefore, these materials and this analysis are not meant to be used in application. We intended to use this approach to first study the grain size gradations and subsequently modify the approach to investigate more competitive materials. The ZnO with 180 nm grain size has the highest peak efficiency among the five materials. The large-grained sample with grain size around 1400 nm grain size shows the lowest efficiency. The peak efficiencies for the two FGMs are about the same and are slightly lower than that of the ZnO with 540 nm grain size. Although the FGMs do not achieve superior efficiency compared to the ZnO with smaller grain sizes, the five-layer FGM exhibits the highest peak efficiency after the specimens were subjected to 20 cycles of thermal shocks as shown in the following section on the effect of thermal fatigue on the efficiency. Moreover, the FGMs have a larger useful current range and the peak efficiencies for the FGMs occur at a higher current, as shown in Figure 4.9.

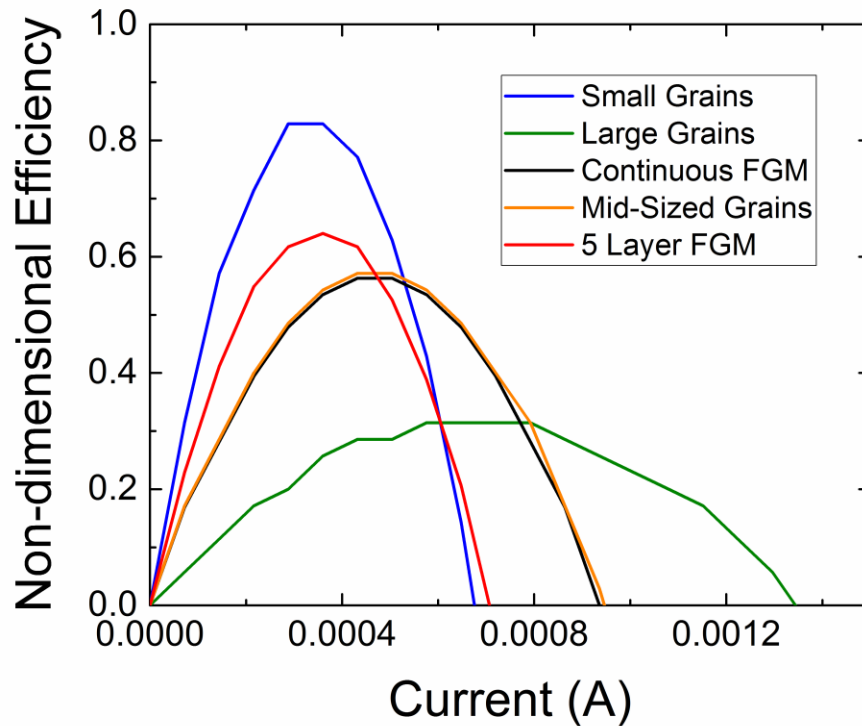


Figure 4.8: Simulated data of efficiency versus current for the model for small, large, and intermediate grains sizes as well as continuous and five-layer FGM.

Experimental results also validate the model, as shown in Figure 4.9. Samples are subjected to a large heat flux on the hot side with maximum temperature of 600°C while the cold side is passively cooled with a copper block. The experimental results roughly show the same trends as the model except the current is slightly higher in the model most likely due to inherent losses with experiments. Some other differences include a wider range in the five-layer FGM and less efficient continuous sample from the experiments. Clearly, the experiments show the correct trends from the model; thus, giving validity to the model and proving that the grain size plays a huge role on the efficiency of a thermoelectric. By processing with different grains sizes, the peak efficiency shifts from low to high current when using small to large grains respectively. The peak efficiency is

highest in the small grains. The efficiency range is widest in large grains. Grain size is effectively a design variable from these data.

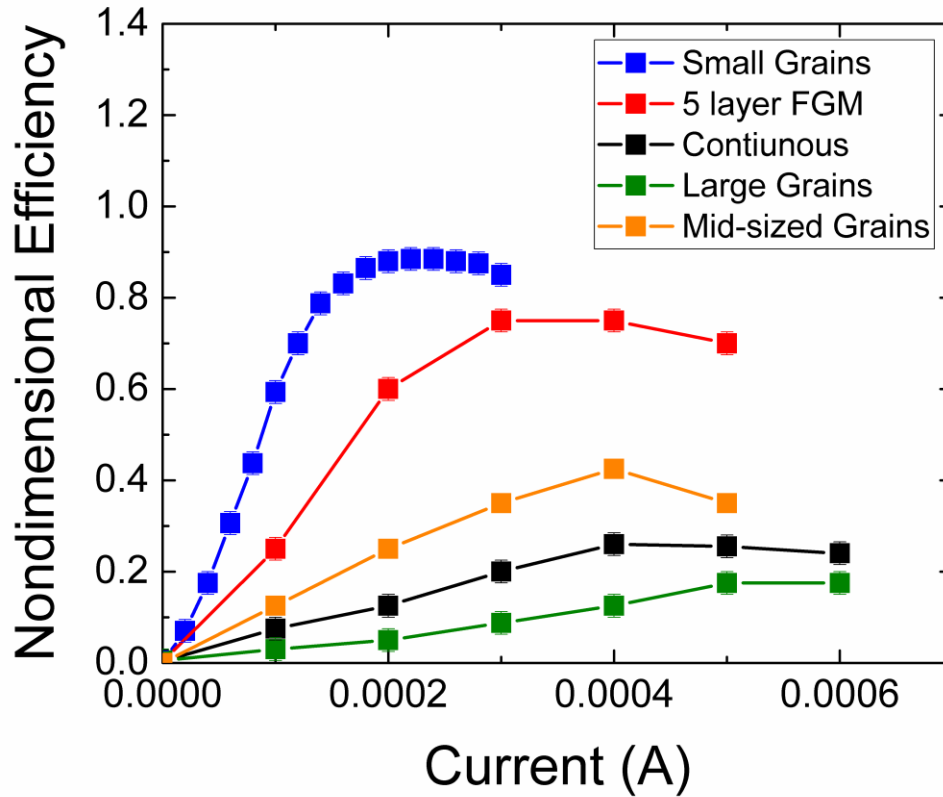


Figure 4.9: Experimental results for efficiency versus current for small, large, and intermediate grains sizes as well as continuous and five-layer FGMs before thermal shock tests.

Since the efficiencies and efficiency ranges are known for the uniform grain size samples and the FGMs, the lifetime of these samples is tested. A 20-cycle aggressive, continuous lifetime test is done on all the samples and the electrical resistance at 600°C is measured at the end of each cycle. The heating schedule of five cycles can be found in Figure 4.10. The rapid heating is meant to test the materials electrical resistance change to thermal stress, along with the resulted degradation to delineate between samples.

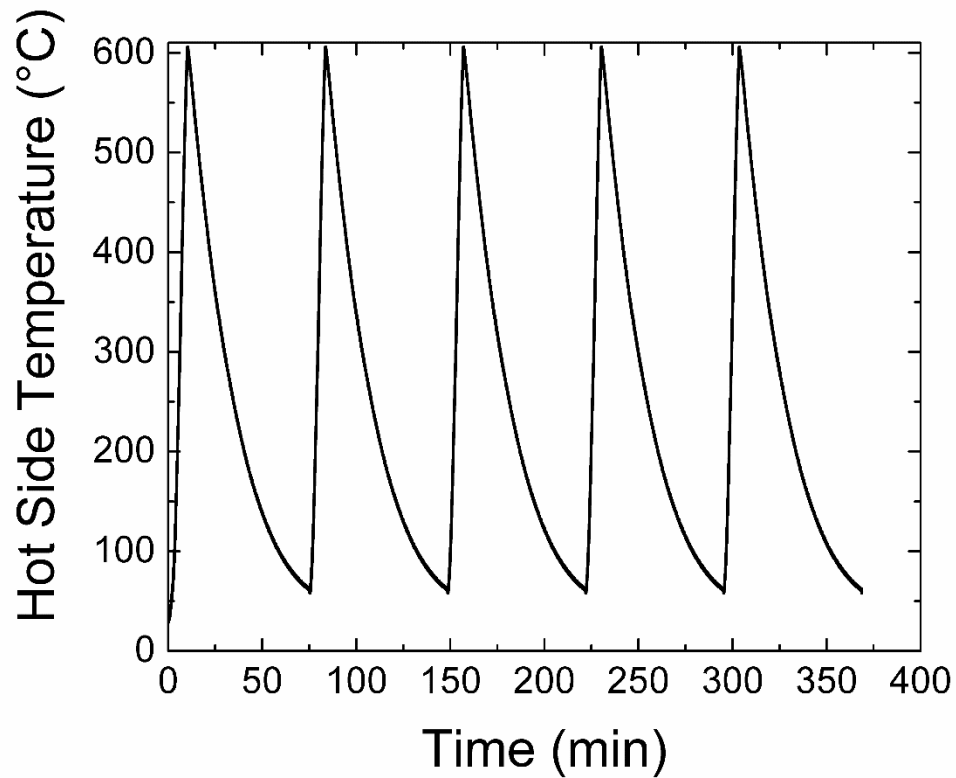


Figure 4.10: Temperature schedule of the hot side of the thermoelectric for thermal shock tests showing five cycles.

Since the resistance at room temperature is relatively hard to measure, the electrical resistance at 600°C is measured at the end of each cycle as a comparative degradation method. The resistance can be seen below for all samples. From start to 20 cycles, the resistance change is monitored then taken to be compared between the original resistance and the final resistance at the same temperature after 20 cycles as in Figure 4.11. It shows that the small and intermediate grain size sample deviate from the original values the most, and that the large grain samples as well as FGMs do not deviate as much from the values without cycling. The resistance is used as the only effective protocol as its change is the most likely property caused from small cracks from thermal stress. The resistivity of the five-layer FGM at 600°C is $\sim 2 \times 10^{-4}$ Ohm-m, which is four times better than porous ZnO of

similar grain size. This proves further that the diffusion bonding in the five-layer FGM is well mixed.

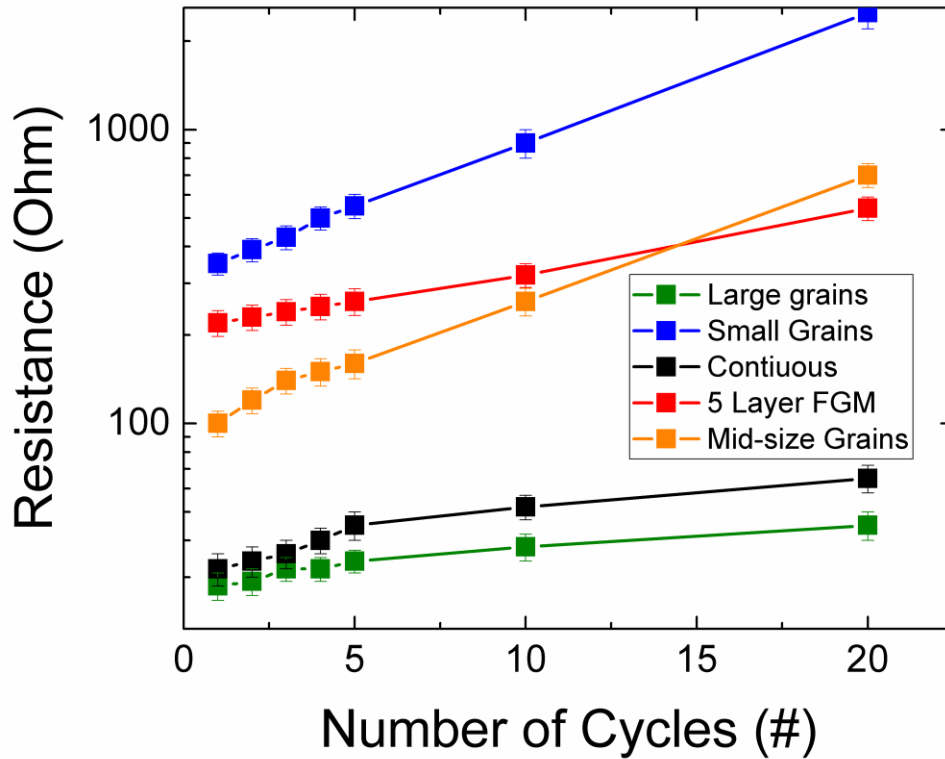


Figure 4.11: Lifetime test for small, large, and intermediate grains sizes as well as continuous and five-layer FGM. Resistance is the resistance at 600°C.

Table 4.2: Lifetime degradation percentage for small, large, and intermediate grains sizes as well as continuous and five-layer FGM.

Sample	Resistance Change (R_0/R_{final})
Small Grains	7.1
Mid-Sized Grains	7.0
Large Grains	1.6
Continuous FGM	2.0
Five-layer FGM	2.2

The efficiency of the samples is measured again after the 20 cycles. The data from the lifetime tests suggests that all samples degrade through thermal stress tests as shown in Table 4.2. This type of degradation tests are similar to Ref. [36] where thermal cycling is done and the properties are measured except our thermal cycling includes faster heating rates and higher temperatures making the degradation more remarkable at lower number of cycles. Noticeable degradation is observed in the small grain sample as well as the mid-sized grain sample. There is limited degradation seen in the large grain, continuous FGM, and five-layer FGM.

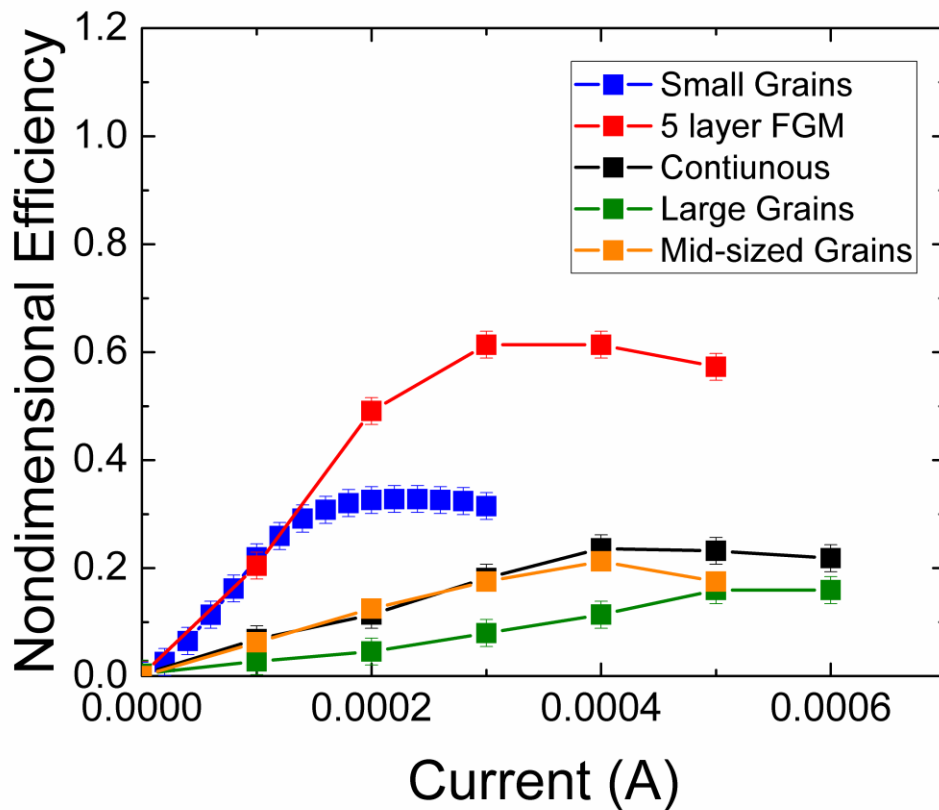


Figure 4.12: Experimental results for efficiency versus current for small, large, and intermediate grains sizes as well as continuous and five-layer FGMs 20 cycles of thermal shock tests.

The continuously graded FGM has similar degradation as the large grain sample making it an ideal candidate for long lasting transient heat applications. Unfortunately, its efficiency was not the highest among the samples tested. The five-layer FGM also has low degradation but not as low as the sample with large grains. The five-layer FGM started with high efficiency, and the efficiency remains high as the most efficient after the 20 cycles. The ability of the five-layer FGM to mitigate thermal stress and transfer heat is evident, but it is most likely more efficient because of lower thermal conductivity from many discontinuous interfaces and thicker areas of uniform grains size. The five-layer FGM has higher efficiency than the continuous FGM, but the two FGMs show similar degradation factor from the degradation of the resistance. Both FGMs would improve lifetime in transient applications with high numbers of cycling, but the five-layer FGM would be better for higher efficiency applications and the continuous would be better for wider range in terms of current and temperature.

The zT in the temperature range of 100°C to 400°C for many ZnO systems including doped polycrystalline ZnO are in the range of 10^{-5} to 10^{-2} , which already makes our pure ZnO competitive with what is currently used without thermal cycling [20]–[22]. In fact, because our ZnO FGM has higher lifetime, it would most likely be a better TEG material than what is currently used for ZnO systems. Because actual efficiencies for pure ZnO are low compared to other material used in applications, the method can be used for other bulk nanostructured systems.

4.4 CONCLUSION

The grain size FGM approach for improved thermal degradation of thermoelectrics has enhanced the lifetime using ZnO as a candidate thermoelectric material while retaining

efficiency. The grain size effects on the efficiency have been analyzed with both modeling and experimental data, and it is shown that the grain size has a large effect on the efficiency, efficiency range, and thermal degradation. FGMs in terms of grains size will last longer in the field when exposed to aggressive thermal cycling, thermal shock, and thermal fatigue. The most efficient ZnO is the small grain sample, but it degrades rapidly due to thermal stresses and thermal stability. The FGMs have higher efficiency than the large grain sample and will last longer. The five-layer FGM combines high efficiency and enhanced lifetime and the continuous FGM combines large efficiency bandwidth and enhanced lifetime over uniform grain size samples. These types of FGMs can be optimized and engineered for certain lifetime as well as efficiency ranges, and the FGMs provide a method to engineering TEGs that could possess high efficiency even after thermal stresses have occurred.

REFERENCES

- [1] Y. Hori, D. Kusano, T. Ito, and K. Izumi, "Analysis on thermo-mechanical stress of thermoelectric module," in *Eighteenth International Conference on Thermoelectrics, 1999*, 1999, pp. 328–331.
- [2] L. Bakhtaryfard and Y. S. Chen, "Design and Analysis of a Thermoelectric Module to Improve the Operational Life," *Advances in Mechanical Engineering*, vol. 7, no. 1, p. 152419, Jan. 2015.
- [3] V. Ravi *et al.*, "Thermal Expansion Studies of Selected High-Temperature Thermoelectric Materials," *Journal of Elec Materi*, vol. 38, no. 7, pp. 1433–1442, Jul. 2009.
- [4] B. L. Wang, Y. B. Guo, and C. W. Zhang, "Cracking and thermal shock resistance of a Bi₂Te₃ based thermoelectric material," *Engineering Fracture Mechanics*, vol. 152, pp. 1–9, Feb. 2016.
- [5] B.-L. Wang and Y.-W. Mai, "On Thermal Shock Behavior of Functionally Graded Materials," *Journal of Thermal Stresses*, vol. 30, no. 6, pp. 523–558, Apr. 2007.
- [6] Y. Isoda, Y. Shinohara, Y. Imai, I. A. Nishida, and O. Ohashi, "Thermal Shock Resistance and Thermoelectric Properties of Boron Doped Iron Disilicides," *Journal of the Japan Institute of Metals*, vol. 63, no. 3, pp. 391–396, 1999.
- [7] H. Takahashi, T. Ishikawa, D. Okugawa, and T. Hashida, "Laser and Plasma-Arc Thermal Shock/Fatigue Fracture Evaluation Procedure for Functionally Gradient Materials," in *Thermal Shock and Thermal Fatigue Behavior of Advanced Ceramics*, D. G. A. Schneider and P. D. D. h c mult G. Petzow, Eds. Springer Netherlands, 1993, pp. 543–554.
- [8] Y. Obata and N. Noda, "Steady Thermal Stresses in a Hollow Circular Cylinder and a Hollow Sphere of a Functionally Gradient Material," *Journal of Thermal Stresses*, vol. 17, no. 3, pp. 471–487, Jan. 1994.
- [9] D. P. H. Hasselman and G. E. Youngblood, "Enhanced Thermal Stress Resistance of Structural Ceramics with Thermal Conductivity Gradient," *Journal of the American Ceramic Society*, vol. 61, no. 1–2, pp. 49–52, Jan. 1978.
- [10] A. Kawasaki and R. Watanabe, "Fabrication of disk-shaped functionally gradient materials by hot pressing and their thermomechanical performance," *Ceramic Transactions, Functionally Gradient Materials*, vol. 34, 1993.
- [11] I. Shiota and I. A. Nishida, "Development of FGM thermoelectric materials in Japan—the state of the art," in *XVI International Conference on Thermoelectrics, 1997. Proceedings ICT '97*, 1997, pp. 364–370.
- [12] Z. Balak, M. Azizieh, H. Kafashan, M. S. Asl, and Z. Ahmadi, "Optimization of effective parameters on thermal shock resistance of ZrB₂-SiC-based composites prepared by SPS: Using Taguchi design," *Materials Chemistry and Physics*, vol. 196, pp. 333–340, Aug. 2017.
- [13] A. S. Al-Merbaty, B. S. Yilbas, and A. Z. Sahin, "Thermodynamics and thermal stress analysis of thermoelectric power generator: Influence of pin geometry on device performance," *Applied Thermal Engineering*, vol. 50, no. 1, pp. 683–692, Jan. 2013.

- [14] U. Erturun, K. Erermis, and K. Mossi, "Effect of various leg geometries on thermo-mechanical and power generation performance of thermoelectric devices," *Applied Thermal Engineering*, vol. 73, no. 1, pp. 128–141, 2014.
- [15] Z.-H. Jin and G. H. Paulino, "Transient thermal stress analysis of an edge crack in a functionally graded material," *International Journal of Fracture*, vol. 107, no. 1, pp. 73–98, Jan. 2001.
- [16] M. Sribalaji, B. Mukherjee, S. R. Bakshi, P. Arunkumar, K. Suresh Babu, and A. K. Keshri, "In-situ formed graphene nanoribbon induced toughening and thermal shock resistance of spark plasma sintered carbon nanotube reinforced titanium carbide composite," *Composites Part B: Engineering*, vol. 123, pp. 227–240, Aug. 2017.
- [17] E. Hatzikraniotis, K. T. Zorbas, I. Samaras, T. Kyratsi, and K. M. Paraskevopoulos, "Efficiency Study of a Commercial Thermoelectric Power Generator (TEG) Under Thermal Cycling," *Journal of Elec Materi*, vol. 39, no. 9, pp. 2112–2116, Sep. 2010.
- [18] Z. Li, J. Liu, H. Du, S. Li, and P. Zhang, "Thermal shock resistance of dense zirconia matrix composites evaluated by indentation techniques," *Materials Science and Engineering: A*, vol. 517, no. 1–2, pp. 154–159, Aug. 2009.
- [19] X. Q. You, T. Z. Si, N. Liu, P. P. Ren, Y. D. Xu, and J. P. Feng, "Effect of grain size on thermal shock resistance of Al₂O₃-TiC ceramics," *Ceramics International*, vol. 31, no. 1, pp. 33–38, 2005.
- [20] K. H. Kim, S. H. Shim, K. B. Shim, K. Niihara, and J. Hojo, "Microstructural and Thermoelectric Characteristics of Zinc Oxide-Based Thermoelectric Materials Fabricated Using a Spark Plasma Sintering Process," *Journal of the American Ceramic Society*, vol. 88, no. 3, pp. 628–632, Mar. 2005.
- [21] Y. Kinemuchi, M. Mikami, K. Kobayashi, K. Watari, and Y. Hotta, "Thermoelectric Properties of Nanograined ZnO," *Journal of Elec Materi*, vol. 39, no. 9, pp. 2059–2063, Dec. 2009.
- [22] S. Walia *et al.*, "Transition metal oxides – Thermoelectric properties," *Progress in Materials Science*, vol. 58, no. 8, pp. 1443–1489, Oct. 2013.
- [23] M. Arai, M. Kambe, T. Ogata, and Y. Takahashi, "Graded Compositional Design of FGM Compliant Pad for Thermoelectric Conversion Module Based on Residual Thermal Stress Analysis," *Transactions of the Japan Society of Mechanical Engineers Series A*, vol. 62, no. 594, pp. 488–492, 1996.
- [24] C. Cramer, J. Gonzalez-Julian, P. Colasuonno, and T. Holland, "Continuous functionally graded material to improve the thermoelectric properties of ZnO," *Journal of the European Ceramic Society*.
- [25] Z.-H. Jin and T. T. Wallace, "Functionally Graded Thermoelectric Materials with Arbitrary Property Gradations: A One-Dimensional Semianalytical Study," *Journal of Elec Materi*, vol. 44, no. 6, pp. 1444–1449, Jun. 2015.
- [26] E. Müller, Č. Drašar, J. Schilz, and W. A. Kaysser, "Functionally graded materials for sensor and energy applications," *Materials Science and Engineering: A*, vol. 362, no. 1–2, pp. 17–39, Dec. 2003.
- [27] Z. Dashevsky, Y. Gelbstein, I. Edry, I. Drabkin, and M. P. Dariel, "Optimization of thermoelectric efficiency in graded materials," in *Thermoelectrics, 2003 Twenty-Second International Conference on - ICT*, 2003, pp. 421–424.

- [28] A. E. Kaliazin, V. L. Kuznetsov, and D. M. Rowe, "Rigorous calculations related to functionally graded and segmented thermoelements," in *XX International Conference on Thermoelectrics, 2001. Proceedings ICT 2001*, 2001, pp. 286–292.
- [29] W. Seifert, K. Zabrocki, E. Müller, and G. J. Snyder, "Power-related compatibility and maximum electrical power output of a thermogenerator," *phys. stat. sol. (a)*, vol. 207, no. 10, pp. 2399–2406, Oct. 2010.
- [30] T. T. Wallace, Z.-H. Jin, and J. Su, "Efficiency of a Sandwiched Thermoelectric Material with a Graded Interlayer and Temperature-Dependent Properties," *Journal of Elec Materi*, pp. 1–8, Feb. 2016.
- [31] T. H. Cross and M. J. Mayo, "Ceramic-ceramic diffusion bonding using nanocrystalline interlayers," *Nanostructured Materials*, vol. 3, no. 1–6, pp. 163–168, 1993.
- [32] L. Liu, F. Ye, Y. Zhou, Z. Zhang, and Q. Hou, "Fast bonding α -SiAlON ceramics by spark plasma sintering," *Journal of the European Ceramic Society*, vol. 30, no. 12, pp. 2683–2689, Sep. 2010.
- [33] B. Dargatz *et al.*, "FAST/SPS sintering of nanocrystalline zinc oxide—Part I: Enhanced densification and formation of hydrogen-related defects in presence of adsorbed water," *Journal of the European Ceramic Society* 36.5 (2016): 1207-1220.
- [34] B. Dargatz, J. Gonzalez-Julian, M. Bram, Y. Shinoda, F. Wakai, and O. Guillon, "FAST/SPS sintering of nanocrystalline zinc oxide—Part II: Abnormal grain growth, texture and grain anisotropy," *Journal of the European Ceramic Society*. 36.5 (2016): 1221-1232.
- [35] Z.-H. Jin, T. T. Wallace, R. J. Lad, and J. Su, "Energy Conversion Efficiency of an Exponentially Graded Thermoelectric Material," *Journal of Elec Materi*, vol. 43, no. 2, pp. 308–313, Nov. 2013.
- [36] M. T. Barako, W. Park, A. M. Marconnet, M. Asheghi, and K. E. Goodson, "Thermal Cycling, Mechanical Degradation, and the Effective Figure of Merit of a Thermoelectric Module," *Journal of Elec Materi*, vol. 42, no. 3, pp. 372–381, Mar. 2013.

CHAPTER 5 – PREDICTING FGM MICROSTRUCTURE WHEN SINTERING WITH A THERMAL GRADIENT

This chapter discusses the differential sintering that occurs when sintering a material in a thermal gradient (TG). Sintering in a thermal gradient creates an FGM with grain size or porosity gradient from transient conditions. A stress shielding effect arises during sintering of a specimen subjected to a thermal gradient. This stress shielding was also present in another material system, 3% yttria stabilized tetragonal zirconia (3YSZ), which is a great candidate for grain size FGM cutting tools. The stress shielding that arises when sintering in a TG comes from differential sintering where the hotter side of the specimen experiences higher strain rate or more shrinkage compared to the colder side, which has a lower strain rate or less shrinkage simultaneously. The axial strain rates along the temperature gradient are always varied during stage 2 sintering, which is the stage where lattice and grain boundary diffusion are dominant and closing of the pore channels occurs. Using advanced sintering equations with ZnO, the value of the stress loss in the apparent strain field caused by the temperature field can be estimated using the constituent equations when viscoelastic behavior is assumed during sintering. Using an average value of the strain rate differences between the cold and hot side from the DGT during sintering, the modeling and estimation showed that an additional 13 MPa for the ZnO system sintered in a TG is needed to match the DGT. Applying this additional mechanical load to a thermal gradient FGM results in improved consistency between the thermal gradient FGM designed grain size gradient and the predictions from the DGT. Improving the accuracy of the DGT predictions of grain size is important because the grain

size greatly affects the material properties. Subsequently, the accuracy of predicting FGM microstructure will provide guidance in controlling the properties and functions for a materials design.

5.1 INTRODUCTION

In many engineering applications, formation of graded microstructure is desired in order to achieve improved properties [1]. In biomedical applications, the presence of graded porosity is beneficial to the mechanical properties [2]. In tribological applications, a graded microstructure improves the wear properties and lifetime [3]. In thermoelectric materials and cutting tools, a graded microstructure is needed for a thermal conductivity gradient. To expand the applications of the graded microstructure, it is important to predict the correlation between the processing conditions and the resultant microstructure, including porosity, density, and grain size distribution.

Use of field assisted sintering technique (FAST) to fabricate FGM materials [4]–[7] has been gaining interest because it has shown achieve graded microstructure for porosity and grain size. Porosity and microstructure FGMs have been achieved, yet the prediction of the microstructure has been a challenge in this field.

In a previous study on sintering on aluminum and nickel, deformation of the materials during sintering was measured and correlated to microscopic properties of the system [8]. Macroscopic dilatometry was applied to measure the strain rate based on applied stress and microscopic properties. The correlation is shown in Equation (5.1) where $\dot{\epsilon}_s$ is the steady-state strain rate, D is the diffusion coefficient, G is the shear modulus, b is the Burger vector, d is the grain size, σ is the applied stress, k is the Boltzman

constant, T is the temperature, p is the grain size exponent, and n is the strain rate sensitivity.

$$\dot{\varepsilon}_s = A \frac{DGb}{kT} \left(\frac{b}{d}\right)^p \left(\frac{\sigma}{G}\right)^n \quad (5.1)$$

Equation (5.1) has been used to analyze the steady-state strain rate during sintering [9], [10]. The analysis of the strain rate is important for understanding the correlation between the macroscopic deformation and the microscopic diffusion mechanisms. Different materials experience different stresses and strains around inclusions, reinforcement material, and substrates because of boundary conditions. This phenomenon is regarded as a stress shielding sintering effect, where the sintering is hindered by the stress states, or all of the forces acting on the sintering specimen [11]–[14]. Using isotropic and viscoelastic analogy for sintering, the stress can be estimated from the measured strain rates.

The continuum constituent equation for sintering, Equation (5.2), describes the correlation between applied stress, sintering stress, and the strain rate tensor acting on a material [15], which is the linear viscous case of the Skorohod-Olevski viscous sintering constitutive relationship where σ_{ij} is from external load, $\dot{\varepsilon}_{ij}$ is the strain rate tensor, η_0 is the shear viscosity of a fully dense sample, φ is the normalized shear viscosity, ψ is the normalized bulk viscosity, \dot{v} is the volume rate change of a porous body, P_L is the sintering stress, and δ_{ij} is the Kronecker symbol.

$$\sigma_{ij} = 2\eta_0 \left[\varphi \dot{\varepsilon}_{ij} + \left(\psi - \frac{1}{3} \varphi \right) \dot{v} \delta_{ij} \right] + P_L \delta_{ij} \quad (5.2)$$

Different amounts of applied stress and different stress states during sintering should be reflected in strain rate from Equation (5.2). Nevertheless, it is hard to get macroscopic data on small inclusions or small stress differences. Theoretically, a stress can be calculated from Equation (5.2) if the strain rates are known. In the current work, the stress shielding, or stress lost in the sample sintered in a TG from stress shielding or non-uniform stress distribution, is defined as the amount of stress that enables the sample sintered in a TG to overcome the stress shielding to predict the TG more accurately. The stress constraint, or stress state difference from external pressures, due to bimodal powder mixtures of steel and alumina has been predicted by measuring the largest and smallest strain rates and using the rule of mixtures to find an effective strain rate on the system [16]. Prediction of the sintering deformation of a stress shielded film showed that the isotropic constitutive laws did not work well and needed to be modified [17].

An improved transversely isotropic viscous formulation was proposed and applied to the stress shielded densification of films and sinter forging. Five constitutive parameters and two free densification rates were required to accurately predict sintering [18]. Transient stresses were investigated in a system that was shielded leading to a better understanding of varying stress states during sintering [19]. Lange and Kellett's study suggested that the strain rates were different for materials with different densities at the starting point and compensated for the slower strain rate with increased pressure [20].

A newly arising stress shielding is introduced in the present work due to sintering in a thermal gradient. In our material system, the sintering curves of samples of ZnO done with isothermal conditions of different heating rates and temperatures demonstrated different strain rates during the sintering, which are associated with different stress values.

By using the constitutive equation, the stress differences can be determined. For a viscoelastic, isotropic material, the equation for analyzing the strain rate during the sintering is shown in (5.3) where $\dot{\epsilon}_x$ is the strain rate from the dilatometer of a sintering specimen, $\dot{\epsilon}_f$ is the free sintering strain rate of the powder used, η is the property called shear viscosity, and σ is the stress.

$$\dot{\epsilon}_x = \dot{\epsilon}_f + \frac{1}{3\eta} \left[\sigma_x - \frac{1}{2} (\sigma_y + \sigma_z) \right] \quad (5.3)$$

The stress shielding can be estimated from the known strain rates measured from a dilatometer on the sintering specimen. The shear viscosity and free sintering rate must be known or previously measured for a specific powder system.

For investigation of the stress shielded system in the current work, the strain rates are different along the thickness of the sintering body. The aim is to calculate the stress shielding in specimens sintering under large thermal gradients and to improve the accuracy of prediction of the microstructure. Given the shear viscosity of a fully dense sample, the normalized shear viscosity, the applied stress, and strain rates from the samples sintered isothermally for predictions, the stress shielding value can be calculated assuming that the conditions for uniaxial compression are met [21].

Sintering in a thermal gradient produced a graded microstructure and a Master Sintering Curve (MSC) approach approximated the grain size gradient [22]. It was also shown how samples sintered isothermally for predictions using a density-grain size-time (DGT) plot overestimated the grain size of a sample sintered in a thermal gradient (TG) [23]. The stress shielding on the system arose from the varying stress and strains due to the changing temperature axially across the thickness of the specimen. This sintering

hindrance resulted in more shrinkage of the materials at the hot side and less shrinkage at the cold side simultaneously. Consequently, the hot side has a higher density than the cold side; meanwhile, the hot side also shielded the surrounding of the materials at the cold side from the same stress state compared to the case where the whole material is in an isothermal sintering condition. A schematic of the sintering effects is shown in Figure 5.1 where the different strain rates occur spatially throughout the sintering specimen. This effect is investigated in terms of stress shielding to more accurately predict a graded microstructure sintered in a large thermal gradient.

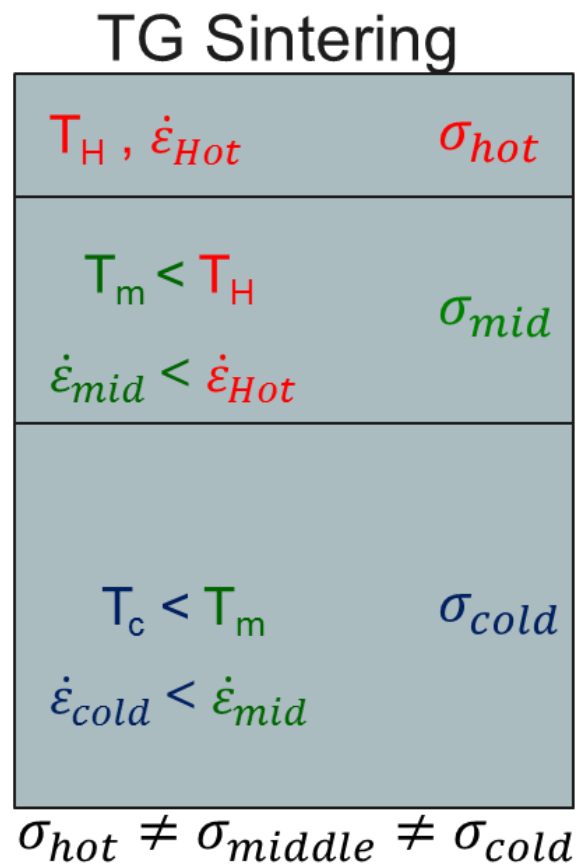


Figure 5.1: Schematic of the sintering effects in a sample sintered in a TG.

5.2 PROCEDURE

For predicting the grain size in a sample sintered in a TG, a typical SPS graphite die setup is used to sinter samples isothermally to predict the density and grain size evolution over time using an MSC approach. Three different heating schedules (175°C/min to 900°C, 125°C/min to 700°C, and 75°C/min to 500°C) were used representing the hot side, cold side, and the geometric middle, respectively. The sintering curves were plotted to show the predictive behavior that should occur in a TG sintering setup. The grain sizes are monitored for the three heating schedules at cut off times corresponding to 97% dense, half the holding time, and the full holding time. This gives a density-grain size-time (DGT) plot of conditions that can predict the final microstructure of system with differential heating schedules. The load schedule started with a low value (35 MPa) during the low temperature bake out, and it was increased to 73 MPa before the large water outgassing. The load is controlled at 0.1 kN per second. A novel sintering setup was developed for the TG to include the wide range of heating schedules in one die setup. The details on TG sintering is discussed elsewhere [23]. The grain size at the end of the sintering run from the samples sintered isothermally in the DGT and the sample sintered in a TG are compared.

The best prediction diagnostic range to analyze the stress and strain behavior during sintering is from 70-90% theoretical density because the strain rates vary drastically in this range with different heating schedules. Also, for the ZnO system, the mechanical load gets ramped after an out-gassing stage, which corresponds to a time on the DGT plot before which the data is suitable for analysis of a stress shielding effect by adding pressure to the TG system and to be compared to the original DGT. The load is maintained at a low value until the cut-off time in the DGT. Samples sintered in a TG are performed

with added pressure up to the cut-off point and compared to the isothermally sintered samples from the DGT to investigate the effects of the added pressure from estimated stress shielding.

Strain rates and stress shielding were estimated to find the amount of additional pressure needed in the sample sintered in a TG to align the results with the samples sintered isothermally for predictions of the microstructure. The maximum strain rate difference is calculated from the data derived from the DGT. Here, we predict the amount of stress shielding by using values of the normalized shear viscosity from our data and estimating a shear viscosity [24], [25]. Then by using equation (5.3) for uniaxial conditions, the stress shielding amount is estimated. Cut off TG runs are completed and compared to the DGT. The setup for the TG sintering is provided elsewhere [23]. The densities of the specimens are measured by two methods, the geometric and Archimedes methods. All FAST tooling is done with 20 mm diameters, and all plunger faces are covered with BN to negate field effects. Prior to sintering, the powder is stored in a desiccator. Eighteen grams of ZnO is used to get a fully dense material that is 10 mm thick. The powder is pressed once to consolidate into a green part; 2 wt. % water is injected in the green part; the surfaces of the plungers are sprayed with BN; subsequently the powder is pressed again to the initial sintering load.

5.3 RESULTS AND DISCUSSION

A. ZNO DGT AND TG COMPARISON

Isothermal sintering is done with ZnO for three heating schedules, 175°C/min to 900°C, 125°C/min to 700°C, and 75°C/min to 500°C, and a mechanical load starting at 35 MPa and increasing to 75 MPa after a large water outgassing to gain a predictive model for

the microstructure of the FGM ZnO. This DGT predicts a fully dense system where the average grain size is approximately 1.8 micrometers on one side of the specimen and 0.3 micrometers on the other side. The DGT plots are displayed in Figure 5.2. The standard deviation indicates that there is a large distribution in grains sizes. The standard deviation values increase with increasing grain size.

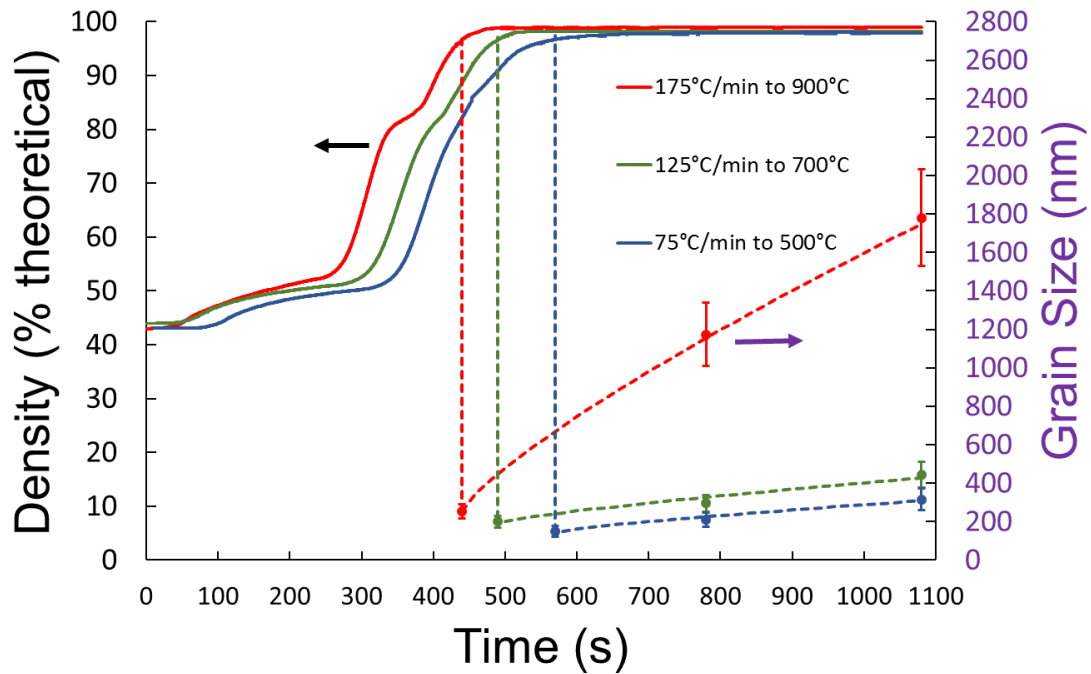


Figure 5.2: DGT plot for grain size and porosity predictions of a sample sintered in a TG when load is ramped to 73 MPa after large water outgassing.

The microstructure at different locations in the sample sintered in a TG is compared to the predicted microstructure where samples are sintered isothermally. The results and comparison are shown in Table 5.1. The average grain sizes in the samples sintered isothermally for predictions are larger than that at the corresponding locations in the specimen sintered with a thermal gradient at each condition. The aforementioned discrepancy indicates that a stress shielding is present in the thermal gradient sintering.

Table 5.1: Comparison of final grain size for a ZnO sample sintered in a TG versus samples sintered isothermally for predictions when load is ramped to 73 MPa after the large water outgassing.

Samples Sintered Isothermally (DGT)		Sample sintered in a TG (FGM)	
Condition	Grain Size (nm)	Condition	Grain Size (nm)
175°C/min to 900°C	1781 ± 617	175°C/min to 900°C	1194 ± 430
125°C/min to 700°C	436 ± 125	125°C/min to 700°C	389 ± 133
75°C/min to 500°C	316 ± 96	75°C/min to 500°C	187 ± 98

B. ZIRCONIA DGT AND TG COMPARISON

Isothermal sintering is also performed on 3YSZ (3% Ytria stabilized tetragonal zirconia) with three heating schedules, 200°C/min to 1600°C, 150°C/min to 1400°C, and 100°C/min to 1200°C, and at a constant mechanical load of 32 MPa. This DGT predicts a fully dense system where the average grain size is ~2.4 micrometers on one side and 0.3 micrometers on the other. Similar to what has been observed in the ZnO, the DGT plot (Figure 5.3) for the YSZ also shows large standard deviations in grain size distribution.

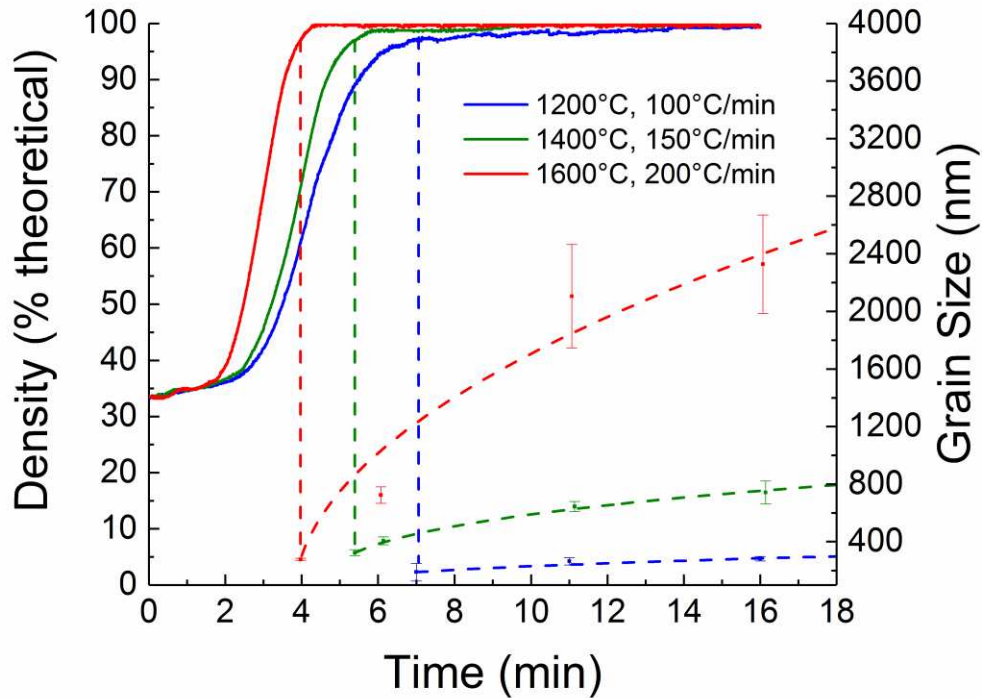


Figure 5.3: DGT plot for microstructural prediction of continuous zirconia sample done with constant load of 32 MPa.

The grain sizes at different locations of the 3YSZ sintered in a thermal gradient are compared to the samples sintered isothermally for predictions of the microstructure. The results are shown in Table 5.2. The average grain sizes in the samples sintered isothermally for predictions are larger than that at the corresponding locations in the specimen sintered in a TG. Again, the discrepancy indicates that a stress shielding is present in the thermal gradient sintering just as in the ZnO. In the 3YSZ system, the sample sintered in a TG is not fully dense along 10 mm; it is fully dense for about 7 mm of the target 10 mm length, so the grain size is not calculated past the 7-mm point as shown in Figure 5.4. The phenomenon suggests that the same stress shielding occurs in another materials system. Therefore, the stress shielding effect on samples sintered in a TG is not limited to ZnO system, nor is it due to the ramping in pressure applied to the ZnO system.

Table 5.2: Comparison of final grain size for zirconia sintered in a TG versus samples sintered isothermally for predictions.

Isothermal Sintering(DGT)		Thermal Gradient Sintering	
Condition	End Grain Size (nm)	Condition	Grain Size (nm)
200°C/min to 900°C	2387 ± 567	200°C/min to 900°C	1489 ± 523
150°C/min to 700°C	792 ± 123	150°C/min to 700°C	321 ± 112
100°C/min to 500°C	302 ± 87	100°C/min to 500°C	90% dense

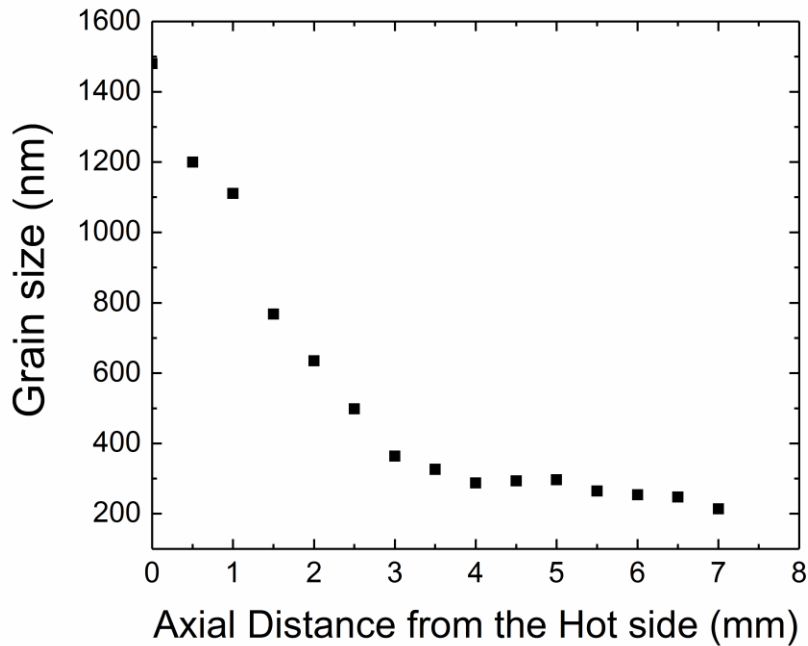


Figure 5.4: Grain size gradation of fully dense thermal gradient sample.

C. ANALYZING THE STRESS SHIELDING IN A TG USING ZNO

Cut-off runs of the samples sintered in a TG are processed by stopping the run at the time where the load of the DGT isothermal experiments begin to increase. For the cut-off runs, the microstructure that is compared in the density because the sample is not fully dense at the cut-off point. DGT samples are processed by ramping the mechanical load during outgassing due to high pressures from adsorbed water. By cutting off the TG at the

cut-off time, it allows for extra mechanical load to be used when processing the sample sintered in a TG. The cut-off scenario provides a case where mechanical load can be added to the sample sintered in a TG to compare the results to the DGT cut-off point. This will help identify the stress needed to overcome the stress shielding and align with the DGT. This cut off point can be seen in Figure 5.5. Since the DGT has a mechanical load starting at 35 MPa before the cutoff, a TG with the same load and cutoff time is fabricated to compare. Table 5.3 shows that the sample sintered in a TG with 35 MPa that was cut off is an underestimate of the density compared to the density of the cut-off point in the DGT done with 35 MPa.

Table 5.3: Theoretical density results of ZnO sample sintered in a TG cut off runs and the 35 MPa DGT samples sintered isothermally for predictions at a time of 385 seconds.

Heating schedule	Isothermal Sintering (DGT)	Thermal Gradient Sintering		
		35 MPa (11 kN)	73 MPa (23 kN)	48 MPa (15 kN)
175°C/min to 900°C	85%	76%	89%	87%
125°C/min to 700°C	79%	70%	86%	80%
75°C/min to 500°C	67%	62%	80%	71%

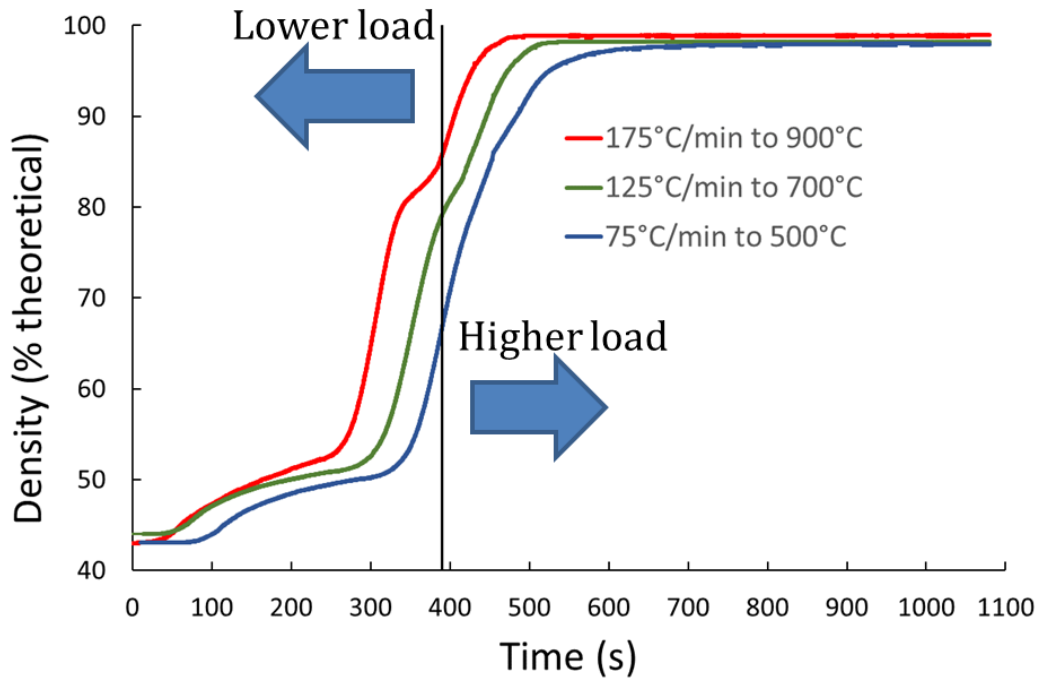


Figure 5.5: ZnO DGT (sans grain size) of for spatial predictions from a DGT with mechanical load of 35 MPa (11 kN) showing the cut off time of 385 seconds.

The strain rates are extracted from the portion of the DGT that corresponds to stage 2 sintering from about 70-90% density. From the portion of the DGT where significant densification occurs, the strain rates for the system are very different in magnitude and vary in time as shown in Figure 5.6. These are the strain rates that affect the sintering behavior the most, and the hot side has a vastly different strain rate compared to the cold side.

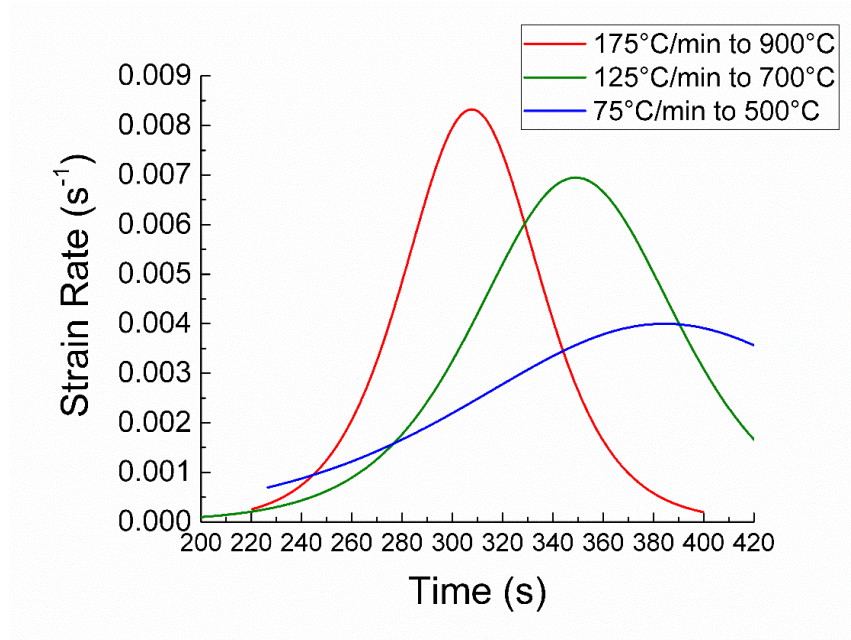


Figure 5.6: ZnO Strain rates for TG spatial predictions from a DGT where the applied load is 35 MPa (11 kN).

Based on the strain rates from Figure 5.6, the constitutive equation, and an estimate of the viscous properties, the stress difference can be calculated [25], [26]. A larger load of 73 MPa, which is the starting load, 35 MPa, plus the load corresponding to the maximum strain rate difference from the constitutive equation, is used to fabricate the sample sintered in a TG with the same cut-off time. Table 5.3 shows that the sample sintered in a TG is an overestimate of the density with that mechanical load. This proves that using the maximum strain rate difference in the system is not the most accurate way of predicting the loss of evenly distributed stress in a sample sintered in a TG.

Varying strain rates spatially leads to a more analysis of the stress shielding. For the time that most of the densification occurs, the strain rates vary, but the maximum strain does not occur the whole time as shown in Figure 5.7. If the maximum strain rate did occur the entire sintering time, then the prediction using the maximum strain rate should line up with the sample sintered in a TG that was cut-off sample; however, this is not the case.

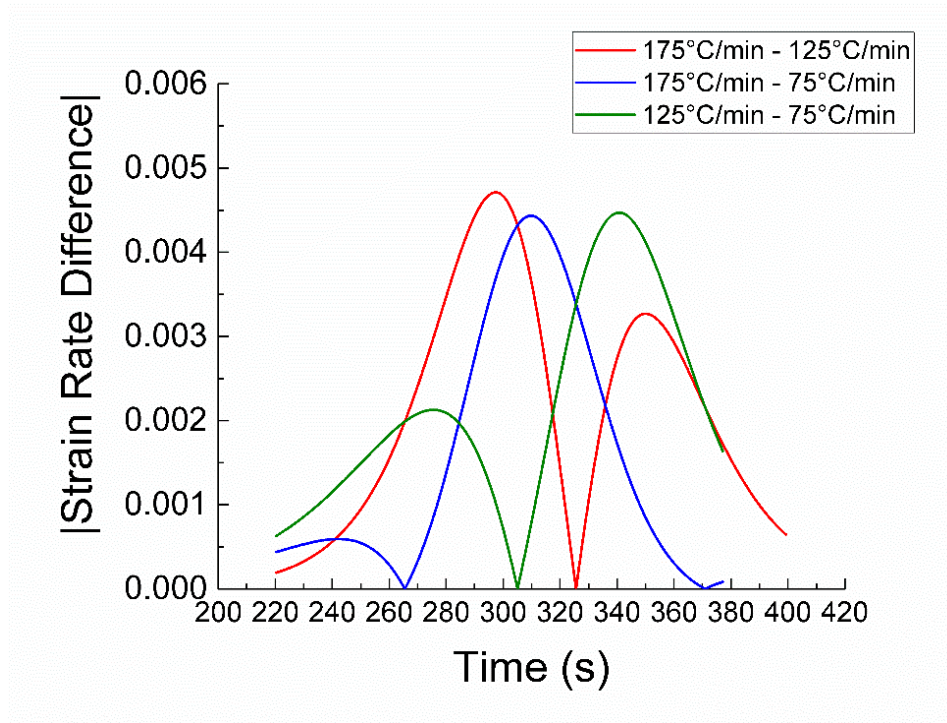


Figure 5.7: ZnO Strain rate differences versus time for the different heating schedules.

Instead of using the maximum strain rate difference to calculate the stress shielding, the average strain rate difference is used to estimate the stress shielding on the TG system. This load is the starting load, 35 MPa, plus the load corresponding to the average strain rate difference from the constitutive equation, 13 MPa, for a total of 48 MPa. Table 5.3 shows results from the cut off run with 48 MPa. It is observed that the grain size follows the DGT within 2-3%.

Using the average strain rate difference provides a more accurate way of providing a value of the stress shielding effect so that the microstructural evolves more closely to the DGT. The value of the stress shielding is about 13 MPa for the system analyzed, meaning that is the minimum amount of extra external load to apply to the sample sintered in a TG to overcome the stress shielding. The maximum stress shielding is about 38 MPa from

stress and strain calculations with the largest strain rate difference, but that happens only for a short period of time during densification. This is significant for the realm of pressure assisted sintering because on a scaling note, the sintering stress is usually around 0.5-1 MPa. This is also important for FGMs that rely on accurate grain sizes for targeted properties. It has been shown that TEGs benefit from this type of gradation in [23]. Therefore, it is important improve the accuracy of predictions on the grain size gradation. Other applications that can benefit from this microstructural gradation includes cutting materials for heat spreading while retaining strength [27], [28], and impact resistant materials [29].

5.4 CONCLUSIONS

There is a stress shielding on the sintering of specimens subjected to thermal gradients that comes from the differential strain rates occurring axially from the temperature field. The stress state at the hot end of a specimen sintered in a TG differs from the cold side during densification. As a result, the grain size distribution of a specimen sintered under a thermal gradient cannot be accurately predicted using the samples sintered isothermally. To further analyze the prediction, the difference in strain rates is measured and the average strain rate difference is used to calculate the stress shielding value. The mechanical load to be used on the sample sintered in a TG should include the mechanical load used with the samples sintered isothermally for predictions plus the estimated stress shielding. The approach considering the stress shielding provides a more accurate prediction of the microstructure based on results from the cut off runs that are within 2-3% of the predicted density values. This finding will guide future designs that

call for microstructural gradients in terms of porosity and grain size with improved accuracy in the microstructure predictions.

REFERENCES

- [1] M. Naebe and K. Shirvanimoghaddam, "Functionally graded materials: A review of fabrication and properties," *Applied Materials Today*, vol. 5, pp. 223–245, Dec. 2016.
- [2] W. Pompe *et al.*, "Functionally graded materials for biomedical applications," *Materials Science and Engineering: A*, vol. 362, no. 1–2, pp. 40–60, Dec. 2003.
- [3] Y. Watanabe, Q. Zhou, H. Sato, T. Fujii, and T. Inamura, "Microstructures of Al–Al₃Ti functionally graded materials fabricated by centrifugal solid-particle method and centrifugal in situ method," *Jpn. J. Appl. Phys.*, vol. 56, no. 1S, p. 01AG01, Nov. 2016.
- [4] L. P. Bulat *et al.*, "On fabrication of functionally graded thermoelectric materials by spark plasma sintering," *Tech. Phys. Lett.*, vol. 40, no. 11, pp. 972–975, Dec. 2014.
- [5] Z. Zhang, X. Shen, C. Zhang, S. Wei, S. Lee, and F. Wang, "A new rapid route to in-situ synthesize TiB–Ti system functionally graded materials using spark plasma sintering method," *Materials Science and Engineering: A*, vol. 565, pp. 326–332, Mar. 2013.
- [6] S. Wei *et al.*, "Simulation of temperature and stress distributions in functionally graded materials synthesized by a spark plasma sintering process," *Computational Materials Science*, vol. 60, pp. 168–175, Jul. 2012.
- [7] Y. Zhang, Z. Li, C. Li, and Z. Yu, "Temperature gradient field sintering of Ti–TiB–TiB₂ functionally graded material," *Ceramics International*, vol. 41, no. 10, Part A, pp. 13844–13849, Dec. 2015.
- [8] J. E. Bird, A. K. Mukherjee, and J. E. Dorn, "Quantitative Relation between Properties and Microstructure, ed. by DG Brandon and A," *Rosen (Israel Univ. P., Jerusalem, 1969)* pp, pp. 255–342, 1969.
- [9] M. n. Rahaman, L. c. De Jonghe, and C. h. Hsueh, "Creep During Sintering of Porous Compacts," *Journal of the American Ceramic Society*, vol. 69, no. 1, pp. 58–60, Jan. 1986.
- [10] M. N. Rahaman, L. C. De Jonghe, and M.-Y. Chu, "Effect of Green Density on Densification and Creep During Sintering," *Journal of the American Ceramic Society*, vol. 74, no. 3, pp. 514–519, Mar. 1991.
- [11] D. J. Green, O. Guillon, and J. Rödel, "Constrained sintering: A delicate balance of scales," *Journal of the European Ceramic Society*, vol. 28, no. 7, pp. 1451–1466, 2008.
- [12] R. K. Bordia and G. W. Scherer, "On constrained sintering—I. Constitutive model for a sintering body," *Acta metallurgica*, vol. 36, no. 9, pp. 2393–2397, 1988.
- [13] R. K. Bordia and R. Raj, "Sintering Behavior of Ceramic Films Constrained by a Rigid Substrate," *Journal of the American Ceramic Society*, vol. 68, no. 6, pp. 287–292, Jun. 1985.
- [14] G. W. Scherer and T. Garino, "Viscous Sintering on a Rigid Substrate," *Journal of the American Ceramic Society*, vol. 68, no. 4, pp. 216–220, Apr. 1985.
- [15] E. A. Olevsky, "Theory of sintering: from discrete to continuum," *Materials Science and Engineering: R: Reports*, vol. 23, no. 2, pp. 41–100, Jun. 1998.
- [16] R. M. German, "Prediction of sintered density for bimodal powder mixtures," *MTA*, vol. 23, no. 5, pp. 1455–1465, May 1992.
- [17] F. Li, J. Pan, O. Guillon, and A. Cocks, "Predicting sintering deformation of ceramic film constrained by rigid substrate using anisotropic constitutive law," *Acta Materialia*, vol. 58, no. 18, pp. 5980–5988, Oct. 2010.

- [18] R. K. Bordia, R. Zuo, O. Guillon, S. M. Salamone, and J. Rödel, "Anisotropic constitutive laws for sintering bodies," *Acta Materialia*, vol. 54, no. 1, pp. 111–118, Jan. 2006.
- [19] L. C. De Jonghe, M. N. Rahaman, and C. H. Hsueh, "Transient stresses in bimodal compacts during sintering," *Acta Metallurgica*, vol. 34, no. 7, pp. 1467–1471, Jul. 1986.
- [20] B. Kellett and F. F. Lange, "Stresses Induced by Differential Sintering in Powder Compacts," *Journal of the American Ceramic Society*, vol. 67, no. 5, pp. 369–371, May 1984.
- [21] S.-Y. Tzeng and J.-H. Jean, "Stress Development during Constrained Sintering of Alumina/Glass/Alumina Sandwich Structure," *Journal of the American Ceramic Society*, vol. 85, no. 2, pp. 335–340, Feb. 2002.
- [22] K. G. Ewsuk, D. T. Ellerby, and C. B. DiAntonio, "Analysis of Nanocrystalline and Microcrystalline ZnO Sintering Using Master Sintering Curves," *Journal of the American Ceramic Society*, vol. 89, no. 6, pp. 2003–2009, Jun. 2006.
- [23] C. Cramer, J. Gonzalez-Julian, P. Colasuonno, and T. Holland, "Continuous functionally graded material to improve the thermoelectric properties of ZnO," *Journal of the European Ceramic Society*.
- [24] E. Olevsky and L. Froyen, "Constitutive modeling of spark-plasma sintering of conductive materials," *Scripta Materialia*, vol. 55, no. 12, pp. 1175–1178, Dec. 2006.
- [25] E. A. Olevsky, V. Tikare, and T. Garino, "Multi-Scale Study of Sintering: A Review," *Journal of the American Ceramic Society*, vol. 89, no. 6, pp. 1914–1922, Jun. 2006.
- [26] M. W. Reiterer, K. G. Ewsuk, and J. G. Argüello, "An Arrhenius-Type Viscosity Function to Model Sintering Using the Skorohod–Olevsky Viscous Sintering Model Within a Finite-Element Code," *Journal of the American Ceramic Society*, vol. 89, no. 6, pp. 1930–1935, Jun. 2006.
- [27] G. Zheng, J. Zhao, Z. Gao, and Q. Cao, "Cutting performance and wear mechanisms of Sialon–Si₃N₄ graded nano-composite ceramic cutting tools," *Int J Adv Manuf Technol*, vol. 58, no. 1–4, pp. 19–28, May 2011.
- [28] Z.-H. Jin and W. J. Luo, "Thermal shock residual strength of functionally graded ceramics," *Materials Science and Engineering: A*, vol. 435–436, pp. 71–77, Nov. 2006.
- [29] C. Wu *et al.*, "Synthesis of AA7075-AA7075/B4C bilayer composite with enhanced mechanical strength via plasma activated sintering," *Journal of Alloys and Compounds*, vol. 701, pp. 416–424, Apr. 2017.

CHAPTER 6 - CONCLUSIONS AND FUTURE WORK

TEGs with improved lifetimes are in demand for applications with large temperature differences and for transient heat sources. Mid- to high-temperature TEGs materials used for these applications are brittle and experience cracking under thermal stress. Moreover, while decreasing grain size leads to higher efficiency bulk TEG materials these normally small-grained materials are even more brittle than larger grained counterparts. Grain size gradation has proven to widen the temperature band width of TE material.

We have successfully demonstrated that the performance of TEG materials benefit from functionally graded grains from submicron to micron sizes. Both continuously graded ZnO FGM and a five-layer discretely graded ZnO material were fabricated.

In addition, the sintering behavior of the continuously graded ZnO system was investigate and compared to that of the isothermally sintered samples to establish a model to predict the microstructure in the DGT plots. We have shown that the FGMs provide longer lifetime and that grain size can act as another engineering parameter in TEGs because it affects the peak efficiency amplitude and range as well as the distribution of thermal stress and associated cracking

6.1 SUMMARY OF PROCESSING

A one-step fabrication process was developed to produce a continuously graded microstructure. The large-grained side is ~ 1.2 micrometers graded somewhat exponentially to ~ 180 nm on the other side. The one-step processing method is done because it allows for ease of manufacturing of a large grain size distribution along the

whole thickness of the material. This is achieved by using modified SPS tooling, and in our case with ZnO, the pressure schedule is strategically applied to allow adsorbed water to outgas after it has aided in the sintering process. Along with this continuous grain size FGM, a method to predict the microstructure with isothermal runs was achieved. Our model to predict the microstructure, the Density-Grain Size-Time (DGT) plot, yields an initial predictability but is slightly off due to a stress shielding that is developed during sintering caused by differential sintering from the temperature gradient. Further investigation of this lead to a predictability within 3%.

In addition to the continuous grain size gradation, a parallel approach also provided another method for grain size gradation and helped model the gradation with discrete layers. The layers are individually sintered using knowledge of the DGT at different temperatures and thus different grain sizes so that the range of grain sizes is the same as the continuous gradation. Diffusion bonding was achieved by ramping slowly to 700°C and holding for five hours while the load is slowly ramped to 10 MPa, which is significantly lower than pressures used during sintering.

6.2 SUMMARY OF FGM MODELING EFFORT

With the help of Jin et al.'s model, curves of the peak efficiency versus current were constructed for a baseline of uniform grain sizes as well as the two FGMs. The five-layer FGM is modeled with data from the individual layers. The continuous FGM was modeled using the same gradation from the data used with the five-layer FGM, but instead of using the individual properties and layers, the property trends were used and 100 math layers were used.

6.3 SUMMARY OF EXPERIMENTAL RESULTS

To verify the simulated thermoelectric output, the efficiency output from the actual samples was measured and compared to the simulations. The simulations and experiments did suggest the same correlations and trends. The experimental current ranges are slightly different from the simulation results, most likely due to losses in the experimental setup. The normalized peak efficiencies are similar from simulation to experimental data partially validating the model. The experimental data show that the grain size plays a significant role in the TEG output. The large-grain sample was not as efficient as the small grain sample, but it had a larger current range. The FGMs seem to have a mix of both the high efficiency and larger current range, and the FGMs serve a larger purpose of mitigating thermal stress and extending lifetime. Because FGMs can survive thermal stress tests longer than the most efficient small-grained sample, FGMs provide a new method to increase the lifetime of TE materials. The grain size presents itself as another design parameter for thermoelectrics.

6.4 FUTURE WORK

There are two directions for more immediate future work in this dissertation. The first, and most important, is the continuation of Chapter 4's work. There should be extended lifetime tests on five or more samples. The effects should show a standard deviation and statistically verify the phenomena presented. The second is using a ZnO system that is competitive for TEG usage. This involves using Al-doped ZnO and an Al compositional gradient. The other more obvious direction is to use these types of FGMs with commercial TEGs such as Bi-Te systems, but this is not discussed further.

A. EXTENDED WORK ON GRAIN SIZE GRADATION IN ZNO

Since the TEG and lifetime test are only done on one of each material, more samples should be made and tested. The mode of failure should be investigated. To do this, the samples must be arranged so that a surface could be monitored for cracks and defects after all cycles of thermal load. One surface must be polished and exposed. That was not previously done and is rather arduous to do, but it may be necessary to find out the mode of cracking and how much cracking occurs in these samples as a function of time and grain size. Multiple samples should undergo lifetime testing to get good statistical data on the properties before and after cycling. After each test, the properties can be measured and microscopy can be done to investigate the cracking and degradation.

B. USING AN AL-DOPEZ ZNO SYSTEM

Spark plasma sintering of AZO has been achieved with excellent properties with varying amount of aluminum doping [1]. Also, many have achieved good sintering results with AZO nanopowders [2]–[4]. The biggest obstacle has been lowering the thermal conductivity of the ZnO material, and that has been done with nanostructuring [2], [54], [99]. One group has even been able to sinter carbon nanotubes in AZO, and this effect improved the electric conductivity by about an order of magnitude [8]. Sintering of AZO has proven to be a success, so further work with this material should be done. We will not know if there is significant thermal migration in the proposed AZO layers until we process the material, but there are also parallel manufacturing methods if there is significant mixing of layers. Furthermore, dopant in ZnO has been known to retard grain growth and induce abnormal grain growth, so these effects will play a role in the processing of AZO with controlled microstructure [9], [10].

Further characterization and testing of a doped ZnO system presents another form of FGM that can enhance the output in terms of TEG output over a larger current or temperature range. Our aim in any future work is to manufacture and design a nanostructured FGM thermoelectric with optimally doped sections to achieve the maximum peak efficiency possible over a large temperature range. The goal will be fulfilled by successfully completing the following research tasks:

- (1) Use SPS to make a layered FGM from starting powder with different aluminum contents for an AZO FGM. The powders will be fabricated with various Al content, then we will press some of one content in an SPS die and continue to pour and press powder with different Al content. The layered starting powder will then be sintered in the SPS with a die setup that has uniform temperature everywhere. Other dopants could be used as well.
- (2) Use the SPS to process a layered starting powder AZO FGM and a grain size gradation. This is similar to task one, but instead of using a die that will produce uniform temperature, a setup that induces a large thermal gradient will be used to produce a grain size gradation in addition to the compositional gradation. The grain size gradation is to have larger grains exposed to the heat source to mitigate thermal fatigue cracking to improve the lifetime.
- (3) Use the SPS to sinter individual samples with different Al or Ga content. These samples will be polished and reentered into the SPS on top of each other for another thermal processing step to diffusion bond them together to make the layered FGM.

Through our detailed experimental, theoretical, and some computational investigations, we will be able to answer the following fundamental questions in the design of functionally graded thermoelectrics: (i) Is it possible to fully control the compositional gradation in EFAS operations and achieve an unmixed, un-migrated FGM in terms of the add element? (ii) Is it possible to create both a compositional and grain size gradation at the same time? (iii) Can we approach the manufacturing form a stepped process to achieve the FGMs wanted? (iv) How do the gradation techniques affect the more commonly used thermoelectric systems such as the tellurides? (v) Can the thermoelectric efficiency be optimized with a compositional and grain size gradation with one manufacturing process and one material to make segmented TEGs obsolete?

For the initial experiments on the FGM with compositional gradation, individual layers with a given Al content should be sintered and characterized. Then powders with different Al content will be compacted next to each other and sintered as in Figure 6.1. The powders will be pressed in stages to get the layered green part shown. The layered FGM will be characterized to see if the compositional content is the same as the in uniform sintering runs. The thermoelectric properties of the FGM will be measured as well as the efficiency output. Essentially, the same process from Chapter 5 should be repeated but for this novel AZO system.

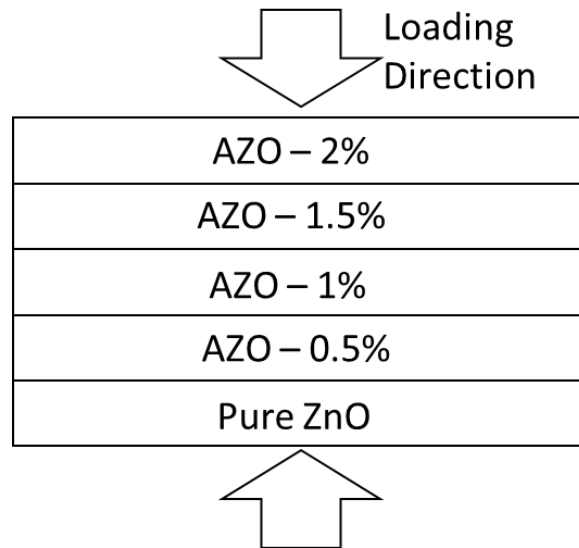


Figure 6.1: Schematic of layered powder for sintering of compositional FGM TEG.

C. CONTINUED INVESTIGATION OF STRESS SHIELDING IN THERMAL GRADIENT SPS

It has been shown in the current work that the shielding effect of sintering material in a TG is not inherent to one material. The effect is eminent in zirconia and zinc oxide. Zirconia is a candidate material for FGM cutting tools, so it will important to use the current work's analysis when making controlled FGM zirconia samples. Once that process is well modelled and controlled, mechanical properties should be tested. Also, these types of property gradients are of interest to the biomedical field. This type of gradient should be done with a biomedical implant material such as hydroxyapatite, 316L steel, and titanium. The design should call for a porosity gradient corresponding to a bone infiltration rate. Based on the data in the current work, if the correct amount of pressure is not used, then the density will not match the model, so for correct density and hence correct bone infiltration, the shielding effect must be accounted for.

D. FINAL REVIEW AND RECOMMENDATION

We successfully demonstrated that FGMs with grain size gradation provide longer lifetime and that grain size can act as another engineering parameter in TEGs because it affects the peak efficiency amplitude and range, as well as the distribution of thermal stress and associated cracking. In future work, a plan provides a method for improvement using compositional gradient FGMs with material that might be promising for use in industry. By using what we have learned in this dissertation and continuing the path of this future work, continued development and optimization of TE material can be achieved.

AZO is recommended as the candidate materials to achieve a grain size gradation for a protective barrier for transient heat fluxes and improved temperature bandwidth. The next step is to try sintering AZO in a thermal gradient to see if the grain size distribution is the same. There could be challenges with the sintering and the microstructural evolution as there is a spinel phase in the grain boundaries that hinders diffusion and thus may alter sintering mechanisms [11]. In addition, the concentration of Al in the AZO is considered as another variable to achieve gradation in chemical composition. The objective is to study whether an electrical conductivity gradient enhances the temperature bandwidth even further as in [12]. There could be problems with thermal migration of the different aluminum contents rendering the sample un-graded or partially mixed in Al content after processing. The grain size gradation can also be applied in Bi-Te system. Since it is challenging to process in a TG large enough to get a significant grain size gradation, the approach is to make the Bi-Te in two layers: a thin layer of large grains to protect against thermal stresses, and the rest of the material with nanostructured material for high

efficiency. This can be achieved with 3-D printing. Subsequently, depending on whether the AZO mixes or stays graded, a conductivity gradient could be done in Bi-Te.

REFERENCES

- [1] Y.-H. Chou, J. L. H. Chau, W. L. Wang, C. S. Chen, S. H. Wang, and C. C. Yang, "Preparation and characterization of solid-state sintered aluminum-doped zinc oxide with different alumina contents," *Bull. Mater. Sci.*, vol. 34, no. 3, pp. 477–482, Sep. 2011.
- [2] J. Han, P. Q. Mantas, and A. M. R. Senos, "Densification and grain growth of Al-doped ZnO," *J. Mater. Res.*, vol. 16, no. 02, pp. 459–468, 2001.
- [3] K. F. Cai, E. Müller, C. Drašar, and A. Mroczek, "Preparation and thermoelectric properties of Al-doped ZnO ceramics," *Mater. Sci. Eng. B*, vol. 104, no. 1–2, pp. 45–48, Nov. 2003.
- [4] K. J. Chen *et al.*, "The crystallization and physical properties of Al-doped ZnO nanoparticles," *Appl. Surf. Sci.*, vol. 254, no. 18, pp. 5791–5795, Jul. 2008.
- [5] W. Kim, "Strategies for engineering phonon transport in thermoelectrics," *J. Mater. Chem. C*, vol. 3, no. 40, pp. 10336–10348, Oct. 2015.
- [6] D. G. Cahill *et al.*, "Nanoscale thermal transport," *J. Appl. Phys.*, vol. 93, no. 2, pp. 793–818, Jan. 2003.
- [7] G. J. Snyder and E. S. Toberer, "Complex thermoelectric materials," *Nat. Mater.*, vol. 7, no. 2, pp. 105–114, Feb. 2008.
- [8] C. Dreßler, R. Löhnert, J. Gonzalez-Julian, O. Guillon, J. Töpfer, and S. Teichert, "Effect of Carbon Nanotubes on Thermoelectric Properties in Zn_{0.98}Al_{0.02}O," *J. Electron. Mater.*, pp. 1–5, Oct. 2015.
- [9] J. Sengupta, R. K. Sahoo, and C. D. Mukherjee, "Effect of annealing on the structural, topographical and optical properties of sol–gel derived ZnO and AZO thin films," *Mater. Lett.*, vol. 83, pp. 84–87, Sep. 2012.
- [10] S.-Y. Kuo *et al.*, "Effects of doping concentration and annealing temperature on properties of highly-oriented Al-doped ZnO films," *J. Cryst. Growth*, vol. 287, no. 1, pp. 78–84, Jan. 2006.
- [11] Y.-H. Chou, J. L. CHAU, W. L. Wang, C. S. Chen, S. H. Wang, and C. C. Yang, "Preparation and characterization of solid-state sintered aluminum-doped zinc oxide with different alumina contents," *Bull. Mater. Sci.*, vol. 34, no. 3, pp. 477–482, 2011.
- [12] M. Koizumi, "FGM activities in Japan," *Compos. Part B Eng.*, vol. 28, no. 1–2, pp. 1–4, 1997.

APPENDIX A

ZNO CATALYSIS COMPLEXION DIFFUSION TRANSPORT

Spark plasma sintering (SPS) of ZnO at low temperatures ($\sim 400^\circ\text{C}$) was difficult until the introduction of adsorbed water on the surface of particles. Research started with water sintering when oxides were sintered in the presence of steam. There are profound effects on the transport of diffusing ions during sintering of ZnO when water is adsorbed to the surface. Dargatz et al. have studied the effects of water in depth and have three theories about the mechanisms that may be occurring [1], [2]. Water has been known to decrease the surface energy that contributes to sintering in the early stages [3]. Quach et al. saw a decrease in surface energy due to adsorbed water but did not discuss the kinetics [4], while others only studied the effects of water on the kinetics of mass transport [5]–[7]. Here, the helpful effects of the water are only seen when done with fast heating rates [8]. It has been shown that pre-adsorbed CO_2 can be replaced by water as well [9]. The preferred location of hydrogen defects as dopants has been discussed, and in [1] a group characterized the defect stoichiometry that caused an apparent hydroxide-ion-enhanced densification and have further evidence and clues to the enhanced sintering in terms of defects and grain growth [2].

Dargatz et al. came up with three valid theories that could be controlling the aided sintering of ZnO with adsorbed water on the surface. The first theory is that the dissociation of surface bound water is affecting the stoichiometry and enhancing oxygen-hydrogen related defects. The second theory is that there is a liquid film on the surface with dissolved Zn^{2+} and O^{2-} ions acting similarly to liquid phase sintering. The third theory

is that there is a surface cleaning where the adsorbed water replaces a carbonate layer. These could be happening simultaneously, but it is evident that the root cause for this enhanced sintering of ZnO is still not known completely.

For the third theory, the XPS data of a sample sintered with water shows no traces of carbon associated with the carbonate form, and there is carbon associated with carbonate when sintering without water suggesting that the water rid the surface of carbonate. This could influence the surface energy and driving force for sintering. The second theory hints that there is enhanced surface transport in a liquid form, not the same as liquid phase sintering. The reason it is believed to be like liquid phase sintering is the grains tend to be anisotropic when sintering with water. In liquid phase sintering, there is a preferential grain growth typically because of preferential precipitates at grains causing an elongation.

The most important theory considered in [1], [2] is the first one, and perhaps it is the most valid, and we wish to elaborate on the theory and provide a full theory and tests. The evidence is that the apparent activation energy is lower, which would correspond to different diffusivity of ions. A hydroxide ion is proposed as a possible mechanism. Also, the blue color observed after sintering is proof of excess hydrogen as a residual dopant in ZnO. The theory stops here though.

In ZnO, the slowest ion to diffuse is the oxygen ion through grain boundaries according to [10]. It is also known that the diffusivity of Zn in the ZnO lattice is much faster than that of oxygen and the same relationship is thought to be upheld in the grain boundaries [11]. Also, a space charge layer is known thought to contribute to diffusion in oxide ceramics. Investigation of a space charge layer in pure ZnO needs to be done because

that might contribute to the diffusion and rate limiting step during sintering, and the water adsorption might be creating a space charge layer or interacting with an existing one to aid in densification. This is where the dissociation of water can be playing a huge role along with three other equilibrium equations. In the early stages of sintering, there will be some concentration gradient of Zn^{2+} and O^{2-} as they diffuse at different rates, oxygen being the slower one. This will drive some movement of the particles to neck areas where they will then establish equilibrium.

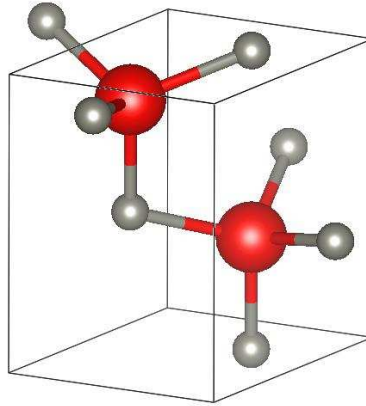


Figure A.1: Primitive unit cell of ZnO showing corner Zn atoms and hexagonal nature of the cell.

Now, consider the dissociation of the water is shown in (A.1). The concentration gradient of Zn and O will still exist, but now there are more reactions occurring at the surface. A view graph of the unit cell of ZnO, which is hexagonal wurtzite, is shown in Figure A.1. There is a stable place for hydroxide to settle on a close packed plane of Zn atoms, so it could settle in between the three grey Zn atoms and the hydrogen is free to settle either on surface of one atomic layer deep where it reacts with the oxygen from the ZnO lattice.



The hydrogen ions or protons will combine with the oxygen ions from the ZnO lattice as in (A.2). Now the effective ionic radius will go from 126 pm in Oxygen ions to 99 pm in hydroxide ions. Thus, the diffusivity should be higher making it easier for the hydroxide to transport in the lattice and possibly at grain boundaries as well.

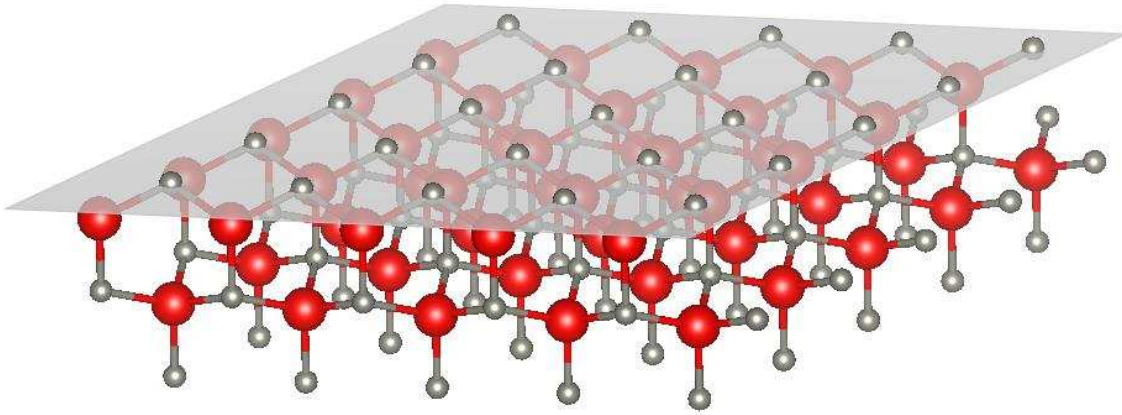


Figure A.2: Surface of ZnO in atoms showing the c-direction close packed plane of Zn.

This cannot be the only reactions going on as we have only created a reaction for the enhanced diffusivity of the slowest ion, O^{2-} . Once the hydroxide ion has diffused to the side where there was a concentration gradient of Zn^{2+} and O^{2-} ions and it will do this because it still has a negative charge, there now must be another equilibrium reaction to bring the hydroxide back to oxygen ions for a net flux of oxygen contributing to diffusion for sintering. This is where we consider the reaction of a possible complex reaction happening to regain stoichiometric ZnO listed in (A.3), where the complex allows for interactions of the smaller cation to reduce to the stoichiometric lattice with water being

released. This is a surface effective reaction, and the surface is represented in Figure A.2 to show the close packed plane in the c-direction more clearly.



In summary, we have reason to believe that the consumption of water by dissociation helps protonate oxygen ions, which in turn promotes the diffusion and thus aids in sintering. The ion then diffuses and reacts to form stoichiometric ZnO and releases water vapor. We believe these are in equilibrium and still driven by concentration gradients and charge differences as well as the regular curvature driven thermodynamic pressure for sintering. The stability of a hydroxide ion near the sintering surface is high as it is surrounded by charged zinc, so the hydroxide can settle where an oxygen would be at the surface and then recombine to satisfy a ZnO lattice filling and water that is release or evaporated on the surface. This would also cause the preferred c-axis grain growth seen in [2]. A schematic of the process can be seen below in Figure A.3.

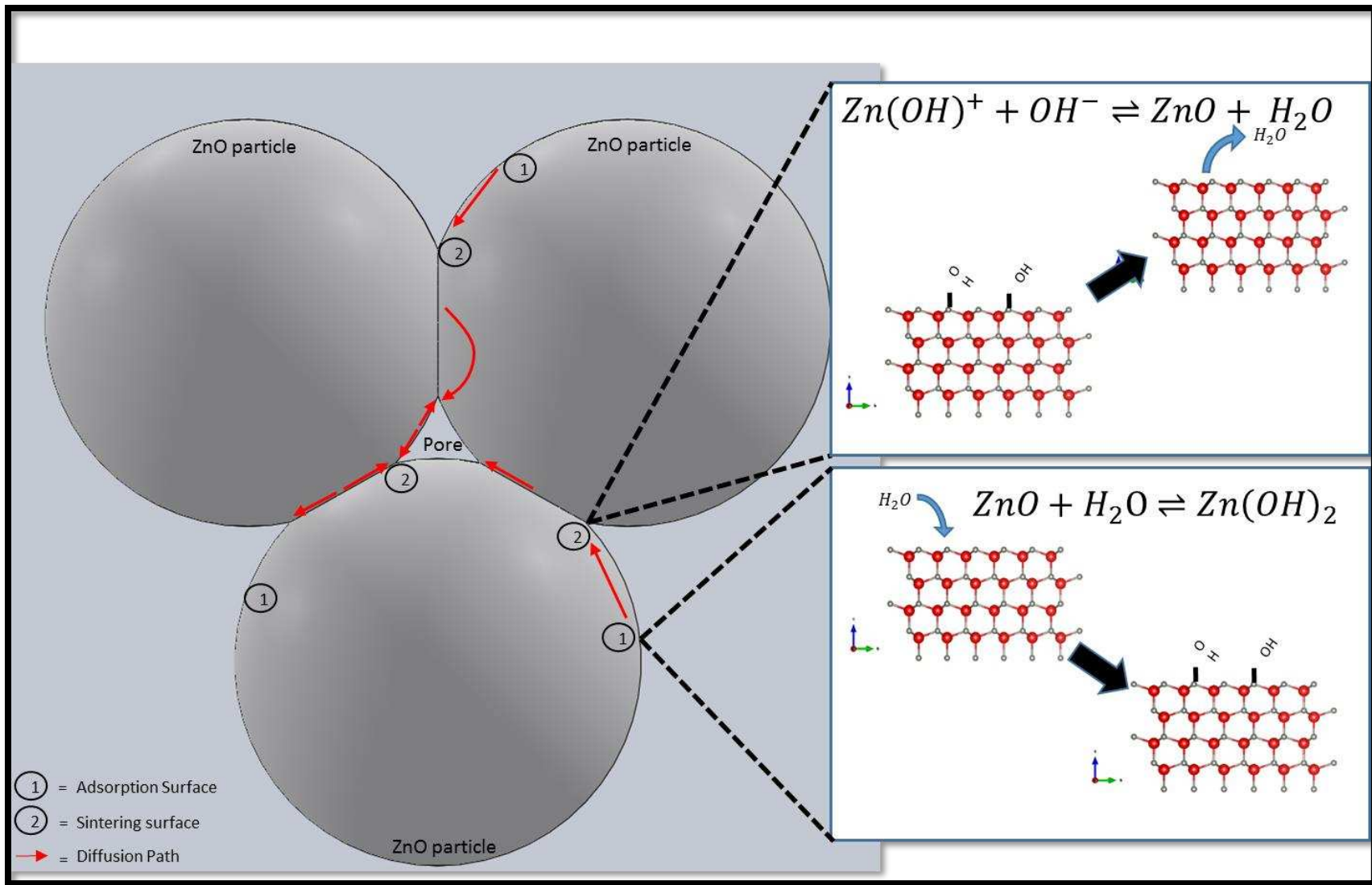


Figure A.3: Schematic of water sintering mechanisms.

REFERENCES

- [1] B. Dargatz *et al.*, “FAST/SPS sintering of nanocrystalline zinc oxide—Part I: Enhanced densification and formation of hydrogen-related defects in presence of adsorbed water,” *Journal of the European Ceramic Society* 36.5 (2016): 1207-1220.
- [2] B. Dargatz, J. Gonzalez-Julian, M. Bram, Y. Shinoda, F. Wakai, and O. Guillon, “FAST/SPS sintering of nanocrystalline zinc oxide—Part II: Abnormal grain growth, texture and grain anisotropy,” *Journal of the European Ceramic Society*. 36.5 (2016): 1221-1232.
- [3] R. H. R. Castro and D. V. Quach, “Analysis of Anhydrous and Hydrated Surface Energies of gamma-Al₂O₃ by Water Adsorption Microcalorimetry,” *J. Phys. Chem. C*, vol. 116, no. 46, pp. 24726–24733, Nov. 2012.
- [4] D. V. Quach, A. R. Bonifacio, and R. H. R. Castro, “Water adsorption and interface energetics of zinc aluminate spinel nanoparticles: Insights on humidity effects on nanopowder processing and catalysis,” *Journal of Materials Research*, vol. 28, no. 15, pp. 2004–2011, 2013.
- [5] J. A. Varela, O. J. Whittemore, and E. Longo, “Pore size evolution during sintering of ceramic oxides,” *Ceramics International*, vol. 16, no. 3, pp. 177–189, 1990.
- [6] P. J. Anderson and P. L. Morgan, “Effects of water vapour on sintering of MgO,” *Trans. Faraday Soc.*, vol. 60, no. 0, pp. 930–937, Jan. 1964.
- [7] L. Perazolli, J. A. Varela, E. R. Leite, and E. Longo, “Effect of Atmosphere on the Sintering and Grain Growth of Tin Oxide,” *Materials Science Forum*, vol. 299–300, pp. 134–140, 1999.
- [8] S. Schwarz, A. M. Thron, J. Rufner, K. van Benthem, and O. Guillon, “Low Temperature Sintering of Nanocrystalline Zinc Oxide: Effect of Heating Rate Achieved by Field Assisted Sintering/Spark Plasma Sintering,” *J. Am. Ceram. Soc.*, vol. 95, no. 8, pp. 2451–2457, Aug. 2012.
- [9] D. Gouvêa, S. V. Ushakov, and A. Navrotsky, “Energetics of CO₂ and H₂O Adsorption on Zinc Oxide,” *Langmuir*, vol. 30, no. 30, pp. 9091–9097, Aug. 2014.
- [10] J. P. Angle, P. E. D. Morgan, and M. L. Mecartney, “Water Vapor-Enhanced Diffusion in Alumina,” *J. Am. Ceram. Soc.*, vol. 96, no. 11, pp. 3372–3374, Nov. 2013.
- [11] A. P. Hynes, R. H. Doremus, and R. W. Siegel, “Sintering and Characterization of Nanophase Zinc Oxide,” *Journal of the American Ceramic Society*, vol. 85, no. 8, pp. 1979–1987, Aug. 2002.

APPENDIX B

SELECTION OF FEEDSTOCK POWDER TO OBTAIN MINIMUM SINTERING CONDITIONS - DIRECT COMPARISON OF US RESEARCH NANOMATERIALS, INC. ZNO VERSUS INFRAMAT ADVANCED MATERIALS, LLC ZNO

When finding powder for sintering for a wide range of conditions for full density and grain growth, it is important to make sure the particle size is very small and the purity is very high to retain submicron-sized grains. Both particle size and purity contribute to uniform and successful sintering. The smaller particle sizes will yield more surface area thus more energy for sintering according. The purity is to ensure that no diffusion paths are blocked or hindered. The other very important part of nano particles is how they are synthesized. US Nano synthesizes their ZnO powder with wet chemistry method as opposed to Infrastructure Material's (Inframat) method of choice of spray pyrolysis and Sky springs method of Sol-gel. Because of the wet chemistry method, most likely co-precipitation method, it has more favorable particle distribution than other manufacturers due to less hard agglomerates because the method involves reactions in solvents at low temperature. Spry pyrolysis has a rapid quench from combustion in which the time to cool is not significant enough to get particles to stay dispersed. The effect of the rapid quench from spray pyrolysis is usually hard agglomeration where some of the particles sinter together.

The comparison between Inframat and US Nano is done by first looking at the powder in SEM, then processing the powder with the same conditions, and then doing some post processing to achieve some density numbers and microstructural views.

SEM of both powders is shown below. The US nano has smaller particle size and less hard agglomerates in Figure B.1.

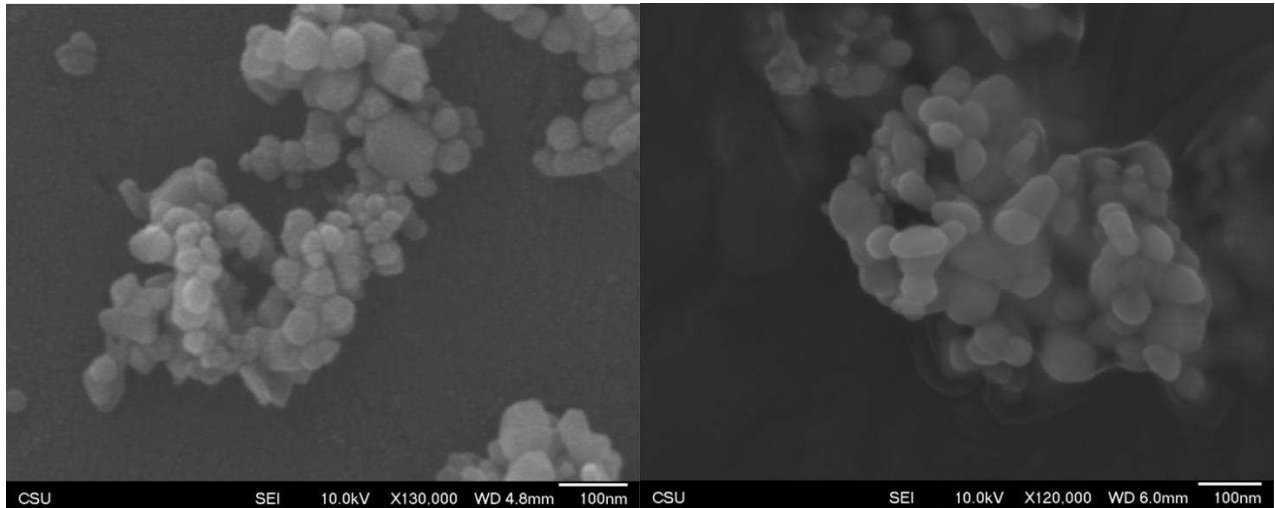


Figure B.1: US Nano nanopowder on the left. Inframat nanopowder on the right.

To compare the processing of the powders, a sample fabricated from US Nano ZnO powder was sintered at 600°C, 200°C/min, 50 MPa, and 30 minutes of hold time from as received powder. An Inframat sample was done with the same schedule. 1.6 wt.% of deionized water was added after an initial green compaction to both samples before sintering. Densification curves are shown below on background subtracted samples.

The densification versus time show that there is more densification in the US nano sample into the hold whereas the Inframat is done sintering 10 minutes into the hold and possibly de-sinters. Both samples are sintered close to theoretical density.

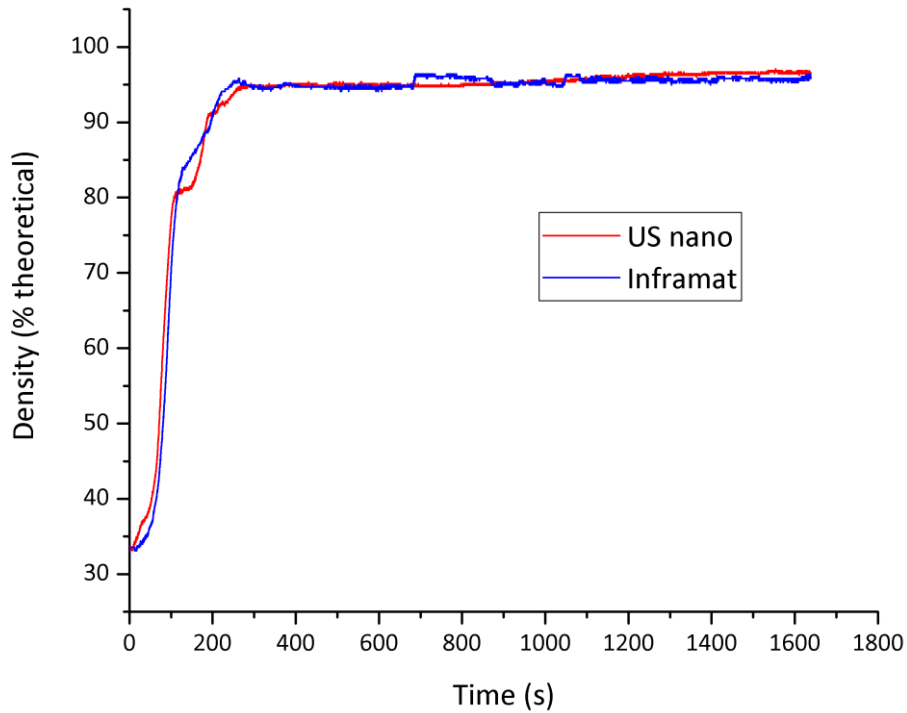


Figure B.2: Density versus time for Inframmat and US Nano samples both sintered at 600°C, 200°C/min, 50 MPa, and 30 minutes.

Once densification curves are done, the process is done again for both powders to ensure a fresh sample as the samples done with background subtractions are now not as useful since they have been thermally cycled twice. Post processing is done which includes Archimedes density, geometric density, and areal density. SEM is done on the samples to analyze areal density and microstructure. All SEM images are 15,000 x and are done on samples after polishing to 1 micron and etching for 3 seconds in 5% acetic acid.

Table B.1: Densities of processed powders.

Sample	Areal density (% theoretical)	Geometric density (% theoretical)	Archimedes density (% theoretical)
US Nano	96 ± 1.3	96	97
Inframmat	92 ± 2.3	97	96

SEM images of the samples are shown in Figure B.3. Microstructural differences are very interesting. The areal densities are different as well. The US Nano sample achieves close to full density and has larger grain sizes. Densification is more dominant opposed to coarsening, but significant coarsening did take place. Coarsening also played a significant role because the sample was held for 30 minutes. The Inframat sample had densification and coarsening at the same driving force causing large open porosity and smaller grains. Pores are thermodynamically impossible to close in the Inframat sample because they are about the same size as the grains, hence the 20 minutes of stagnant densification and no coarsening. It is shown in the image below that the US Nano sample is more promising for a wide range of sintering conditions which is needed in thermal gradient sintering. The Inframat could achieve full density, but it would take significantly more load and temperature, which is not the goal of our research. To get our continuous grain size gradient to work, we needed US Nano powder.

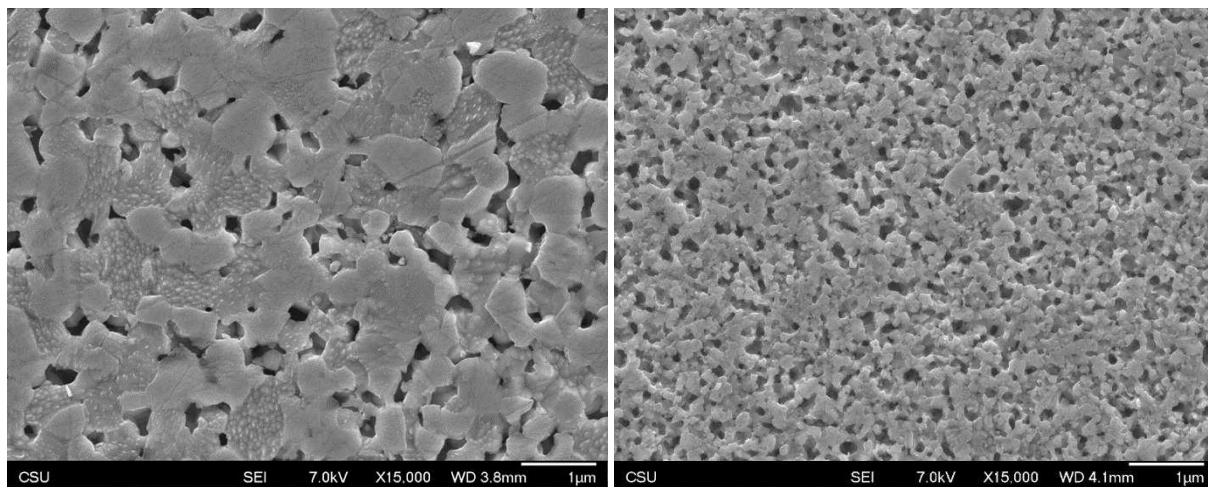


Figure B.3: SEM for US Nano (left) and Inframat (right) samples both sintered at 600°C, 200°C/min, 16 kN, and 30 minutes.